

## Visible light driven H<sub>2</sub>O<sub>2</sub> synthesis by p-type copper-based sulfide photocathodes

著者	Chen Chao
year	2022-07-20
その他のタイトル	可視光照射下でH <sub>2</sub> O <sub>2</sub> を生成するp型銅系硫化物光電カソード電極の開発に関する研究
学位授与年度	令和4年度
学位授与番号	17104甲工第558号
URL	<a href="http://doi.org/10.18997/00009003">http://doi.org/10.18997/00009003</a>

# **Visible light driven H<sub>2</sub>O<sub>2</sub> synthesis by p-type copper-based sulfide photocathodes**

July 20<sup>th</sup>, 2022

Kyushu Institute of Technology

Graduate School of Engineering

Major: Engineering; Graduate School of Engineering

Chao Chen

# Contents

<b>Introduction .....</b>	<b>1</b>
1. Background.....	2
2. Light-driven oxygen reduction for H <sub>2</sub> O <sub>2</sub> production .....	3
3. Metal sulfides as photoelectrocatalysts .....	5
4. Strategies for improving photoelectrocatalytic performance .....	7
4.1 Light absorption efficiency .....	8
4.2 Charge separation efficiency .....	13
4.3 Charge injection efficiency .....	20
5. Summary .....	23
6. Research perspectives .....	24
References .....	26
<b>Visible light-driven H<sub>2</sub>O<sub>2</sub> synthesis by a Cu<sub>3</sub>BiS<sub>3</sub> photocathode via a photoelectrochemical indirect two-electron oxygen reduction reaction .....</b>	<b>32</b>
1. Introduction.....	33
2. Experimental section.....	36
2.1 Chemicals .....	36
2.2 Fabrication of a Cu <sub>3</sub> BiS <sub>3</sub> photocathode.....	36
2.3 Modification with n-type buffer layers.....	37
2.4 Deposition of Au.....	38
2.5 Characterization of catalysts .....	38
2.6 Photoelectrochemical (PEC) measurement.....	38
2.7 Analysis of products .....	39
3. Results and discussion.....	40
3.1 Comparison of electrodes prepared by electrophoretic deposition and spray pyrolysis deposition .....	40
3.2 Modification with In <sub>2</sub> S <sub>3</sub> for formation of <i>p-n</i> junctions .....	46
3.3 Optimization of the co-catalytic layer for H <sub>2</sub> O <sub>2</sub> production.....	51
3.4 Photoelectrocatalytic mechanism analysis.....	58

4. Conclusions .....	60
References .....	61
<b>Preparation of Cu<sub>3</sub>VS<sub>4</sub> photocathode and its application in the preparation of H<sub>2</sub>O<sub>2</sub> by oxygen reduction .....</b>	<b>66</b>
1. Introduction.....	67
2. Experimental section.....	69
2.1 Chemicals .....	69
2.2 Fabrication of a Cu <sub>3</sub> VS <sub>4</sub> photocathode .....	70
2.3 Modification with n-type buffer layers.....	70
2.4 Doping of Ag or Ga in CVS electrodes.....	71
2.5 Characterization of catalysts .....	71
2.6 Photoelectrochemical (PEC) measurement.....	72
2.7 Analysis of products .....	72
3. Results and discussion.....	72
3.1 Ag doped Cu <sub>3</sub> VS <sub>4</sub> photocathode .....	72
3.2 Ga doped Cu <sub>3</sub> VS <sub>4</sub> photocathode .....	76
3.3 Ga, Ag co-doped Cu <sub>3</sub> VS <sub>4</sub> photocathode .....	80
3.4 Sulfurization time and temperature optimization.....	83
3.5 The modification of n-type semiconductors .....	86
4. Conclusions .....	91
References .....	92
<b>Conclusion and outlook.....</b>	<b>94</b>
1. Conclusion .....	95
2. Outlook.....	96
<b>Acknowledgements.....</b>	<b>97</b>
<b>List of Publications .....</b>	<b>98</b>



## Part 1

### **Introduction**

## 1. Background

In line with the increasingly serious energy crisis, investigations on the applications of solar energy, a clean and inexhaustible energy source, have become ever more important [1-3]. Up to now, the most extensive use of solar energy is to convert it into electric energy, that is, the application of solar cells. However, there are also some problems in energy storage, transmission and utilization efficiency with this route [4]. The direct conversion of solar energy into usable chemical energy is another route, for example, the generation of  $H_2$  by water decomposition reaction [5-7], and the conversion of  $CO_2$  into fossil fuels such as  $CH_4$  (Figure 1) [8, 9].

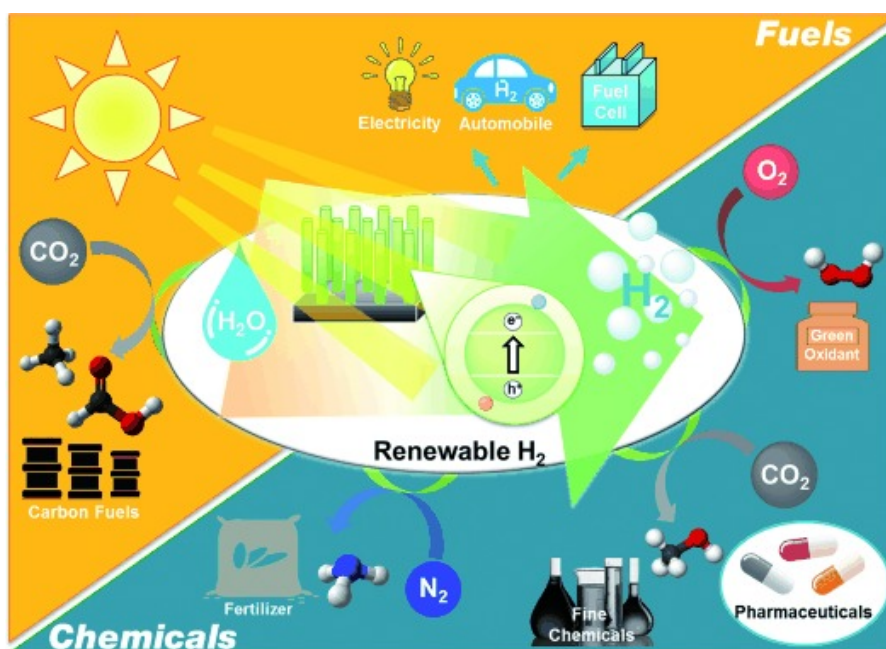
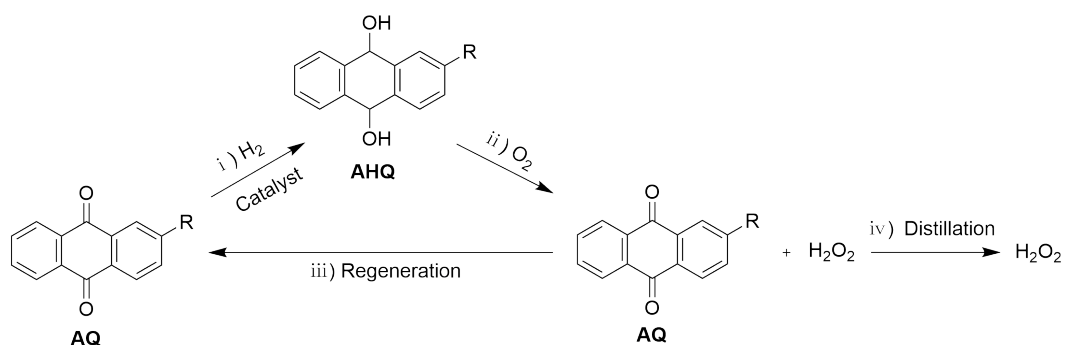


**Figure 1.** Scheme of direct conversion of solar energy into usable chemical energy [1].

Recently, hydrogen peroxide ( $H_2O_2$ ) has attracted a lot of attention as a promising green fuel. As a clean and environmental-friendly green oxidant,  $H_2O_2$  is widely used in pulp and textile bleaching [10], sterilization [11], and wastewater treatment [12], hydrometallurgy and electronics industries [13]. In addition, the development of  $H_2O_2$  fuel cells further enhances its potential value. The theoretical open circuit voltage of  $H_2O_2$  fuel cells (theoretical  $V_{oc} = 1.1$  V, comparable to 1.23 V of  $H_2$  fuel cells) is comparable to that of  $H_2$  fuel cell [14]. In addition,  $H_2O_2$  has the advantage of high energy density and can be stored as an aqueous solution at normal temperature and pressure, which is safer and

easier to transport [1]. Compared to other liquid fuels (such as methanol),  $H_2O_2$  is more environmentally friendly as the products are only water and oxygen, so some people call it an ideal new solar fuel [15].

So far, anthraquinone (AQ) auto-oxidation has been the main process for the industrial production of  $H_2O_2$ , accounting for more than 95% of global production. (Scheme 1) [16]. The primary process of the AQ method consists of the following four steps: i) hydrogenation of AQ to produce anthrahydroquinone (AHQ); ii) Oxidation of AHQ to produce hydrogen peroxide and AQ; iii) Extraction of  $H_2O_2$ , purification and regeneration of AHQ into AQ; iv) purification and concentration of  $H_2O_2$ . As a popular technology, the AQ method has the advantages of cost-effectiveness and convenience for mass production. However, as a critical step, AQ hydrogenation requires the precious metal Pt as a catalyst to achieve it. In addition, the steps of hydrogenation and concentration are energy-intensive and generate large amounts of waste, which is not conducive to environmental protection.



**Scheme 1.** Schematic of the anthraquinone (AQ) process for the generation of  $H_2O_2$ .

## 2. Light-driven oxygen reduction for $H_2O_2$ production

Therefore, efforts have been made to develop new environmentally friendly methods for the production of  $H_2O_2$ . Photocatalytic reactions have attracted widespread interest from researchers since Fujishima and Honda first reported titanium dioxide catalyzed hydrolysis under UV light in 1972 [17]. Recently, the production of  $H_2O_2$  via photocatalytic reaction processes has received increasing attention, which would be a meaningful breakthrough in  $H_2O_2$  chemistry [18]. Compared to the AQ method, the photocatalytic method uses renewable sunlight as an energy source and the reaction can be carried out

at room temperature and pressure, making it a safe and green method of H<sub>2</sub>O<sub>2</sub> production.

Generally, there are two photocatalytic H<sub>2</sub>O<sub>2</sub> production pathways, i.e., particulate photocatalytic (PC) and photoelectrochemical (PEC) systems [2]. Conventional photocatalytic generation of H<sub>2</sub>O<sub>2</sub> from PC systems is based on inorganic semiconductors such as BiVO<sub>4</sub>, TiO<sub>2</sub>, etc. [10, 19-21]. However, inorganic semiconductors are still inefficient for photocatalytic H<sub>2</sub>O<sub>2</sub> generation due to factors such as large band gap values and high charge recombination rates. Recently, various PC systems based on organic-polymer semiconductors have been developed for photocatalytic H<sub>2</sub>O<sub>2</sub> generation, the most representative of which is graphitic carbon nitride (C<sub>3</sub>N<sub>4</sub>) with a recorded solar-to-H<sub>2</sub>O<sub>2</sub> (STH) conversion efficiency of 0.61% [22-24]. However, as the strongly oxidizing hydroxyl radicals (•OH) are inevitably generated during photocatalytic H<sub>2</sub>O<sub>2</sub> production ( $\text{H}_2\text{O}_2 + h\nu \rightarrow 2\cdot\text{OH}$  or  $\text{H}_2\text{O}_2 + e^- + \text{H}^+ \rightarrow \cdot\text{OH} + \text{H}_2\text{O}$ ), the stability of these semiconductors is challenged [25].

For the systems of photoelectrochemical cells, oxidation and reduction reactions occur on the photoanode and photocathode, respectively, i.e., the selectivity and activity for ORR and WOR can be separately improved. Studies on WOR generating H<sub>2</sub>O<sub>2</sub> have mainly focused on the development of photoanode metal oxide materials [26]. Fuku et al. reported that a WO<sub>3</sub>/BiVO<sub>4</sub> photoanode coated with a mesoporous Al<sub>2</sub>O<sub>3</sub> layer could lead to excellent oxidative H<sub>2</sub>O<sub>2</sub> generation at a selectivity of ca. 80% [27]. Yin et al. developed a BiVO<sub>4</sub> photoanode with surface oxygen vacancies that showed a photocurrent density of 4.32 mA·cm<sup>-2</sup> at 1.23 V vs. RHE [28]. However, H<sub>2</sub>O<sub>2</sub> production via WOR by PEC systems is restricted by the high redox potential for H<sub>2</sub>O<sub>2</sub> production via WOR (1.74 V vs. RHE; eq. 1). Prevention of the decomposition of H<sub>2</sub>O<sub>2</sub> at such high oxidation potential is difficult since H<sub>2</sub>O<sub>2</sub> usually serves as an excellent hole scavenger and an intermediate reductant. In this case, accumulation of H<sub>2</sub>O<sub>2</sub> is difficult in a PEC system that mainly relies on WOR.



The use of a PEC system for boosting ORR (0.68 V vs. RHE; eq. 2) is a promising strategy for H<sub>2</sub>O<sub>2</sub> production. According to the electron transfer process and reaction intermediates, the ORR to H<sub>2</sub>O<sub>2</sub> can be further divided into direct 2e<sup>-</sup> ORR and indirect 2e<sup>-</sup> ORR pathways, i.e., a one-step two-electron O<sub>2</sub> reduction process (eq. 2) and via a superoxide radical intermediate ( $\bullet O_2^-$ ) two-step one-electron O<sub>2</sub> reduction process (equations (3) and (4)). The reaction process and thermodynamics of H<sub>2</sub>O<sub>2</sub> generation through direct and indirect ORR processes are listed in equations (2)-(4). Clearly, the reaction potential of the direct ORR (+0.68 V) is more positive than that of the indirect ORR (-0.33 V), indicating that the direct ORR is thermodynamically favorable. Nevertheless, from the viewpoint of reaction dynamics, the indirect ORR process is facile and kinetically favorable, since only one electron is needed for each step, while the direct ORR process needs two electrons.

### 3. Metal sulfides as photoelectrocatalysts

So far, many metal sulfides have been developed for photoelectric catalysis, as shown in the periodic table of elements below, with the metal elements highlighted in red (Figure 2) [29]. This is because metal sulfides have high light absorption coefficients and suitable band gaps due to their S2p orbitals, which can enhance light absorption compared to metal oxide semiconductors with O2p orbitals [30]. Furthermore, the structures of metal sulfides are easily tunable in terms of morphology, crystallinity, and chemical composition, leading to customizable chemical, electronic, optical, physical properties.

**Periodic Table of Elements**

1 H Hydrogen																	2 He Helium
3 Li Lithium	4 Be Beryllium											5 B Boron	6 C Carbon	7 N Nitrogen	8 O Oxygen	9 F Fluorine	10 Ne Neon
11 Na Sodium	12 Mg Magnesium											13 Al Aluminum	14 Si Silicon	15 P Phosphorus	16 S Sulfur	17 Cl Chlorine	18 Ar Argon
19 K Potassium	20 Ca Calcium	21 Sc Scandium	22 Ti Titanium	23 V Vanadium	24 Cr Chromium	25 Mn Manganese	26 Fe Iron	27 Co Cobalt	28 Ni Nickel	29 Cu Copper	30 Zn Zinc	31 Ga Gallium	32 Ge Germanium	33 As Arsenic	34 Se Selenium	35 Br Bromine	36 Kr Krypton
37 Rb Rubidium	38 Sr Strontium	39 Y Yttrium	40 Zr Zirconium	41 Nb Niobium	42 Mo Molybdenum	43 Tc Technetium	44 Ru Ruthenium	45 Rh Rhodium	46 Pd Palladium	47 Ag Silver	48 Cd Cadmium	49 In Indium	50 Sn Tin	51 Sb Antimony	52 Te Tellurium	53 I Iodine	54 Xe Xenon
55 Cs Cesium	56 Ba Barium	57-71	72 Hf Hafnium	73 Ta Tantalum	74 W Tungsten	75 Re Rhenium	76 Os Osmium	77 Ir Iridium	78 Pt Platinum	79 Au Gold	80 Hg Mercury	81 Tl Thallium	82 Pb Lead	83 Bi Bismuth	84 Po Polonium	85 At Astatine	86 Rn Radon
87 Fr Francium	88 Ra Radium	89-103	104 Rf Rutherfordium	105 Db Dubnium	106 Sg Seaborgium	107 Bh Bohrium	108 Hs Hassium	109 Mt Meitnerium	110 Ds Darmstadtium	111 Rg Roentgenium	112 Cn Copernicium	113 Nh Nihonium	114 Fl Flerovium	115 Mc Moscovium	116 Lv Livermorium	117 Ts Tennessine	118 Og Oganesson

**Figure 2.** Common metal elements (highlighted in red) used to construct binary, ternary or quaternary sulfide photoelectrodes for PEC applications [29].

However, metal sulfides also suffer from photo-corrosion during the photoelectrocatalytic reaction, where metal sulfides are oxidized by photogenerated holes, thereby damaging the material structure and leading to a reduction in performance. So far, a series of strategies have been adopted to inhibit the photocorrosion and dissolution of materials from improving the stability of metal sulfides. The main components include:

The use of sacrificial agents (such as  $\text{Na}_2\text{S}$  and  $\text{Na}_2\text{SO}_3$ ) in the electrolyte as vacancy scavengers in the electrolyte to deplete the vacancies prone to photocorrosion;

Surface modification with co-catalysts to enhance oxygen production or the rate of hydrogen evolution;

The modification or modulation of the semiconductor surface with metal oxides, carbon-based materials, or polymers to achieve spatial separation of the semiconductor from the electrolyte;

Nanostructured construction for fast separation of holes on electrode surfaces.

The structural tunability of metal sulfides can enable researchers to obtain desired photoelectrochemical properties by adjusting the chemical composition and particle size parameters. However, these complex parameters imply a huge amount of screening work when selecting suitable electrodes. In this review, we simplified the main parameters for evaluating the photoelectrocatalytic performance as photocurrent density. Furthermore, photocurrent density ( $J_{\text{ph}}$ ) is mainly determined by light absorption efficiency ( $\eta_{\text{abs}}$ ), charge

separation efficiency ( $\eta_{\text{separation}}$ ), and charge injection efficiency ( $\eta_{\text{injection}}$ ) (Eq. 5).

$$J_{ph} = \eta_{abs} \times \eta_{separation} \times \eta_{injection} \quad (5)$$

Specifically for oxygen reduction reaction, relevant stages in photoelectrochemical reduction are: (1) light absorption by a semiconductor, (2) charge separation within the semiconductor structure, (3) charge transfer to the back contact, and (4) charge transfer to the liquid medium and carry out oxygen reduction reaction (Figure 3). The first step corresponds to the light absorption efficiency. The second and third steps are related to the charge separation efficiency. The fourth step is related to the charge injection efficiency. Based on these three crucial parameters, solutions such as morphology control, heteroatom doping, surface modification, and cocatalyst modification are proposed, which will inspire the design and preparation strategies for not only metal sulfides but also various high-performance photocatalysts.

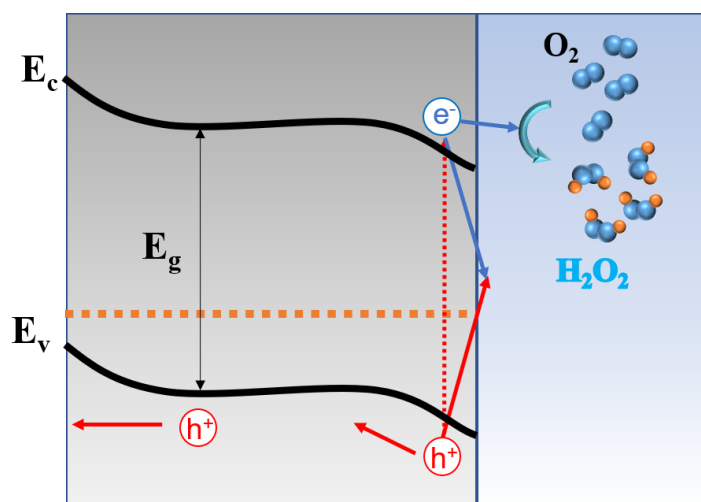


**Figure 3.** Structure of a photoelectrochemical cell based on a p-type semiconductor.

#### 4. Strategies for improving photoelectrocatalytic performance

For photocatalysts, the research on light absorption efficiency mainly focuses on the effect of energy band structure and material structure. Most metal sulfide photoelectrodes (except for ZnS and MnS) could absorb visible light since their band gaps are lower than 3.0 eV. Moreover, metal oxides generally can only absorb and utilize ultraviolet light due to their large bandgap (>3.0 eV) [31]. The energy of ultraviolet light accounts for only about 2% of the irradiated solar spectra, compared to about 47% for visible light (Figure 5) [32]. This

means that the utilization rate of sunlight by metal sulfides is higher than that of most metal oxides. More importantly,  $\text{H}_2\text{O}_2$  decomposes easily under UV light, so for the accumulation of  $\text{H}_2\text{O}_2$ , the reaction needs to be carried out under visible light.

However, when the bandgap is narrower, photogenerated electrons and holes are also more likely to compound, resulting in a lower photogenerated current density. In addition, the poor chemical stability of the sulfide material makes it prone to photocorrosion. To address these issues, appropriate modifications are essential.

It should be noticed that, for a comprehensive introduction to the modification strategy, some cases are not metal sulfide. But these strategies are general, and these strategies can also be used to enhance the photogenerated currents of metal sulfide.

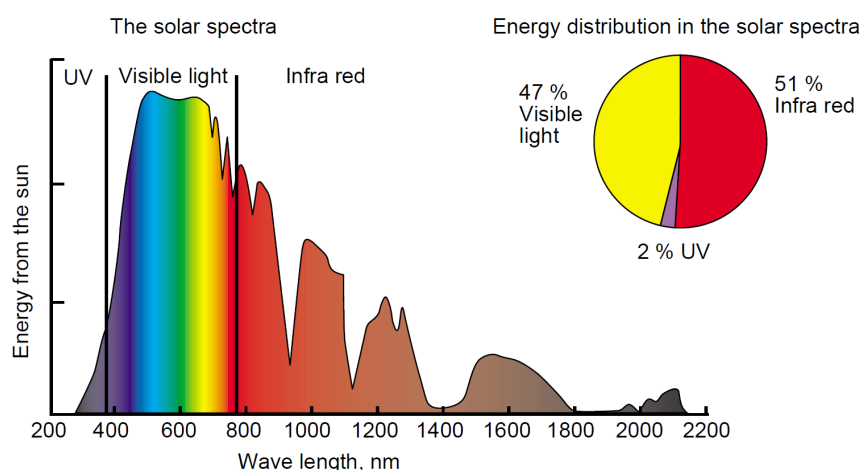


**Figure 4.** Solar spectra and energy content of visible light, IR and UV parts of the sunlight [32].

## 4.1 Light absorption efficiency

### 4.1.1 3D structures construct

In order to obtain efficient photocatalysts, the photoelectrode film material should be thick enough to absorb more light, and at the same time, the photogenerated carriers in the photoelectrode should be able to reach the interface participating in the catalytic reaction. Therefore, the minority carrier diffusion length is crucial for carrier transport. The morphology of the photoelectrode will affect the transport distance of photogenerated carriers. Compared with conventional semiconductor photoelectrodes, the potential advantages of one-dimensional (1D) nanostructured photoelectrodes are that the transfer distance of minority carriers is relatively short, so the morphology control of



photoelectrodes is particularly important [33]. It is the preparation of porous structures or 1D nanostructures such as nanorods, nanotubes and nanowires that has attracted much attention. In addition, the increase of surface reactive sites helps to reduce the charge recombination of the material and improve its PEC performance.

Liu et al. [34] demonstrated a typical method for synthesizing ZnO nanorod arrays and explained the working mechanism of the nanorod array (Figure 5). ZnO nanorod arrays (NRAs) were synthesized by a hydrothermal method, and their size could be controlled by adjusting the concentrations of reactants. Multiple scattering of UV light between ZnO NRAs, resulting in increased light absorption. Due to the high density of nanorods, little light scattering occurs on Z100, which can also be verified in transmittance spectra. Furthermore, Z25 having the highest surface area ratio which provides the most reactive sites for photocatalysis. Combining these two factors, Z25 produces about three times the concentration of  $H_2O_2$  as Z100 in 360 min.

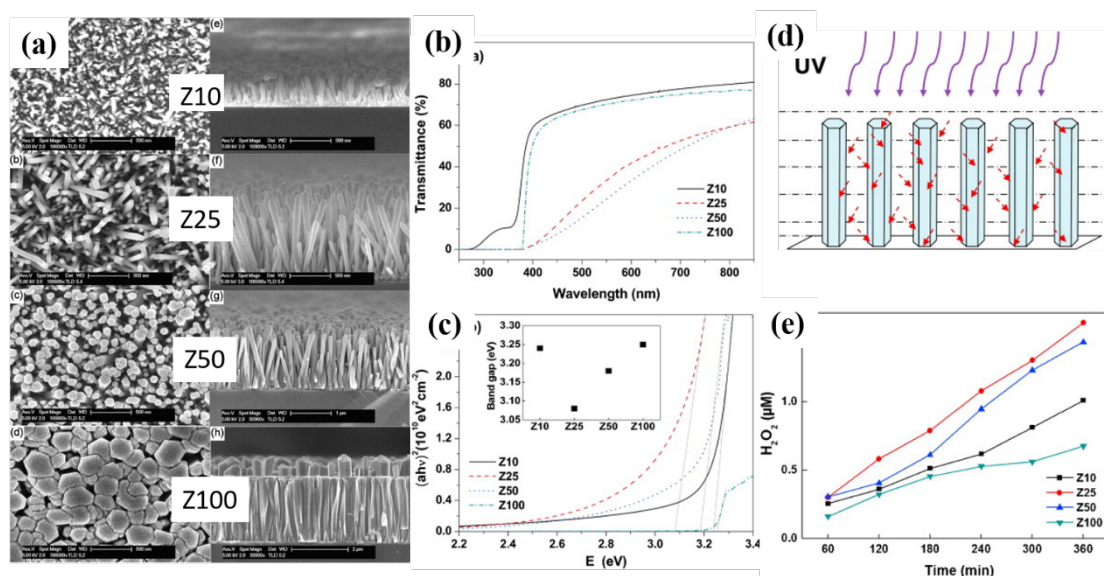


**Figure 5.** (a) SEM images of Z10, Z25, Z50 and Z100 (ZnO NRAs samples were named after their reactants' concentration as Z10, Z25, Z50 and Z100). (b) UV-vis transmittance spectra of the ZnO nanorod arrays. (c) Tauc plots for the ZnO nanorod arrays. The inset was the band gap data for different samples. (d) Schematic illustration of multiple scattering of light on ZnO nanorod arrays. (e)  $H_2O_2$  generated by the ZnO nanorod arrays under UV irradiation [34].

Besides nanorod arrays, there are other types of 3D structures, such as nanosheet arrays, pyramid arrays, etc., all of which aim to achieve better light absorption efficiency and reduce carrier recombination. Song et al. [35] prepared CdS nanoflakes (CdS NFAs)

using thermal evaporation as a substrate. Subsequently, the CdIn<sub>2</sub>S<sub>4</sub> surface layer was obtained by cation exchange of CdS NFAs in the presence of InCl<sub>3</sub> precursor at 500 °C (Figure 6). The formation of a type II heterojunction (Please see section 4.2.2 for details) by CdS NFAs and CdIn<sub>2</sub>S<sub>4</sub> layer improved the charge separation efficiency and hole injection rate, which resulted in enhanced photocurrent.

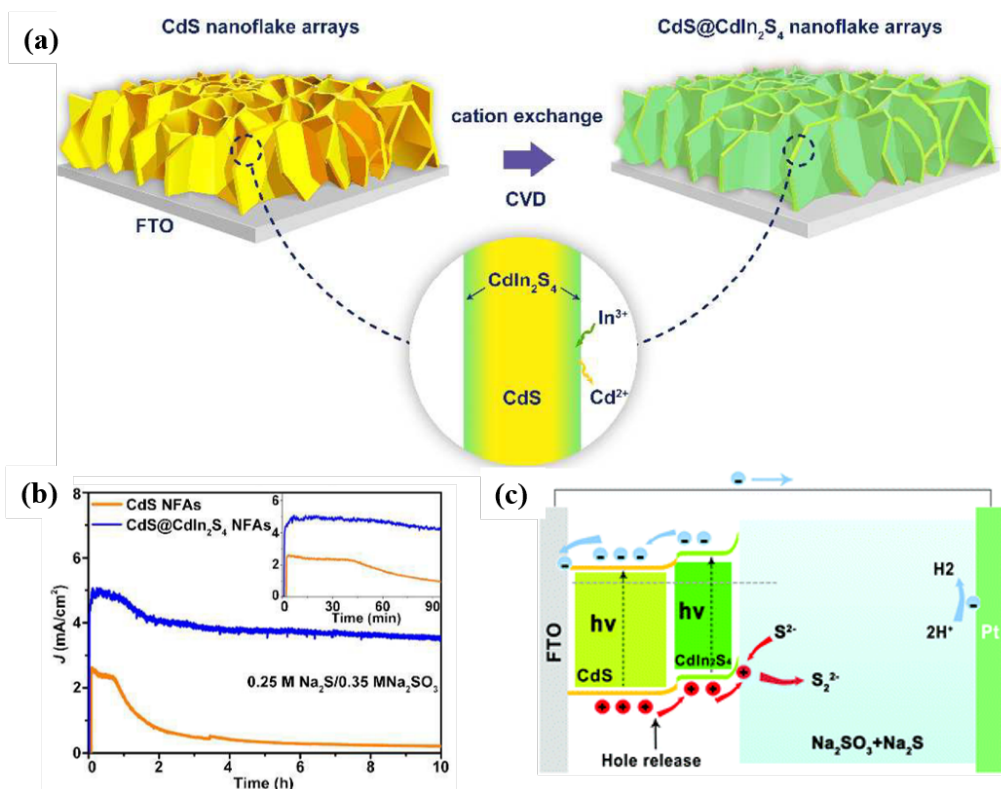


**Figure 6.** (a) Schematic illustration of CdS@CdIn<sub>2</sub>S<sub>4</sub> nanoflake preparation. (b) Time courses of the photocurrent of the CdS and CdS@CdIn<sub>2</sub>S<sub>4</sub> photoanodes. (c) Schematic illustration of CdS@CdIn<sub>2</sub>S<sub>4</sub> nanoflake for producing H<sub>2</sub> [35].

#### 4.1.2 Heteroatom doping

Doping of heteroatom ions is one of the most commonly used methods to improve the PEC performance of photoelectrode materials, which can be divided into metal ion doping and non-metal ion doping. And its effects can be summarized in the following four points:

By introducing additional electrons or holes, the carrier transport rate and separation efficiency inside the electrode can be improved;

The band structure of semiconductor materials can be adjusted to improve the utilization of light absorption;

The participation of heteroatom ions may also make conductivity of the material

increase, changing the onset potential;

The doping of heteroatom elements may also change the morphology of the material.

In addition, multi-element doping may produce synergistic effects to enhance the photocatalytic performance of semiconductor photocatalysts further.

The sulfur atoms in metal sulfide are often been substituted by the Se atoms, i.e., Cu(In, Ga)S<sub>2</sub> (CIGS) is frequently selenated to form Cu(In, Ga)(S, Se)<sub>2</sub> (CIGSSe) [36, 37]. Compared to metal oxides (bandgap of 2.2 - 3.5 eV), metal sulfides have significantly smaller bandgaps (bandgap of 1.1 - 2 eV) [30]. However, some sulfides, such as Cu<sub>2</sub>ZnSnS<sub>4</sub> (CZTS), have a too large bandgap value, which makes it impossible to absorb visible light sufficiently [38, 39]. To minimize the band gap, one approach is to partially replace sulfur with selenium. Since the energy of the Se 4p orbital is higher than that of the S 3p orbital, Se substitution can shift the valance band maximum (VBM) up and the conduction band minimum (CBM) down, thereby reducing the band gap.

Ge et al. [40] prepared BaCu<sub>2</sub>Sn(Se<sub>x</sub>S<sub>1-x</sub>)<sub>4</sub> (BCTSSe) films with different Se/S ratios using a co-sputtering method (Figure 7). It can be observed that as the ratio of selenium increases, the bandgap value of the material decreases nearly linearly. Compared with pure sulfide BCTS (when x = 0, FTO-1), the selenium-doped electrode exhibits improved photocurrent. This improvement stems from the addition of selenium reduces the band gap, resulting in the enhanced absorption efficacy of visible light.

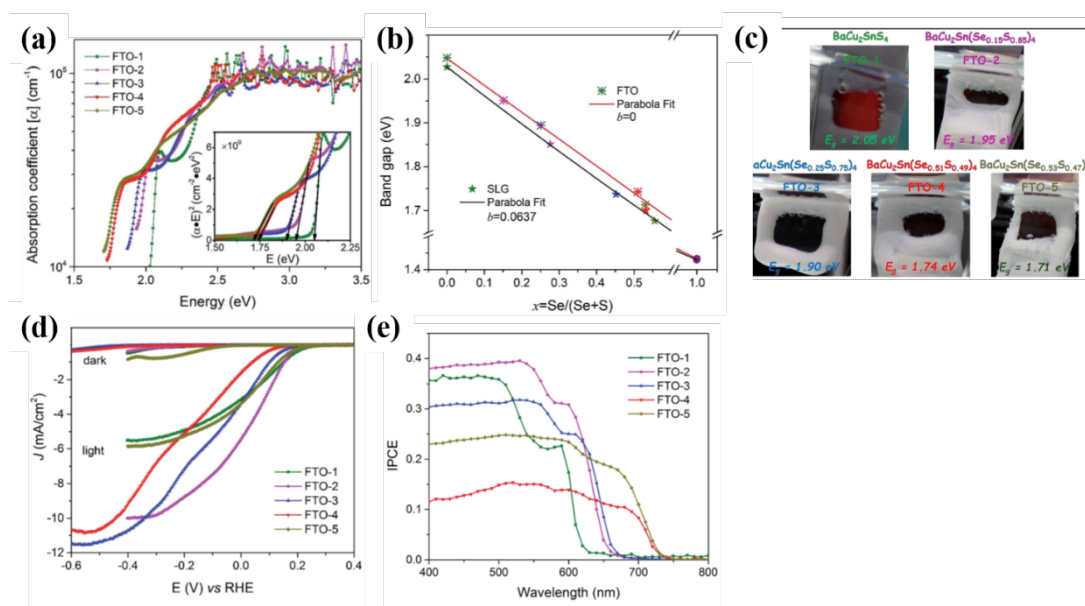


**Figure 7.** (a) Optical absorption coefficients of BCTSSe. (b) The band gaps of BCTSSe. (c) Photos of

BCTSSe photocathodes under PEC testing. (d) LSV curves of BCTSSe photocathodes. (e) IPCE spectra measured under 0 V vs. RHE [40].

Ikeda et al. [41] successfully prepared Cu(In, Ga)S<sub>2</sub> (CIGS) solid solutions with different Ga contents by spray pyrolysis-sulfurization process, and tested the performance of PEC based on CdS deposition layers and CIGS with different band gaps decorated with Pt nanoparticles (Figure 8). It can be found from the SEM images that when the molar ratio of Ga/(In+Ga) is 0.25, a significant increase in particle size is observed. With the increase of Ga content, the photocurrent density and onset potential of the bright pole gradually increased. As shown in Figure 12, when the molar ratio of Ga/(In+Ga) is 0.25, the Pt-CdS/CIGS(25) photocathode can obtain the maximum photocurrent density of -6.8 mA/cm<sup>2</sup> (0 V<sub>RHE</sub>) and the most positive onset potential of 0.89 V<sub>RHE</sub>. However, further increasing the Ga content is not conducive to improving the performance of PEC, which is attributed to the narrowing of the light absorption range due to the excessively large band gap.

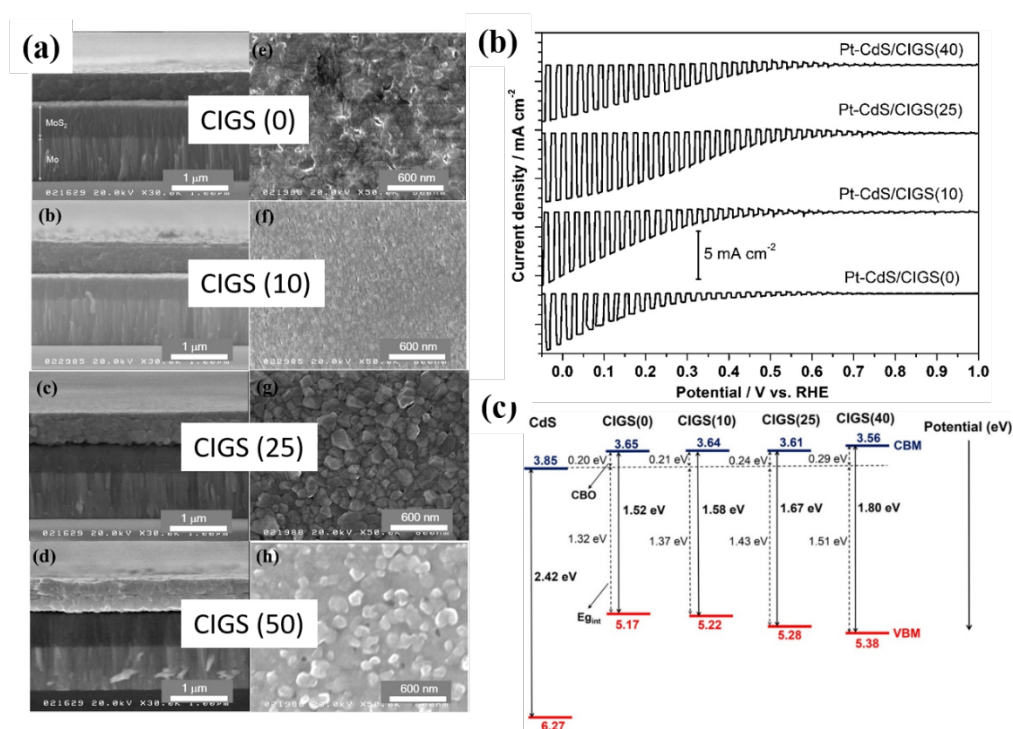


**Figure 8.** (a) SEM images of CIGS with different molar ratios of Ga/(In+Ga). (b) *J*-*V* curves of Pt-CdS/CIGS electrodes with different Ga contents. (c) Band positions of CIGS with different Ga contents [41].

## 4.2 Charge separation efficiency

### 4.2.1 Particle size and crystallinity

The particle size of the material is one of the important factors affecting the photogenerated current. Most of the time, the large-sized particles represent the excellent crystallinity of the material. The interface of contact between particles can lead to the formation of some recombination centers, so the formation of large particles is generally pursued for electrodes to obtain high photocurrent. In addition, large-sized particles generally possess good mechanical strength, which is crucial for their practical applications, such as the construction of tandem devices starting from nanostructures [30].

Chernomordik et al. systematically investigated the factors governing crystal growth and microstructure development during annealing of  $\text{Cu}_2\text{ZnSnS}_4$  (CZTS) films [42]. As shown in Figure 9, two competing mechanisms, normal grain growth and anomalous grain growth, affect the film microstructure. The temperature and time of annealing, sulfur vapor pressure, and the presence or absence of impurities can significantly affect grain growth and size.

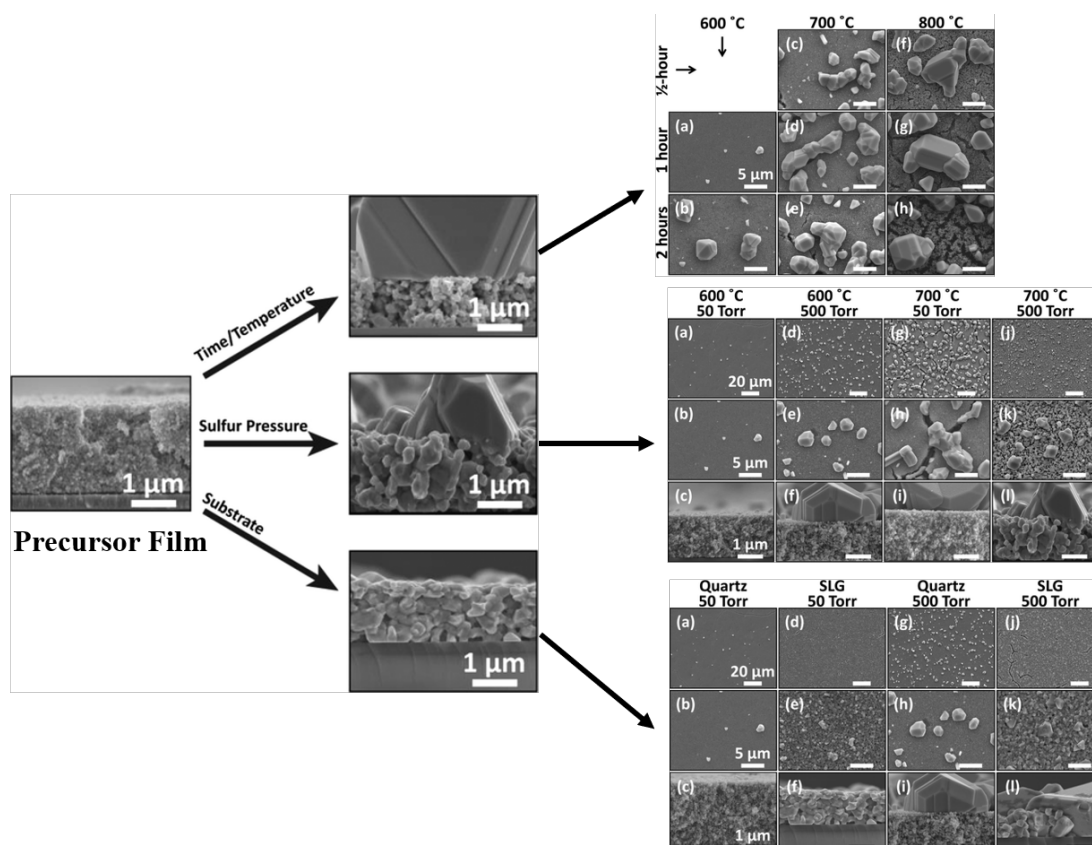


**Figure 9.** The effects of different annealing temperature, time, sulfur vapor pressure and substrate on the microstructure of CZTS thin films were observed by SEM images [42].

Liu et al. synthesized  $\text{BiVO}_4$  by solid-liquid state reaction, and controlled the particle size by adjusting the reaction time (Figure 10) [43]. The tightness of the contact between the  $\text{BiVO}_4$  particles and the FTO substrate affects the transfer of charges to the counter electrode. It thus affects parameters such as photocurrent, onset potential, and resistance. However, the charge separation efficiency plays a more significant role in the PEC reaction. The better performance of  $\text{BiVO}_4$  with large particle size in the oxygen evolution reaction can be attributed to two points: i) the decrease in particle size leads to a higher density of surface defect sites, resulting in more surface recombination centers; ii) large particles Dimensional  $\text{BiVO}_4$  has better charge separation efficiency based on the band bending induced by the space charge layer (SCL) [44]. It should be noted that a large particle size does not necessarily mean that the material is not tightly connected to the substrate. This problem can be effectively solved by using spin coating, ALD and other preparation methods.

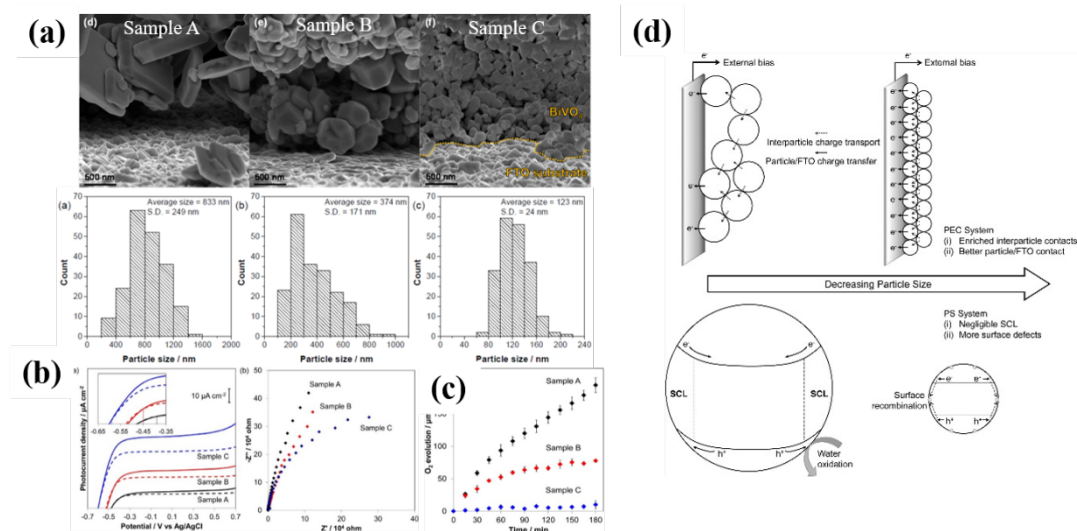


**Figure 10.** (a) Cross-section SEM micrographs of  $\text{BiVO}_4$  photoanode and corresponding particle size. (b) I-V curves under light (full line) and dark (dashed line) conditions and Nyquist plots. (c)  $\text{O}_2$  evolution reaction with time goes. (d) Different roles of particle size in controlling  $\text{BiVO}_4$  photoactivity in PEC and PS systems [43].

Qin et al. prepared  $\text{BiVO}_4$  photoanode with large particle size by chemical vapor deposition (CVD) method (Figure 11) [45]. The particle size of  $\text{BiVO}_4$  can be controlled by



adjusting the pH of the electrodeposition electrolyte of the Bi precursor. As the particle size increases, the photocurrent is significantly enhanced, which is attributed to the improved charge separation efficiency.

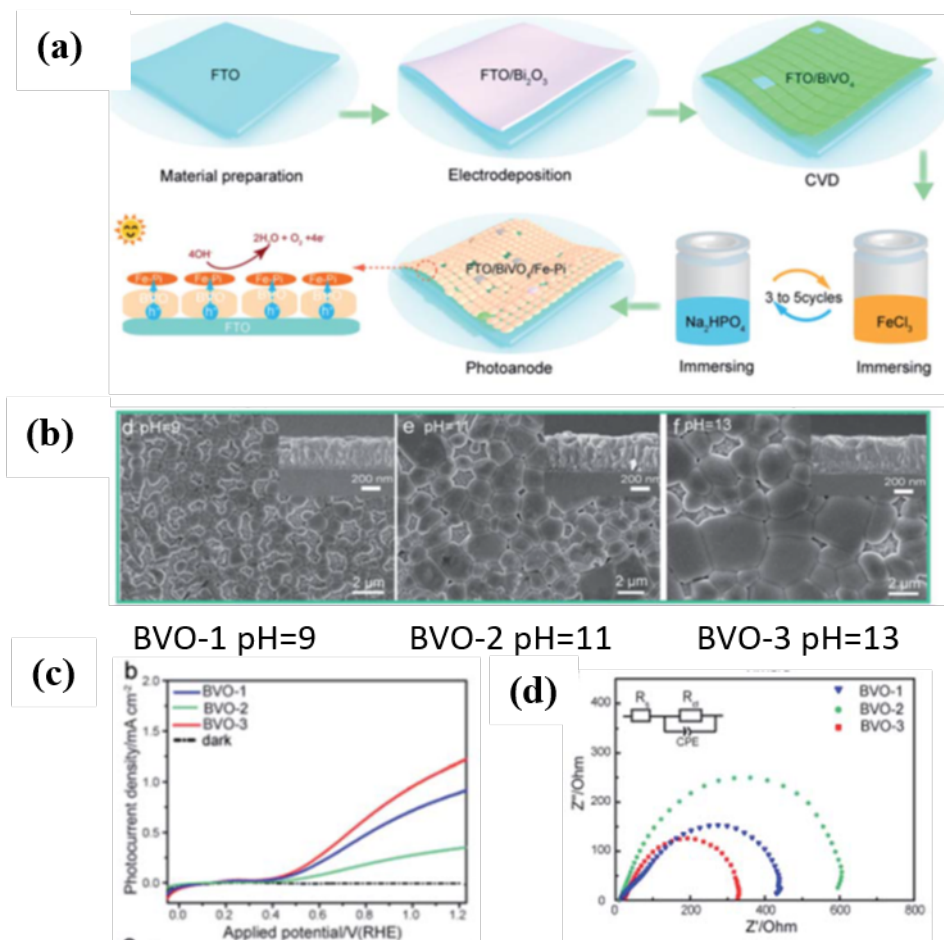


**Figure 11.** (a) Illustration of the preparation process. (b) SEM image of  $\text{BiVO}_4$  photoanodes. (c) J–V plot of  $\text{BiVO}_4$  photoanodes. (d) Nyquist plots of  $\text{BiVO}_4$  photoanodes [45].

#### 4.2.2 Heterojunction construction

Generally, conventional heterojunction photocatalysts are classified into three types (Figure 12), i.e., straddling gap (type I) [46], staggered gap (type II) [47–49], and broken gap (type III) [50, 51]. Among these three types of heterojunctions, type II heterojunction can enhance photocatalytic activity as it can effectively improve the charge separation efficiency. Nonetheless, since the reduction and oxidation processes occur on semiconductors with lower reduction and oxidation potentials, respectively, the redox capacity of photocatalysts is reduced [52]. To overcome this problem, Z-type heterojunctions are proposed, which can be divided into three categories, liquid-phase

Z-type heterojunctions [53], all-solid-state Z-type heterojunctions [54-59], and direct Z-type heterojunctions [60-62].

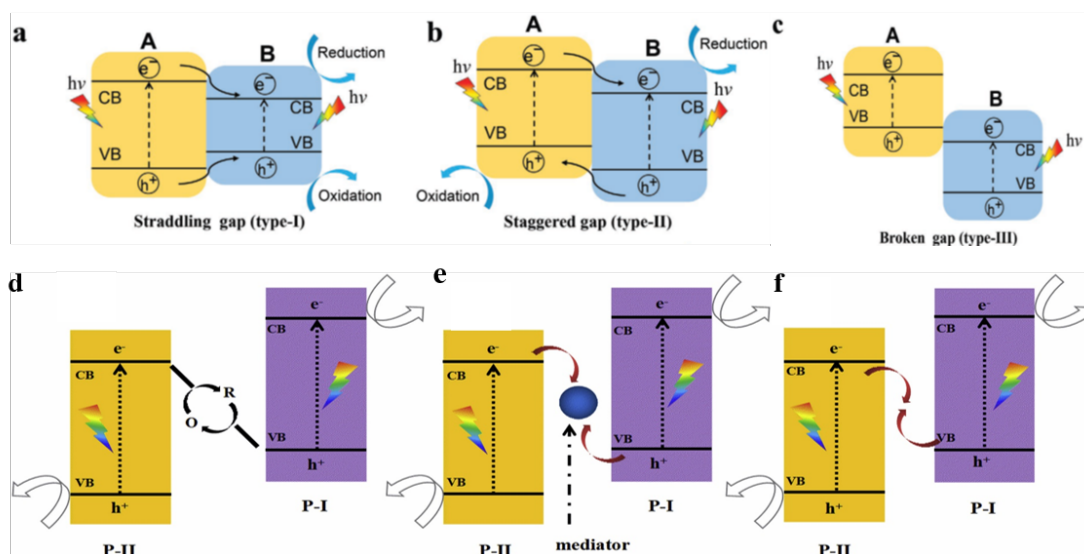


**Figure 12.** (a) type-I, (b) type-II, and (c) type-III heterojunctions. (d) liquid-phase Z-scheme heterojunction, (e) all-solid-state Z-scheme heterojunction, (f) direct Z-scheme heterojunction [53].

Wu et al. [63] synthesized  $\text{ZnIn}_2\text{S}_4$  (ZIS) photoanode by hydrothermal method, and P-doped ZIS was obtained by phosphine vapor phosphating (Figure 13). The n-type ZIS and p-type P-doped ZIS form a p-n heterojunction, which can be verified from the Mott-Schottky plot. Compared with the base ZIS, the photocurrent of the ZIS/P-ZIS is greatly improved, which is attributed to the excellent charge separation efficiency. Kumar et. al [62] report the fabrication of Z-scheme based core/shell/shell nanomaterials of  $\text{NaNbO}_3/\text{CuInS}_2/\text{In}_2\text{S}_3$  photoelectrode (Figure 13c). For comparison, the authors have also performed a modified  $\text{NaNbO}_3/\text{In}_2\text{S}_3/\text{CuInS}_2$  photoelectrode with type II heterostructure. The enhanced photocurrent density under visible light irradiation indicates that the Z-type system performs better than the type-II heterostructure. This is due to the reduced recombination of charge carriers by the Z-type system, revealed by the PL intensity and short lifetime.



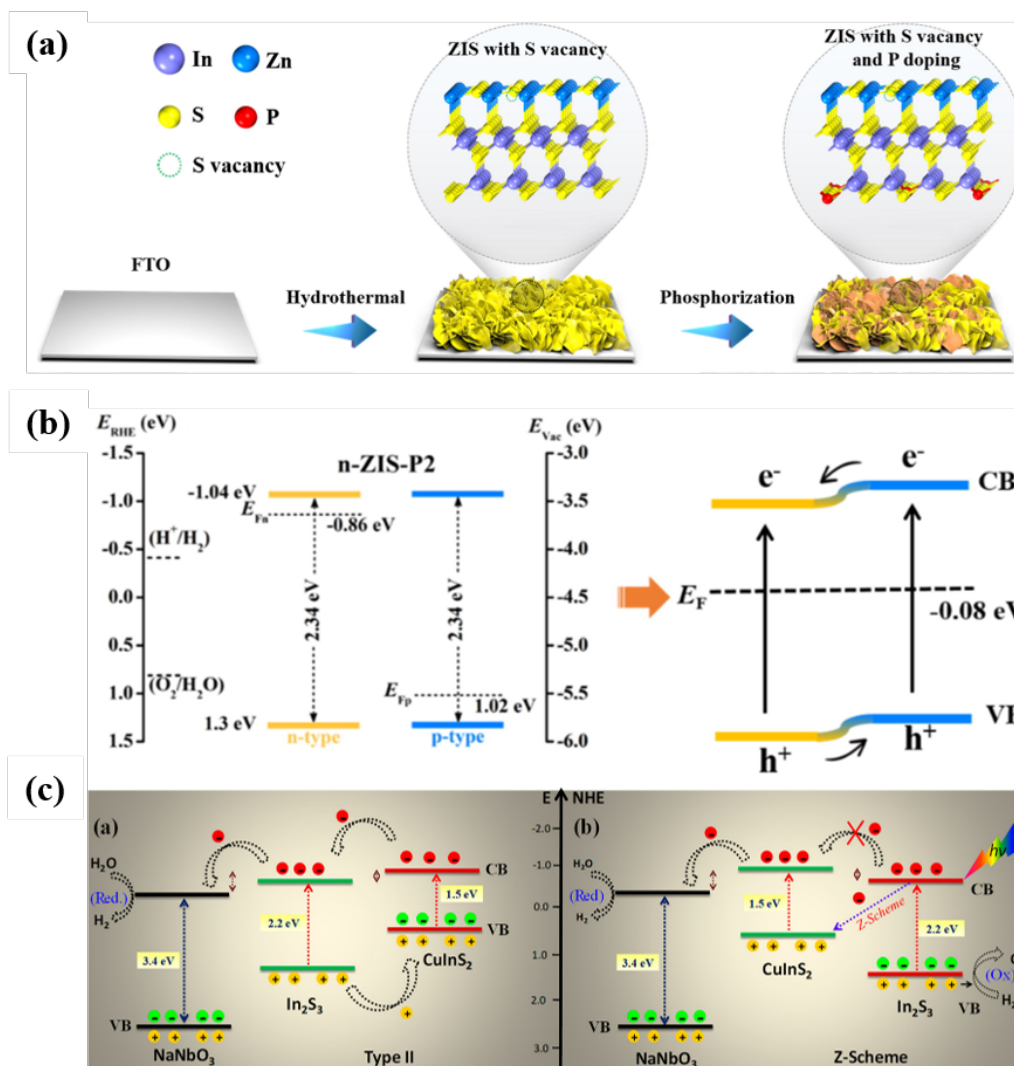


**Figure 13.** (a) The preparation process of ZIS photoanode. (b) The band structure alignment containing n- and p-type regions, and diagram for carrier transport of n-ZIS-P2 [63]. (c) Schematic of type II bandgap structure and Z-Scheme bandgap structure [62].

#### 4.2.3 Passivation layer modification

Since metal sulfide semiconductors are photoelectrochemically unstable, inert surface coatings such as  $TiO_2$  are required to improve the stability of photoelectrodes. Typically, the thickness of the passivation layer should be less than 100 nm to minimize the effect on light absorption and allow charge carriers to tunnel through it [64]. In addition, the passivation layer should be stable enough to not react with the electrolyte and not easily be reduced by electrons or oxidized by holes. Usually, the passivation layer does not provide a catalytic surface for the oxidation or reduction of water. Therefore, additional cocatalysts may be required to reduce the overpotential to generate efficient

photoelectrodes for oxygen reduction reactions. However, some passivation layers can also prevent electron-hole recombination, leading to fast interfacial charge transfer rates.

Wang et al. [65] prepared an Al-ZnO/CdS photoanode and deposited TiO<sub>2</sub> as a passivation layer through atomic layer deposition (ALD) to enhance the photostability (Figure 14). When the number of ALD cycles is small, the photocurrent is increased, which may be based on the enhancement of the charge transfer rate, and when the number of ALD cycles is high, the photocurrent is shown to decrease, which may be due to the affected light absorption. With the increasing of ALD cycles, the photostability of photoanodes are extended. In addition to acting as a passivation layer to physically isolate the contact between the electrode and the electrolyte, TiO<sub>2</sub> also prevents electron-hole recombination and improves the charge separation efficiency.

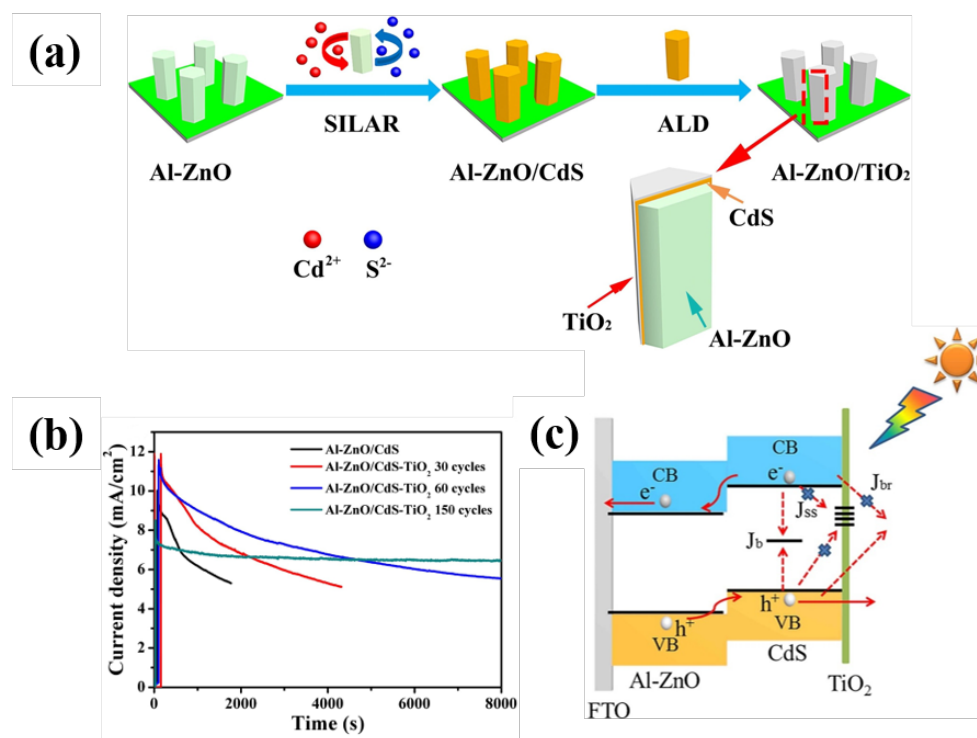


**Figure 14.** (a) Schematic diagram of the fabrication of Al-ZnO/CdS/TiO<sub>2</sub> photoanode. (b) Stability measurement. (c) Bandgap structure of Al-ZnO/CdS/TiO<sub>2</sub> photoanode [65].

#### 4.2.4 Conductive layer modification

The metal layer can form a Schottky junction with the semiconductor, where the equilibrium arrangement of the Fermi level ( $E_F$ ) of the metal and the semiconductor creates a built-in electric field in the depletion region near the interface [66]. Driven by this

electric field, photoexcited electrons from the semiconductor are transferred to the metal layer (Figure 15). The Schottky barrier not only promotes the separation of photogenerated electrons and holes, but also inhibits the recombination of photogenerated charge carriers on the semiconductor surface. The metal layer also physically isolates the electrode from the electrolyte and provides active sites for the photocatalytic reduction reaction.

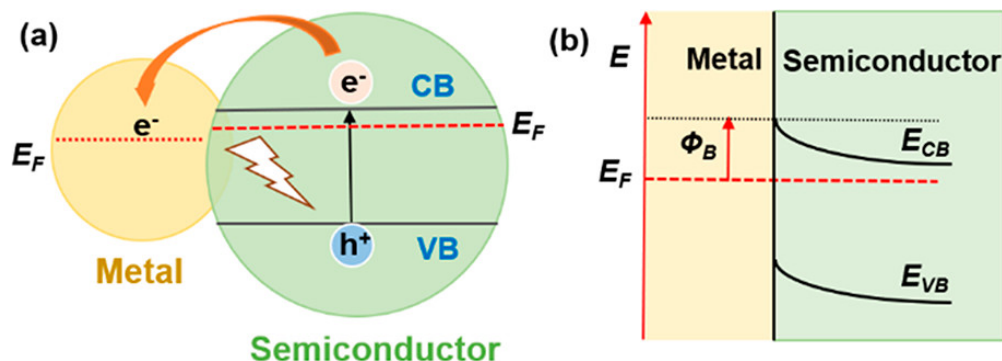


**Figure 15.** (a) Schematic diagram of electron transfer between semiconductor and metal layers under light irradiation. (b) Schematic diagram of Schottky barrier formation [66].

Kumagai et al. [67] reported the effects of the conductive layers on the  $\text{Cu}(\text{In,Ga})\text{Se}_2$  (CIGS) photocathodes (Figure 16). In this study, the degree of contact between the Pt particles and the photocathode was enhanced by inserting a Mo layer at the interface between the two phases. The Ti layer acts as a protective layer to isolate the contact between the electrode and the electrolyte. As a result, the Pt/Mo/Ti/CdS/CIGS electrode exhibited an enhanced photocurrent density and stability compared with the base CIGS photocathode.

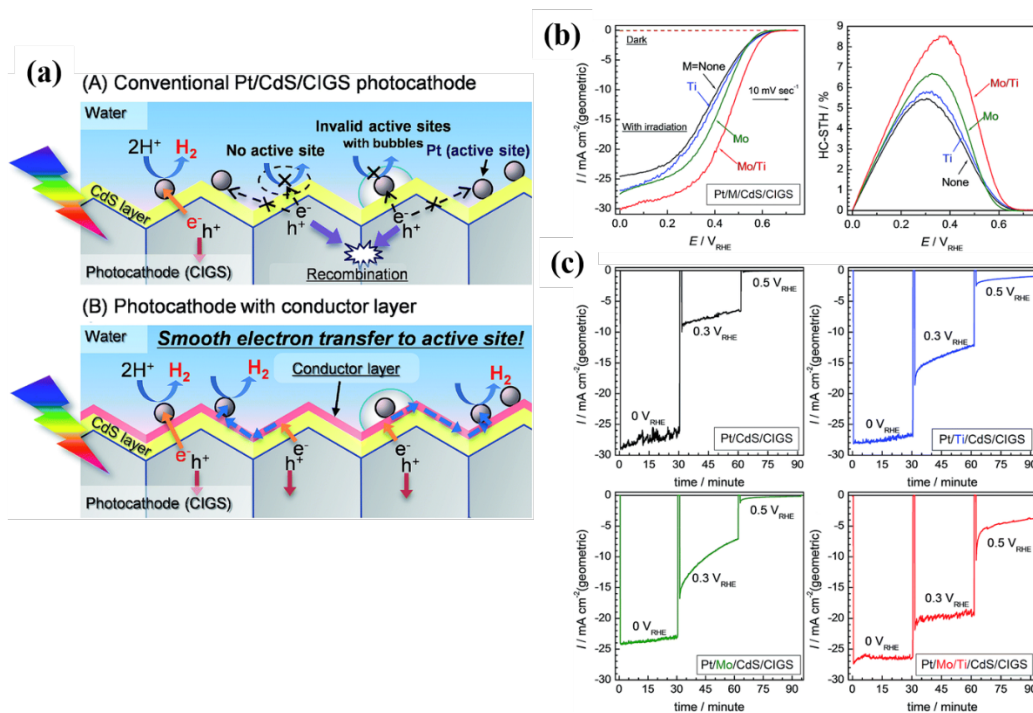


**Figure 16.** (a) A possible mechanism for Pt/CdS/CIGS and Pt/Mo/Ti/CdS/CIGS photocathodes. (b) *J-V* curves and corresponding HC-STH values of Pt/M/CdS/CIGS electrodes. (c) Current–time plots of conductive layers modified CIGS electrodes under different potentials [67].

## 4.3 Charge injection efficiency

### 4.3.1 Co-catalyst modification

Co-catalyst modification is one of the important means to improve the PEC performance of the photoelectrode [68]. Appropriate co-catalysts can effectively reduce the activation energy required for the reaction and reduce the adsorption energy to the reactants, thereby increasing the reaction rate and increasing the selectivity of the reaction. At the same time, the co-catalyst also acts as an oxidation or reduction center, so that the carriers are concentrated on the surface of the co-catalyst, thereby protecting the electrode from photocorrosion and improving the photostability of the electrode. There are many types of co-catalysts [69, 70], and the most used are noble metal catalysts such as Au [71] and Pt [72], etc. Due to its high cost, it later began to explore transition metals [73, 74] and alloys [75, 76] co-catalysts. In addition, metal oxides [77], metal hydroxides [78], metal phosphides [79], metal sulfides [80], carbon-based materials [81, 82], biological enzyme [83] cocatalysts, etc., have also been significantly developed. Among these cocatalysts, noble metal nanoparticles (NPs) deposition, such as Au NPs, show

surface plasmon resonance (SPR) effect, which is one of the most common ways to extend the light absorption range of semiconductors [69]. The visible light absorption range can be tuned by changing conditions such as the morphology and size of noble metal nanoparticles.

Hirakawa et al. [19] synthesis Au/BiVO<sub>4</sub> photocatalytic for H<sub>2</sub>O<sub>2</sub> production by a direct two-electron reduction of oxygen (Figure 17). In the UV-Vis absorption spectra, Au<sub>0.2</sub>/BiVO<sub>4</sub> showed visible light absorption at about 600 nm compared with bare BiVO<sub>4</sub>, which was attributed to the SPR of Au particles. The calcination temperature and the amount of Au doping have a significant impact on the size of Au particles, which in turn directly affects the amount of H<sub>2</sub>O<sub>2</sub> generated. Comparative experiments show that smaller Au particles could generate H<sub>2</sub>O<sub>2</sub> more efficiently.

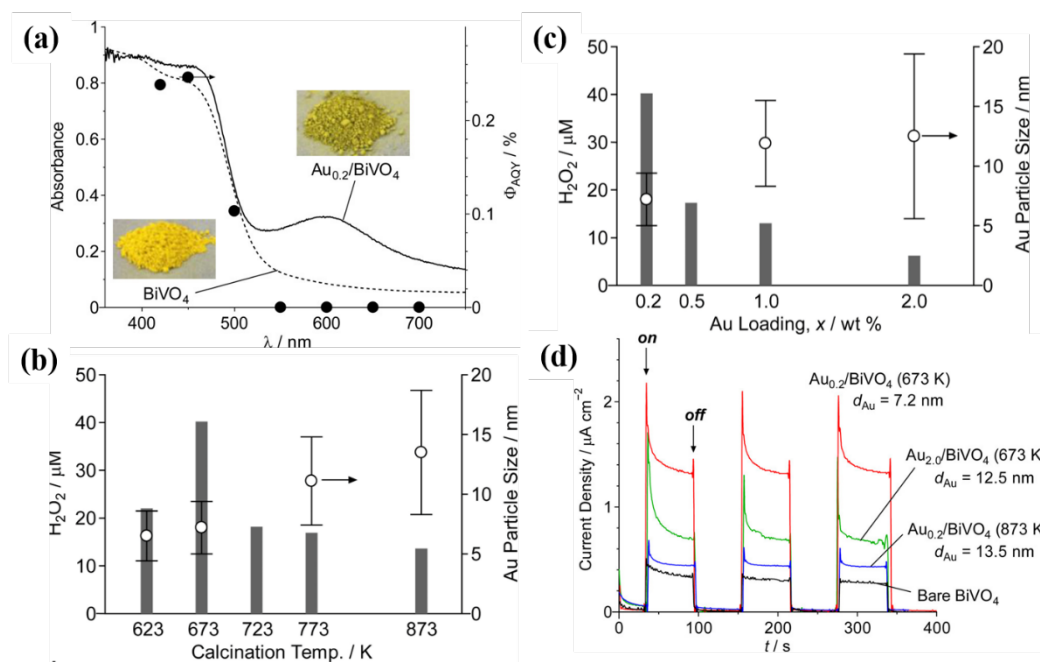


**Figure 17.** (a) Absorption spectra of BiVO<sub>4</sub> and 0.2 wt% Au loaded BiVO<sub>4</sub>. (b) Effects of calcination temperature. (c) Effects of Au loaded amount. (d) Photocurrent response [19].

After loading Pd nanoparticles on BiVO<sub>4</sub>, Fuku et al. [20] found that Pd/BiVO<sub>4</sub> could efficiently generate H<sub>2</sub>O<sub>2</sub> from water and O<sub>2</sub> under visible light irradiation (Figure 18). After screening a series of metal cocatalysts, it was found that Pd has the highest oxygen reduction activity. By control the amount of loaded smaller Pd NPs supported selectively on the reductive surfaces of the BiVO<sub>4</sub> facilitate H<sub>2</sub>O<sub>2</sub> production from O<sub>2</sub>. The authors found that smaller size Pd NPs were deposited on the reduced surface of BiVO<sub>4</sub> by

phosphate ion coating. The smaller Pd NPs promoted  $\text{H}_2\text{O}_2$  generation synergistically by catalyzing the  $2\text{e}^-$  reduction of  $\text{O}_2$ , while simultaneously inhibiting the  $4\text{e}^-$  reduction of  $\text{O}_2$  and the two-electron reduction of  $\text{H}_2\text{O}_2$  to  $\text{H}_2\text{O}$ .

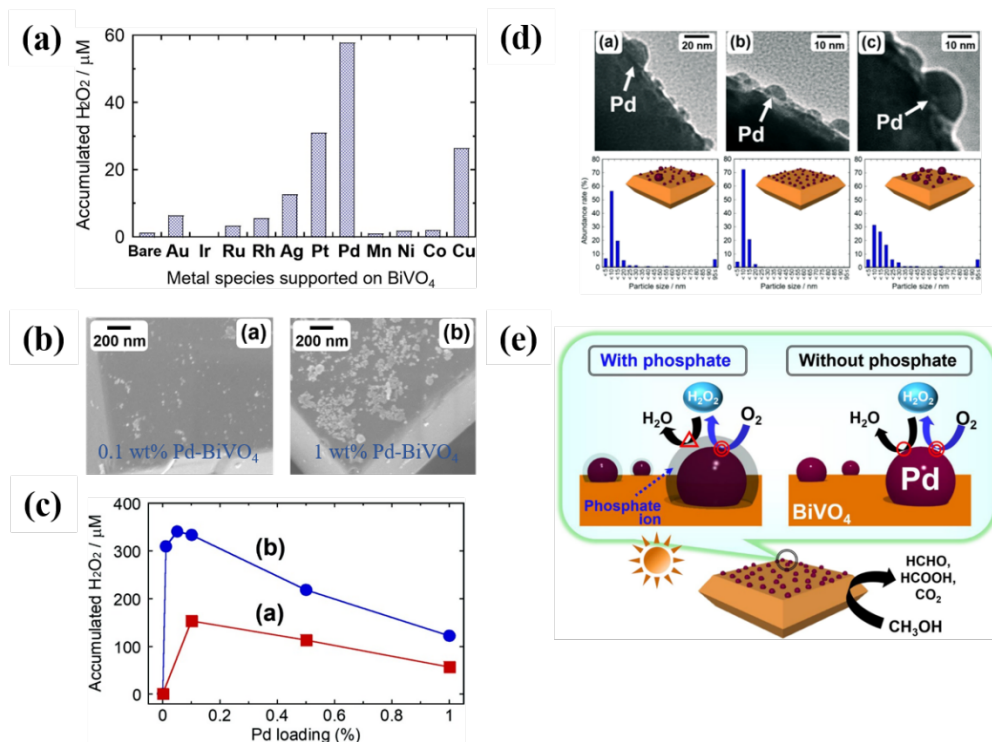


**Figure 18.** (a) Effects of metal co-catalyst species. (b) SEM images of 0.1 wt% and 1.0 wt% Pd- $\text{BiVO}_4$ . (c) Effects of Pd loading using IMP (red line) and PAD (blue line) methods. (d) TEM images, size distributions of Pd NPs prepared using the PAD method at different pH value. (e) Proposed mechanism [20].

### 4.3.2 Facet engineering

Zhang et al. [84] predicted the effect of different crystal planes of  $\text{Cu}_2\text{ZnSnS}_4$  (CZTS) on the hydrogen evolution reaction by density functional theory (DFT) calculations (Figure 19). For CZTS, there are usually several identifiable crystal planes (112), (220) and (312). The adsorption sites of hydrogen ions on all faces were observed to be on top of the S atoms. However, the free energy of hydrogen ions on different crystal planes is different, which also brings about changes in adsorption energy. Overall, (220) has the smallest free energy and is expected to have the best hydrogen evolution efficiency.



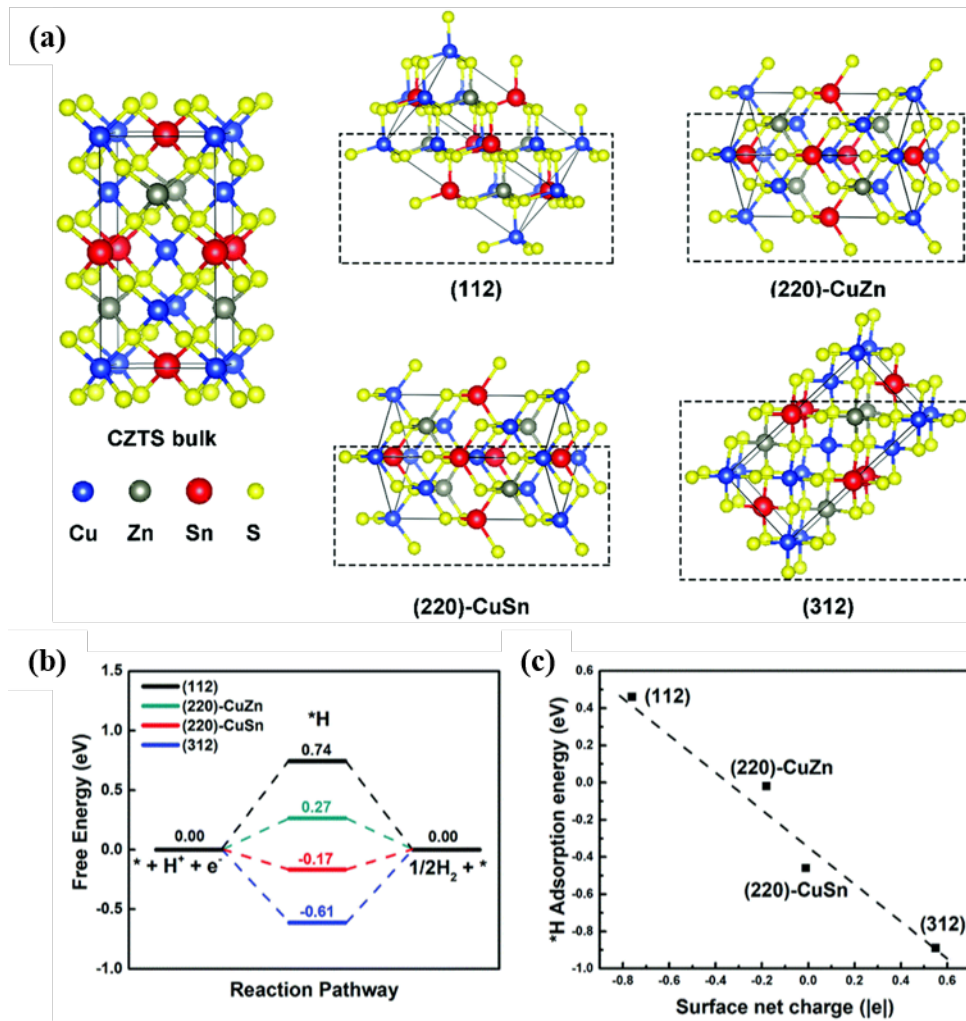


**Figure 19.** (a) Schematic of the CZTS structure and different facets. (b) The free energy on different facets for hydrogen evolution reaction. (c) The  $*H$  adsorption energy-surface net charge plot for different facets [84].

## 5. Summary

Photoelectrocatalytic  $H_2O_2$  generation is a promising method for the direct conversion of solar energy into chemical energy. Metal sulfides as photocathodes have the advantages of suitable band gap values, high absorption coefficients, fast charge carrier kinetics, and structural tunability. However, metal sulfides are also limited by factors such as photocorrosion, which requires necessary modifications to enhance their stability and  $H_2O_2$  production rate. Therefore, here we focus on modification strategies and simplify the main parameter for assessing photocatalytic performance to the photocurrent density. Furthermore, photocurrent density ( $J_{ph}$ ) is mainly determined by light absorption efficiency ( $\eta_{abs}$ ), charge separation efficiency ( $\eta_{separation}$ ), and charge injection efficiency ( $\eta_{injection}$ ).

Based on these three key parameters, a series of strategies are summarized for improving the PEC performance of metal sulfide electrodes.

( i ) In order to achieve high light absorption efficiency, a suitable band gap and good light absorption are necessary, for which heteroatom doping and methods of constructing 3D structures can be used. In addition, the SPR effect caused by noble metal loading can also increase light absorption to a certain extent.

( ii ) In order to improve the charge separation efficiency, it is necessary to reduce the recombination of electrons and holes as much as possible and increase the carrier transport rate. Large-sized particles, metal ion doping, heterostructure construction, and modification of protective or conductive layers are all effective methods to improve charge separation efficiency.

( iii ) In order to improve the efficiency of charge injection, the most commonly used methods are cocatalyst modification and facet engineering.

It is worth noting that these methods of improving PEC performance may affect more than one parameter, so photoelectrodes are often modified in multiple ways. In addition, the stability of metal sulfide electrodes can also be improved based on the above strategies, for example, using a protective layer or conductive layer to physically isolate the photoelectrode from the electrolyte; using a cocatalyst to remove photogenerated holes to achieve the effect of protection.

## **6. Research perspectives**

The purpose of this study was to reduce the cost of preparing hydrogen peroxide by the PEC method and to make it competitive with the AQ method in the future.  $\text{Cu}_3\text{BiS}_3$  (CBS) and  $\text{Cu}_3\text{VS}_4$  (CVS) were selected as photocathodes in this thesis since they are safe, non-toxic, rich in constituent elements, and inexpensive. Spray pyrolysis was employed for electrode preparation since it is cost-effective, can be applied on a large scale, and has a fast deposition rate.

Although both materials possess suitable conduction band values and bandgaps, they do not appear to possess high photocurrent densities and high stability. In order to improve the efficiency of charge separation and injection, further modifications have to be



made to the electrodes. In the following work, we applied these modification strategies to the prepared CBS and CVS photocathodes and effectively increased the photocurrent density. With further research, we believe that it will be possible to achieve an environmentally friendly and cost-effective industrial generation of hydrogen peroxide through the PEC method.

## References

- [1] D. Kim, K.K. Sakimoto, D. Hong, P. Yang, Artificial photosynthesis for sustainable fuel and chemical production, *Angew Chem Int Ed Engl*, 54 (2015) 3259-3266.
- [2] J. Gong, C. Li, M.R. Wasielewski, Advances in solar energy conversion, *Chem Soc Rev*, 48 (2019) 1862-1864.
- [3] S.D. Tilley, Recent Advances and Emerging Trends in Photo-Electrochemical Solar Energy Conversion, *Advanced Energy Materials*, 9 (2019).
- [4] K.B. Ashurov, B.M. Abdurakhmanov, S.C. Iskandarov, T.K. Turdaliev, A.M. Salimboev, M.M. Adilov, I.J. Abdusaidov, Solving the Problem of Energy Storage for Solar Photovoltaic Plants (Review), *Applied Solar Energy*, 55 (2019) 119-125.
- [5] Z. Wang, C. Li, K. Domen, Recent developments in heterogeneous photocatalysts for solar-driven overall water splitting, *Chem Soc Rev*, 48 (2019) 2109-2125.
- [6] Q. Wang, M. Nakabayashi, T. Hisatomi, S. Sun, S. Akiyama, Z. Wang, Z. Pan, X. Xiao, T. Watanabe, T. Yamada, N. Shibata, T. Takata, K. Domen, Oxysulfide photocatalyst for visible-light-driven overall water splitting, *Nat Mater*, 18 (2019) 827-832.
- [7] S. Chen, T. Takata, K. Domen, Particulate photocatalysts for overall water splitting, *Nature Reviews Materials*, 2 (2017).
- [8] Y. Zhao, G.I.N. Waterhouse, G. Chen, X. Xiong, L.Z. Wu, C.H. Tung, T. Zhang, Two-dimensional-related catalytic materials for solar-driven conversion of CO<sub>x</sub> into valuable chemical feedstocks, *Chem Soc Rev*, 48 (2019) 1972-2010.
- [9] L. Ye, Y. Deng, L. Wang, H. Xie, F. Su, Bismuth-Based Photocatalysts for Solar Photocatalytic Carbon Dioxide Conversion, *ChemSusChem*, 12 (2019) 3671-3701.
- [10] R.J. Lewis, G.J. Hutchings, Recent Advances in the Direct Synthesis of H<sub>2</sub>O<sub>2</sub>, *ChemCatChem*, 11 (2018) 298-308.
- [11] X. Geng, L. Wang, L. Zhang, H. Wang, Y. Peng, Z. Bian, H<sub>2</sub>O<sub>2</sub> production and in situ sterilization over a ZnO/g-C<sub>3</sub>N<sub>4</sub> heterojunction photocatalyst, *Chemical Engineering Journal*, 420 (2021).
- [12] J. Xu, X. Zheng, Z. Feng, Z. Lu, Z. Zhang, W. Huang, Y. Li, D. Vuckovic, Y. Li, S. Dai, G. Chen, K. Wang, H. Wang, J.K. Chen, W. Mitch, Y. Cui, Organic wastewater treatment by a single-atom catalyst and electrolytically produced H<sub>2</sub>O<sub>2</sub>, *Nat Sustain*, 4 (2021) 233-241.
- [13] K. Sahel, L. Elsellami, I. Mirali, F. Dappozze, M. Bouhent, C. Guillard, Hydrogen peroxide and photocatalysis, *Applied Catalysis B: Environmental*, 188 (2016) 106-112.
- [14] Y. Xue, Y. Wang, Z. Pan, K. Sayama, Electrochemical and Photoelectrochemical Water Oxidation for Hydrogen Peroxide Production, *Angew Chem Int Ed Engl*, 60 (2021) 10469-10480.
- [15] W. Fan, B. Zhang, X. Wang, W. Ma, D. Li, Z. Wang, M. Dupuis, J. Shi, S. Liao, C. Li, Efficient hydrogen peroxide synthesis by metal-free polyterthiophene via photoelectrocatalytic dioxygen reduction, *Energy & Environmental Science*, 13 (2020) 238-245.
- [16] Z. Teng, W. Cai, T. Ohno, Functionalized Graphitic Carbon Nitrides for Photocatalytic H<sub>2</sub>O<sub>2</sub> Production: Desired Properties Leading to Rational Catalyst Design, *KONA Powder and Particle Journal*, (2022).
- [17] A. Fujishima, K. Honda, Electrochemical Photolysis of Water at a Semiconductor Electrode, *Nature*, 238 (1972) 37-38.

- [18] Z. Haider, H.-i. Cho, G.-h. Moon, H.-i. Kim, Minireview: Selective production of hydrogen peroxide as a clean oxidant over structurally tailored carbon nitride photocatalysts, *Catalysis Today*, 335 (2019) 55-64.
- [19] H. Hirakawa, S. Shiota, Y. Shiraishi, H. Sakamoto, S. Ichikawa, T. Hirai, Au Nanoparticles Supported on BiVO<sub>4</sub>: Effective Inorganic Photocatalysts for H<sub>2</sub>O<sub>2</sub> Production from Water and O<sub>2</sub> under Visible Light, *ACS Catalysis*, 6 (2016) 4976-4982.
- [20] K. Fuku, R. Takioka, K. Iwamura, M. Todoroki, K. Sayama, N. Ikenaga, Photocatalytic H<sub>2</sub>O<sub>2</sub> production from O<sub>2</sub> under visible light irradiation over phosphate ion-coated Pd nanoparticles-supported BiVO<sub>4</sub>, *Applied Catalysis B: Environmental*, 272 (2020).
- [21] T. Liu, Z. Pan, J.J.M. Vequizo, K. Kato, B. Wu, A. Yamakata, K. Katayama, B. Chen, C. Chu, K. Domen, Overall photosynthesis of H<sub>2</sub>O<sub>2</sub> by an inorganic semiconductor, *Nat Commun*, 13 (2022) 1034.
- [22] Z. Teng, Q. Zhang, H. Yang, K. Kato, W. Yang, Y.-R. Lu, S. Liu, C. Wang, A. Yamakata, C. Su, B. Liu, T. Ohno, Author Correction: Atomically dispersed antimony on carbon nitride for the artificial photosynthesis of hydrogen peroxide, *Nature Catalysis*, 4 (2021) 533-533.
- [23] Q. Wu, J. Cao, X. Wang, Y. Liu, Y. Zhao, H. Wang, Y. Liu, H. Huang, F. Liao, M. Shao, Z. Kang, Author Correction: A metal-free photocatalyst for highly efficient hydrogen peroxide photoproduction in real seawater, *Nat Commun*, 12 (2021) 1187.
- [24] X. Wang, K. Maeda, A. Thomas, K. Takanabe, G. Xin, J.M. Carlsson, K. Domen, M. Antonietti, A metal-free polymeric photocatalyst for hydrogen production from water under visible light, *Nat Mater*, 8 (2009) 76-80.
- [25] J. Xiao, Q. Han, Y. Xie, J. Yang, Q. Su, Y. Chen, H. Cao, Is C<sub>3</sub>N<sub>4</sub> Chemically Stable toward Reactive Oxygen Species in Sunlight-Driven Water Treatment?, *Environ Sci Technol*, 51 (2017) 13380-13387.
- [26] J. Liu, Y. Zou, B. Jin, K. Zhang, J.H. Park, Hydrogen Peroxide Production from Solar Water Oxidation, *ACS Energy Letters*, 4 (2019) 3018-3027.
- [27] K. Fuku, Y. Miyase, Y. Miseki, T. Gunji, K. Sayama, WO<sub>3</sub>/BiVO<sub>4</sub> photoanode coated with mesoporous Al<sub>2</sub>O<sub>3</sub> layer for oxidative production of hydrogen peroxide from water with high selectivity, *RSC Adv.*, 7 (2017) 47619-47623.
- [28] S. Jin, X. Ma, J. Pan, C. Zhu, S.E. Saji, J. Hu, X. Xu, L. Sun, Z. Yin, Oxygen vacancies activating surface reactivity to favor charge separation and transfer in nanoporous BiVO<sub>4</sub> photoanodes, *Applied Catalysis B: Environmental*, 281 (2021).
- [29] C.Y. Toe, S. Zhou, M. Gunawan, X. Lu, Y.H. Ng, R. Amal, Recent advances and the design criteria of metal sulfide photocathodes and photoanodes for photoelectrocatalysis, *Journal of Materials Chemistry A*, 9 (2021) 20277-20319.
- [30] C. Chen, M. Yasugi, L. Yu, Z. Teng, T. Ohno, Visible light-driven H<sub>2</sub>O<sub>2</sub> synthesis by a Cu<sub>3</sub>BiS<sub>3</sub> photocathode via a photoelectrochemical indirect two-electron oxygen reduction reaction, *Applied Catalysis B: Environmental*, 307 (2022).
- [31] L. Cheng, Q. Xiang, Y. Liao, H. Zhang, CdS-Based photocatalysts, *Energy & Environmental Science*, 11 (2018) 1362-1391.
- [32] I.H. M. Bohm, H. Nilsson, O. Noren, Thermal effect of glazing in driver's cabs: evaluation of the impact of different types of glazing on the thermal comfort, 2002.

- [33] F.X. Xiao, J. Miao, H.B. Tao, S.F. Hung, H.Y. Wang, H.B. Yang, J. Chen, R. Chen, B. Liu, One-dimensional hybrid nanostructures for heterogeneous photocatalysis and photoelectrocatalysis, *Small*, 11 (2015) 2115-2131.
- [34] Y. Liu, J. Han, W. Qiu, W. Gao, Hydrogen peroxide generation and photocatalytic degradation of estrone by microstructural controlled ZnO nanorod arrays, *Applied Surface Science*, 263 (2012) 389-396.
- [35] J.P. Song, P.F. Yin, J. Mao, S.Z. Qiao, X.W. Du, Catalytically active and chemically inert CdIn<sub>2</sub>S<sub>4</sub> coating on a CdS photoanode for efficient and stable water splitting, *Nanoscale*, 9 (2017) 6296-6301.
- [36] X. Zhao, M. Lu, M.J. Koeper, R. Agrawal, Solution-processed sulfur depleted Cu(In, Ga)Se<sub>2</sub> solar cells synthesized from a monoamine–dithiol solvent mixture, *Journal of Materials Chemistry A*, 4 (2016) 7390-7397.
- [37] A.R. Uhl, J.K. Katahara, H.W. Hillhouse, Molecular-ink route to 13.0% efficient low-bandgap CuIn(S,Se)<sub>2</sub> and 14.7% efficient Cu(In,Ga)(S,Se)<sub>2</sub> solar cells, *Energy & Environmental Science*, 9 (2016) 130-134.
- [38] S.S. Fouad, I.M. El Radaf, P. Sharma, M.S. El-Bana, Multifunctional CZTS thin films: Structural, optoelectrical, electrical and photovoltaic properties, *Journal of Alloys and Compounds*, 757 (2018) 124-133.
- [39] S. Zhou, K. Sun, J. Huang, X. Lu, B. Xie, D. Zhang, J.N. Hart, C.Y. Toe, X. Hao, R. Amal, Accelerating Electron-Transfer and Tuning Product Selectivity Through Surficial Vacancy Engineering on CZTS/CdS for Photoelectrochemical CO<sub>2</sub> Reduction, *Small*, 17 (2021) e2100496.
- [40] J. Ge, Y. Yu, Y. Yan, Earth-abundant trigonal BaCu<sub>2</sub>Sn(S<sub>1-x</sub>Se<sub>x</sub>)<sub>4</sub> (x = 0–0.55) thin films with tunable band gaps for solar water splitting, *J. Mater. Chem. A*, 4 (2016) 18885-18891.
- [41] W. Septina, Gunawan, S. Ikeda, T. Harada, M. Higashi, R. Abe, M. Matsumura, Photosplitting of Water from Wide-Gap Cu(In,Ga)S<sub>2</sub> Thin Films Modified with a CdS Layer and Pt Nanoparticles for a High-Onset-Potential Photocathode, *The Journal of Physical Chemistry C*, 119 (2015) 8576-8583.
- [42] B.D. Chernomordik, A.E. Béland, D.D. Deng, L.F. Francis, E.S. Aydil, Microstructure Evolution and Crystal Growth in Cu<sub>2</sub>ZnSnS<sub>4</sub> Thin Films Formed By Annealing Colloidal Nanocrystal Coatings, *Chemistry of Materials*, 26 (2014) 3191-3201.
- [43] H.L. Tan, R. Amal, Y.H. Ng, Exploring the Different Roles of Particle Size in Photoelectrochemical and Photocatalytic Water Oxidation on BiVO<sub>4</sub>, *ACS Appl Mater Interfaces*, 8 (2016) 28607-28614.
- [44] Z. Zhang, J.T. Yates, Jr., Band bending in semiconductors: chemical and physical consequences at surfaces and interfaces, *Chem Rev*, 112 (2012) 5520-5551.
- [45] Q. Qin, Q. Cai, C. Jian, W. Liu, Crystal size-controlled growth of bismuth vanadate for highly efficient solar water oxidation, *Sustainable Energy & Fuels*, 5 (2021) 1129-1133.
- [46] H. Zhou, Y. Qu, T. Zeid, X. Duan, Towards highly efficient photocatalysts using semiconductor nanoarchitectures, *Energy & Environmental Science*, 5 (2012).
- [47] R. Marschall, Semiconductor Composites: Strategies for Enhancing Charge Carrier Separation to Improve Photocatalytic Activity, *Advanced Functional Materials*, 24 (2014) 2421-2440.

- [48] S.J.A. Moniz, S.A. Shevlin, D.J. Martin, Z.-X. Guo, J. Tang, Visible-light driven heterojunction photocatalysts for water splitting – a critical review, *Energy & Environmental Science*, 8 (2015) 731-759.
- [49] H. Wang, L. Zhang, Z. Chen, J. Hu, S. Li, Z. Wang, J. Liu, X. Wang, Semiconductor heterojunction photocatalysts: design, construction, and photocatalytic performances, *Chem Soc Rev*, 43 (2014) 5234-5244.
- [50] J.K. Hyun, S. Zhang, L.J. Lauhon, Nanowire Heterostructures, *Annual Review of Materials Research*, 43 (2013) 451-479.
- [51] W. Shi, N. Chopra, Nanoscale heterostructures for photoelectrochemical water splitting and photodegradation of pollutants, *Nanomaterials and Energy*, 2 (2013) 158-178.
- [52] J. Low, J. Yu, M. Jaroniec, S. Wageh, A.A. Al-Ghamdi, Heterojunction Photocatalysts, *Adv Mater*, 29 (2017).
- [53] Y. Yuan, R.-t. Guo, L.-f. Hong, X.-y. Ji, Z.-d. Lin, Z.-s. Li, W.-g. Pan, A review of metal oxide-based Z-scheme heterojunction photocatalysts: actualities and developments, *Materials Today Energy*, 21 (2021).
- [54] P. Zhou, J. Yu, M. Jaroniec, All-solid-state Z-scheme photocatalytic systems, *Adv Mater*, 26 (2014) 4920-4935.
- [55] K. Maeda, Z-Scheme Water Splitting Using Two Different Semiconductor Photocatalysts, *ACS Catalysis*, 3 (2013) 1486-1503.
- [56] A. Iwase, Y.H. Ng, Y. Ishiguro, A. Kudo, R. Amal, Reduced graphene oxide as a solid-state electron mediator in Z-scheme photocatalytic water splitting under visible light, *J Am Chem Soc*, 133 (2011) 11054-11057.
- [57] Y. Sun, Q. Zhu, B. Bai, Y. Li, C. He, Novel all-solid-state Z-scheme SnO<sub>2</sub>/Pt/In<sub>2</sub>O<sub>3</sub> photocatalyst with boosted photocatalytic performance on water splitting and 2,4-dichlorophenol degradation under visible light, *Chemical Engineering Journal*, 390 (2020).
- [58] X. Yu, H. Qiu, B. Wang, Q. Meng, S. Sun, Y. Tang, K. Zhao, A ternary photocatalyst of all-solid-state Z-scheme TiO<sub>2</sub>-Au-BiOBr for efficiently degrading various dyes, *Journal of Alloys and Compounds*, 839 (2020).
- [59] W.-K. Jo, N.C.S. Selvam, Z-scheme CdS/g-C<sub>3</sub>N<sub>4</sub> composites with RGO as an electron mediator for efficient photocatalytic H<sub>2</sub> production and pollutant degradation, *Chemical Engineering Journal*, 317 (2017) 913-924.
- [60] J. Fu, Q. Xu, J. Low, C. Jiang, J. Yu, Ultrathin 2D/2D WO<sub>3</sub>/g-C<sub>3</sub>N<sub>4</sub> step-scheme H<sub>2</sub>-production photocatalyst, *Applied Catalysis B: Environmental*, 243 (2019) 556-565.
- [61] J. Yu, S. Wang, J. Low, W. Xiao, Enhanced photocatalytic performance of direct Z-scheme g-C<sub>3</sub>N<sub>4</sub>-TiO<sub>2</sub> photocatalysts for the decomposition of formaldehyde in air, *Phys Chem Chem Phys*, 15 (2013) 16883-16890.
- [62] S. Kumar, N. Yadav, P. Kumar, A.K. Ganguli, Design and Comparative Studies of Z-Scheme and Type II Based Heterostructures of NaNbO<sub>3</sub>/CuInS<sub>2</sub>/In<sub>2</sub>S<sub>3</sub> for Efficient Photoelectrochemical Applications, *Inorg Chem*, 57 (2018) 15112-15122.
- [63] Y. Wu, S. Yao, G. Lv, Y. Wang, H. Zhang, P. Liao, Y. Wang, Construction of p-n junctions in single-unit-cell ZnIn<sub>2</sub>S<sub>4</sub> nanosheet arrays toward promoted photoelectrochemical performance, *Journal of Catalysis*, 401 (2021) 262-270.

- [64] R. Liu, Z. Zheng, J. Spurgeon, X. Yang, Enhanced photoelectrochemical water-splitting performance of semiconductors by surface passivation layers, *Energy Environ. Sci.*, 7 (2014) 2504-2517.
- [65] R. Wang, L. Wang, Y. Zhou, Z. Zou, Al-ZnO/CdS Photoanode Modified with a Triple Functions Conformal TiO<sub>2</sub> Film for Enhanced Photoelectrochemical Efficiency and Stability, *Applied Catalysis B: Environmental*, 255 (2019).
- [66] H. Lu, J. Tournet, K. Dastafkan, Y. Liu, Y.H. Ng, S.K. Karuturi, C. Zhao, Z. Yin, Noble-Metal-Free Multicomponent Nanointegration for Sustainable Energy Conversion, *Chem Rev*, 121 (2021) 10271-10366.
- [67] H. Kumagai, T. Minegishi, N. Sato, T. Yamada, J. Kubota, K. Domen, Efficient solar hydrogen production from neutral electrolytes using surface-modified Cu(In,Ga)Se<sub>2</sub> photocathodes, *Journal of Materials Chemistry A*, 3 (2015) 8300-8307.
- [68] M. Chen, Y. Liu, C. Li, A. Li, X. Chang, W. Liu, Y. Sun, T. Wang, J. Gong, Spatial control of cocatalysts and elimination of interfacial defects towards efficient and robust CIGS photocathodes for solar water splitting, *Energy & Environmental Science*, 11 (2018) 2025-2034.
- [69] N. Xiao, S. Li, X. Li, L. Ge, Y. Gao, N. Li, The roles and mechanism of cocatalysts in photocatalytic water splitting to produce hydrogen, *Chinese Journal of Catalysis*, 41 (2020) 642-671.
- [70] J. Ran, M. Jaroniec, S.Z. Qiao, Cocatalysts in Semiconductor-based Photocatalytic CO<sub>2</sub> Reduction: Achievements, Challenges, and Opportunities, *Adv Mater*, 30 (2018).
- [71] Q. He, H. Sun, Y. Shang, Y. Tang, P. She, S. Zeng, K. Xu, G. Lu, S. Liang, S. Yin, Z. Liu, Au@TiO<sub>2</sub> yolk-shell nanostructures for enhanced performance in both photoelectric and photocatalytic solar conversion, *Applied Surface Science*, 441 (2018) 458-465.
- [72] X. Li, W. Bi, L. Zhang, S. Tao, W. Chu, Q. Zhang, Y. Luo, C. Wu, Y. Xie, Single-Atom Pt as Co-Catalyst for Enhanced Photocatalytic H<sub>2</sub> Evolution, *Adv Mater*, 28 (2016) 2427-2431.
- [73] W. Chen, Y. Wang, S. Liu, L. Gao, L. Mao, Z. Fan, W. Shangguan, Z. Jiang, Non-noble metal Cu as a cocatalyst on TiO<sub>2</sub> nanorod for highly efficient photocatalytic hydrogen production, *Applied Surface Science*, 445 (2018) 527-534.
- [74] N. Zhao, L. Kong, Y. Dong, G. Wang, X. Wu, P. Jiang, Insight into the Crucial Factors for Photochemical Deposition of Cobalt Cocatalysts on g-C<sub>3</sub>N<sub>4</sub> Photocatalysts, *ACS Appl Mater Interfaces*, 10 (2018) 9522-9531.
- [75] C. Han, L. Wu, L. Ge, Y. Li, Z. Zhao, AuPd bimetallic nanoparticles decorated graphitic carbon nitride for highly efficient reduction of water to H<sub>2</sub> under visible light irradiation, *Carbon*, 92 (2015) 31-40.
- [76] P. Zhang, T. Song, T. Wang, H. Zeng, Fabrication of a non-semiconductor photocatalytic system using dendrite-like plasmonic CuNi bimetal combined with a reduced graphene oxide nanosheet for near-infrared photocatalytic H<sub>2</sub> evolution, *Journal of Materials Chemistry A*, 5 (2017) 22772-22781.
- [77] M. Wu, J.-M. Yan, X.-W. Zhang, M. Zhao, Q. Jiang, Ag<sub>2</sub>O modified g-C<sub>3</sub>N<sub>4</sub> for highly efficient photocatalytic hydrogen generation under visible light irradiation, *Journal of Materials Chemistry A*, 3 (2015) 15710-15714.

- [78] H. Xu, S. Li, L. Ge, C. Han, Y. Gao, D. Dai, In-situ synthesis of novel plate-like Co(OH)<sub>2</sub> co-catalyst decorated TiO<sub>2</sub> nanosheets with efficient photocatalytic H<sub>2</sub> evolution activity, *International Journal of Hydrogen Energy*, 42 (2017) 22877-22886.
- [79] Z. Sun, M. Zhu, M. Fujitsuka, A. Wang, C. Shi, T. Majima, Phase Effect of Ni<sub>3</sub>P<sub>2</sub> Hybridized with g-C<sub>3</sub>N<sub>4</sub> for Photocatalytic Hydrogen Generation, *ACS Appl Mater Interfaces*, 9 (2017) 30583-30590.
- [80] Y. Liu, X. Xu, J. Zhang, H. Zhang, W. Tian, X. Li, M.O. Tade, H. Sun, S. Wang, Flower-like MoS<sub>2</sub> on graphitic carbon nitride for enhanced photocatalytic and electrochemical hydrogen evolutions, *Applied Catalysis B: Environmental*, 239 (2018) 334-344.
- [81] L. Song, X. Kang, S. Zhang, CNT/g-C<sub>3</sub>N<sub>4</sub> photocatalysts with enhanced hydrogen evolution ability for water splitting based on a noncovalent interaction, *International Journal of Energy Research*, 42 (2018) 1649-1656.
- [82] Y. Sui, L. Wu, S. Zhong, Q. Liu, Carbon quantum dots/TiO<sub>2</sub> nanosheets with dominant (001) facets for enhanced photocatalytic hydrogen evolution, *Applied Surface Science*, 480 (2019) 810-816.
- [83] K.K. Sakimoto, S.J. Zhang, P. Yang, Cysteine-Cystine Photoregeneration for Oxygenic Photosynthesis of Acetic Acid from CO<sub>2</sub> by a Tandem Inorganic-Biological Hybrid System, *Nano Lett*, 16 (2016) 5883-5887.
- [84] R. Zhang, X. Wen, H. Peng, Y. Xia, F. Xu, L. Sun, Facet-dependent CO<sub>2</sub> reduction reactions on kesterite Cu<sub>2</sub>ZnSnS<sub>4</sub> photo-electro-integrated electrodes, *Phys Chem Chem Phys*, 24 (2021) 48-55.

## PART 2

**Visible light-driven  $\text{H}_2\text{O}_2$  synthesis by a  $\text{Cu}_3\text{BiS}_3$  photocathode via a photoelectrochemical indirect two-electron oxygen reduction reaction**



## 1. Introduction

Hydrogen peroxide ( $H_2O_2$ ) has received increasing attention as a product of artificial photosynthesis, a promising strategy for solar energy conversion [1-3]. Additionally,  $H_2O_2$  has the advantage of high energy density and can be stored as an aqueous solution at normal temperature and pressure [4]. The development of  $H_2O_2$  fuel cells (theoretical  $V_{oc} = 1.1$  V, comparable to 1.23 V of  $H_2$  fuel cells) has made  $H_2O_2$  become a new ideal solar fuel [5, 6]. Generally, there are two photocatalytic  $H_2O_2$  production pathways, i.e., particulate photocatalytic (PC) and photoelectrochemical (PEC) systems. The PC system has the advantages of convenience and high profitability [7-10]. However, the oxidation reaction and reduction reaction on the surface of the catalyst proceed simultaneously, and thus excellent activity and selectivity for both oxygen reduction reaction (ORR) and water oxidation reaction (WOR) are needed [10]. Tada et.al reported a carbonate-modified surface Au nanoparticle-loaded rutile  $TiO_2$  for ORR to generate  $H_2O_2$ . Unfortunately,  $HCOOH$  as a sacrificing electron donor was needed [11]. For the systems of photoelectrochemical cells, oxidation and reduction reactions occur on the photoanode and photocathode, respectively, i.e., the selectivity and activity for ORR and WOR can be separately improved. Studies on WOR generating  $H_2O_2$  have mainly focused on the development of photoanode metal oxide materials [12]. Fuku et al. reported that a  $WO_3/BiVO_4$  photoanode coated with a mesoporous  $Al_2O_3$  layer could lead to excellent oxidative  $H_2O_2$  generation at a selectivity of ca. 80% [13]. Yin et al. developed a  $BiVO_4$  photoanode with surface oxygen vacancies that showed a photocurrent density of  $4.32\text{ mA}\cdot\text{cm}^{-2}$  at 1.23 V vs. RHE [14]. However,  $H_2O_2$  production via WOR by PEC systems is restricted by the high redox potential for  $H_2O_2$  production via WOR (1.74 V vs. RHE; eq.1). Prevention of the decomposition of  $H_2O_2$  at such high oxidation potential is difficult since  $H_2O_2$  usually serves as an excellent hole scavenger and an intermediate reductant. In this case, accumulation of  $H_2O_2$  is difficult in a PEC system that mainly relies on  $2e^-$  WOR.

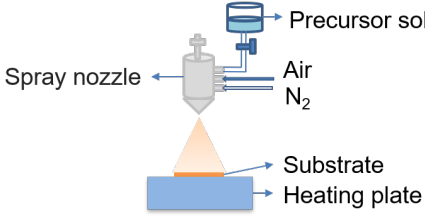
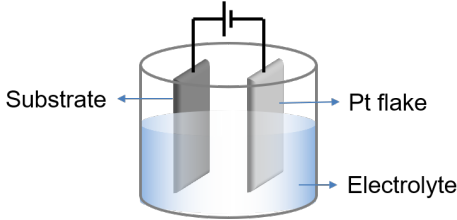


The use of a PEC system for boosting  $2e^-$  ORR (0.68 V vs. RHE; eq. 2) is a promising strategy for  $H_2O_2$  production. Up to now, only a few kinds of semiconductors have shown activity for PEC  $2e^-$  ORR, most of which were organic materials that showed activity via a photosensitizer effect with dyes [15, 16]. However, these photo-responsive dyes were often toxic. For example, the accumulation of porphyrin in the human body can lead to porphyria [17]. In addition, most of the processes for preparation of organic photosensitizers were complicated, thus increasing their preparation costs. Alternatively, inorganic materials have the advantage of high carrier mobility. Besides, their preparation steps are relatively simple, which reduces the manufacturing cost. However, the only successful inorganic *p*-type semiconductor system for photocatalytic  $H_2O_2$  production was Gd-doped  $CuBi_2O_4/CuO$ . Unfortunately, this system required an electrolyte of 0.1 M KOH since the  $CuO$  coating could be easily decomposed under acidic and neutral conditions [18]. In this case, such strong alkaline conditions restricted the accumulation of  $H_2O_2$  and limited the maximum concentration of  $H_2O_2$ . Furthermore, the  $O2p$  orbitals of metal oxides usually result in a deep valence band, thus leading to a large bandgap (2.2 - 3.5 eV) and an undesired light usage [19].

Copper-based sulfides, such as  $CuInS_2$  [20-22], and  $Cu_2ZnSnS_4$  [23, 24], have attracted increasing attention for solar to chemical conversion efficiency due to their suitable bandgaps and high absorption coefficients ( $>10^5 \text{ cm}^{-1}$ ) [25]. Their  $S2p$  orbitals could enhance light absorption (bandgap of 1.1 - 2 eV) compared with metal oxide semiconductors with  $O2p$  orbitals [26]. Additionally, copper-based sulfides were not easily dissolved under acidic or neutral conditions. In this case, sulfides are promising inorganic materials for preparation of photocathodes for  $H_2O_2$  production via  $2e^-$  ORR [27, 28]. Li et.al reported a particle-on-flower nanostructure  $Au-Cu_3BiS_3$  for PEC HER [29]. They coated  $Au-Cu_3BiS_3$  nanoparticles with a flower-like structure on ITO glass to prepare thin-film electrodes to obtain a larger specific surface area and more active sites. Spray pyrolysis deposition (SPD) and electrophoresis deposition (EPD) are both excellent methods for preparing thin films (details can be seen in **Table 2-1**). Previously, we prepared  $Cu_3BiS_3$  (CBS) thin-film electrodes by using EPD for PEC  $H_2$  evolution [30]. However, particles of different sizes resulted in an unsmooth and porous surface of the

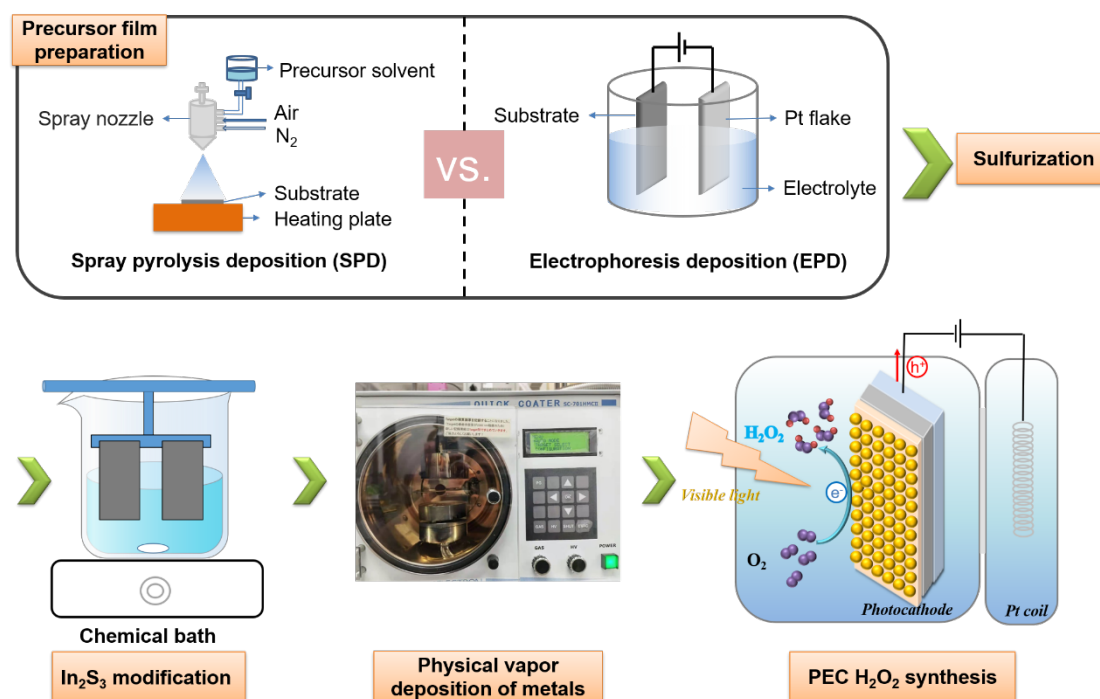
electrode after the electrophoresis process. The unsmooth surface usually resulted in a poor charge transfer between the interface of *p-n* junctions (CBS/In<sub>2</sub>S<sub>3</sub>), thus leading to unsatisfactory photocurrents. Additionally, the Pt surface of the previous system is not suitable for H<sub>2</sub>O<sub>2</sub> production since Pt usually reduces the change of free energy ( $\Delta G$ ) of intermediates during HER  $4e^-$  ORR reaction (usually resulting in a high selectivity for HER and  $4e^-$  ORR) [31]. A promising PEC system would enable efficient charge transfer for high activity and have a desirable surface for good selectivity. Thus, seeking a practical strategy for CBS to achieve PEC H<sub>2</sub>O<sub>2</sub> production is still of great importance.

**Table 2-1.** Comparison of spray pyrolysis deposition (SPD) and electrophoresis deposition

Prepare methods	Advantages	Disadvantages
 <p><b>Spray pyrolysis deposition</b></p>	<ul style="list-style-type: none"> <li>• High efficiency</li> <li>• Low cost</li> <li>• Possibility to large product volumes and sizes</li> <li>• Precisely controlled stoichiometric ratios</li> <li>• Controllability of material properties</li> </ul>	<ul style="list-style-type: none"> <li>• Low tap density</li> </ul>
 <p><b>Electrophoretic deposition</b></p>	<ul style="list-style-type: none"> <li>• High efficiency</li> <li>• Low cost</li> <li>• Possibility to large product volumes and sizes</li> <li>• Deposition in nanometer thickness</li> </ul>	<ul style="list-style-type: none"> <li>• Low crystallinity</li> <li>• Possibility of shedding</li> </ul>

In this study, an efficient cathode of In<sub>2</sub>S<sub>3</sub>/CBS was fabricated by the combination of simple spray pyrolysis deposition (SPD) on a molybdenum-coated glass (Mo-SLG) and chemical bath deposition (**Scheme 1**). The electrode photocurrent during H<sub>2</sub>O<sub>2</sub> production increased 131 times than that without In<sub>2</sub>S<sub>3</sub> modification, which is 3 times higher than that in our previous work in the same bias conditions (0.35 V vs. NHE). After the deposition of Au as a co-catalyst, H<sub>2</sub>O<sub>2</sub> was obtained through an indirect  $2e^-$  ORR at a rate of 5.5 mg·L<sup>-1</sup>·h<sup>-1</sup>·cm<sup>-1</sup> with a Faraday efficiency of 71%. To the best of our knowledge, it is the first report of a sulfide-based photocathode for photoelectrochemical synthesis of H<sub>2</sub>O<sub>2</sub>.

Furthermore, this work provides a practical strategy for designing a highly efficient CBS photocathode and is easily accessible for other inorganic photocathodes.\_



**Scheme 1.** Flow chart of Au-In<sub>2</sub>S<sub>3</sub>/Cu<sub>3</sub>BiS<sub>3</sub> photocathode preparation.

## 2. Experimental section

### 2.1 Chemicals

Unless otherwise stated, all of the chemicals used in the study were of analytical grade and used without further purification. All solutions were prepared by using ultra-pure water. Bi(NO<sub>3</sub>)<sub>3</sub>·5H<sub>2</sub>O, Cu(NO<sub>3</sub>)<sub>2</sub>·3H<sub>2</sub>O, S powder, InCl<sub>3</sub>·4H<sub>2</sub>O and nitric acid of analytical grade were purchased from Wako Pure Chemical Industries, Ltd., Japan. C<sub>2</sub>H<sub>5</sub>NS of analytical grade was purchased from Tokyo Chemical Industry, Japan. Mo/SLG substrate was purchased from GEOMATEC Co. Ltd., Japan.

### 2.2 Fabrication of a Cu<sub>3</sub>BiS<sub>3</sub> photocathode

In this study, typically, 0.9 M Cu(NO<sub>3</sub>)<sub>2</sub>·3H<sub>2</sub>O (99.9%) and 0.3 M Bi(NO<sub>3</sub>)<sub>3</sub>·5H<sub>2</sub>O (99.9%) were fully dissolved in 10% aqueous HNO<sub>3</sub> solution with stirring for 8 h and then the two solutions were mixed at a volume ratio of 1:1 to obtain the precursor solvent. The temperature of the reaction stage was controlled at 380 °C, and 5 mL of the precursor

solvent was sprayed onto an Mo/SLG substrate (16 mm × 20 mm). The spraying time was controlled at 7 min. The precursor film was put into a glass tube together with 0.5 g of sulfur (99.9%), evacuated to 102 Pa, and then heated at 550 °C for 1 h. The heating rate was controlled at 5 °C/min. After cleaning with ammonia aqueous solution (25%) and ammonium sulfide (99.9%), the CBS photocathode was obtained.

## **2.3 Modification with n-type buffer layers**

### **2.3.1 Surface modification with an *n*-type In<sub>2</sub>S<sub>3</sub> layer**

An *n*-type In<sub>2</sub>S<sub>3</sub> layer was formed by the chemical bath deposition method. During the process, 2.5 mmol of InCl<sub>3</sub> (99.9%), 10 mmol of thioacetamide (99.9%) and 0.6 mL of acetic acid (99.9%) were added into 100 mL of ultrapure water and stirred until they were completely dissolved. The electrode was immersed in the aqueous solution, and the bath was heated at 65 °C for 30 minutes. After that, the electrode was taken out, washed with ultrapure water, and then annealed at 100 °C for 20 minutes to obtain In<sub>2</sub>S<sub>3</sub>/CBS.

### **2.3.2 Surface modification with an *n*-type CdS layer**

An *n*-type CdS layer was formed by the chemical bath deposition method. 79.6 mL of ultrapure water, 12.5 mmol of Cd(CH<sub>3</sub>COO)<sub>2</sub>·2H<sub>2</sub>O (99.9 %), 220 mmol of SC(NH<sub>2</sub>)<sub>2</sub> (98 %) and 20.4 mL of NH<sub>3</sub> aqueous solution (25 %) were added to the beaker and the mixture was stirred until they were completely dissolved. The electrode was immersed in the aqueous solution, and the bath was heated at 65 °C for 9 minutes. After that, the electrode was taken out, washed with ultrapure water, and then annealed at 200 °C for 10 minutes to obtain CdS/CBS.

### **2.3.3 Surface modification with an *n*-type ZnS layer**

An *n*-type ZnS layer was formed by the chemical bath deposition method. 74.4 mL of ultrapure water were added 0.16 mol of ZnSO<sub>4</sub>·7H<sub>2</sub>O (99.9%), 0.6 mol of SC(NH<sub>2</sub>)<sub>2</sub> (98%) and 15.6 mL of NH<sub>3</sub> aqueous solution (25%) were added to the beaker and the mixture was stirred until they were completely dissolved. The electrode was immersed in the aqueous solution, and the bath was heated at 80 °C for 15 minutes. After that, the

electrode was taken out, washed with ultrapure water, and then annealed at 100 ° C for 10 minutes to obtain ZnS/ CBS.

## 2.4 Deposition of Au

Au layers were sprayed onto the In<sub>2</sub>S<sub>3</sub>/CBS surfaces to a thickness of 2 nm using a programmable sputter coater (SC-701HMC II, Sanyu Electron Co.) with an Au disc target material (49×t0.5/4N). Pt, Cu, Ag, and Ni layers were prepared by similar spray strategies.

## 2.5 Characterization of catalysts

The crystalline phases were characterized by using a powder X-ray diffraction (XRD) instrument (MiniFlex II, Rigaku Co.) with CuK $\alpha$  ( $\lambda = 1.5418 \text{ \AA}$ ) radiation (cathode voltage: 30 kV, current: 15 mA). The absorption properties of an Au-In<sub>2</sub>S<sub>3</sub>/CBS electrode were measured using the diffuse reflection method with a UV-VIS spectrometer (UV-2600, Shimadzu Co.) attached to an integral sphere at room temperature. X-ray photoelectron spectroscopy (XPS) measurements were performed by using a Kratos AXIS Nova spectrometer (Shimadzu Co.) with a monochromatic Al K $\alpha$  X-ray source. The binding energy was calibrated by taking the C1s peak of contaminant carbon as a reference at 284.6 eV. Raman spectroscopy measurements were performed with 532 nm excitation wavelength (NRS-5100, JASCO Co.).

## 2.6 Photoelectrochemical (PEC) measurement

The PEC performance of the CBS electrode was investigated in a three-electrode configuration by using a silver-silver chloride (Ag/AgCl) reference electrode and a Pt coil counter electrode. In order to avoid the influence of Pt<sup>2+</sup>, an H-type electrolytic cell is used, and the Nafion™ membrane is used for isolation. The electrolytes were 0.1 M Eu<sup>3+</sup>-containing aqueous solution, 0.1 M Na<sub>2</sub>SO<sub>4</sub> solution (pH = 6) or 0.1 M phosphate buffer solution (pH = 7). All electrolytes were stirred and purged with N<sub>2</sub> gas or O<sub>2</sub> gas for 30 min before PEC measurement. In the case of 0.1 M phosphate buffer solution (pH = 7), the measured potential vs. Ag/AgCl was converted to RHE by Nernst's equation ( $E_{RHE} = E_{Ag/AgCl} + 0.059 \text{ pH} + 0.197$ ). Linear sweep voltammetry and chronoamperometry

measurements were carried out by an automatic polarization system (HSV-110, Hokuto Denko Co.) under visible light (420-800 nm) irradiation. The scan rate for the linear sweep voltammetry was  $10 \text{ mV/s}^{-1}$ . For details of the reaction device, please refer to the supporting information **Figure 2-1**.

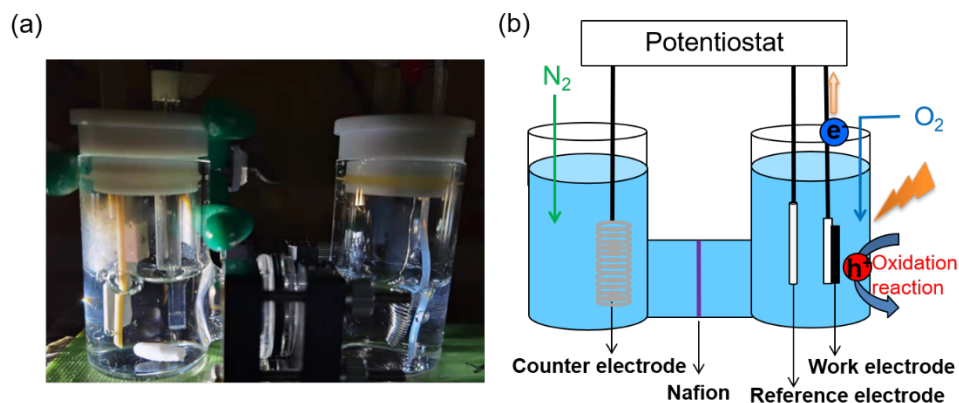


**Figure 2-1.** (a) Photograph of H-type electrolytic cell for oxygen reduction reaction. (b) Schematic diagram of H-type electrolytic cell for oxygen reduction reaction.

In the experiments of trapping superoxide radicals, the non-aqueous electrolyte was acetonitrile with 0.1 M tetra-n-butylammonium hexafluorophosphate (TBAPF<sub>6</sub>) and 0.5 M acetic acid (CH<sub>3</sub>COOH) dissolved. The Ag/Ag<sup>+</sup> electrode was used as a reference electrode and the electrolyte inside was acetonitrile with 0.1 M TBAPF<sub>6</sub> and 0.01 M AgNO<sub>3</sub> dissolved. The Pt coil was used as a counter electrode. A Nafion™ membrane was used to separate anolytes and catholytes.

## 2.7 Analysis of products

The amount of H<sub>2</sub>O<sub>2</sub> was determined by a colorimetric method using PACKTEST (WAK-H<sub>2</sub>O<sub>2</sub>, KYORITSU CHEMICAL- CHECK Lab., Corp.) equipped with a digital PACKTEST spectrometer (ED723, GL Sciences Inc.). H<sub>2</sub> gas was detected by an on-line gas chromatograph (GC) with a thermal conductivity detector (Agilent Technology Co. Micro GC) equipped with an MS-5A column.

### 3. Results and discussion

#### 3.1 Comparison of electrodes prepared by electrophoretic deposition and spray pyrolysis deposition

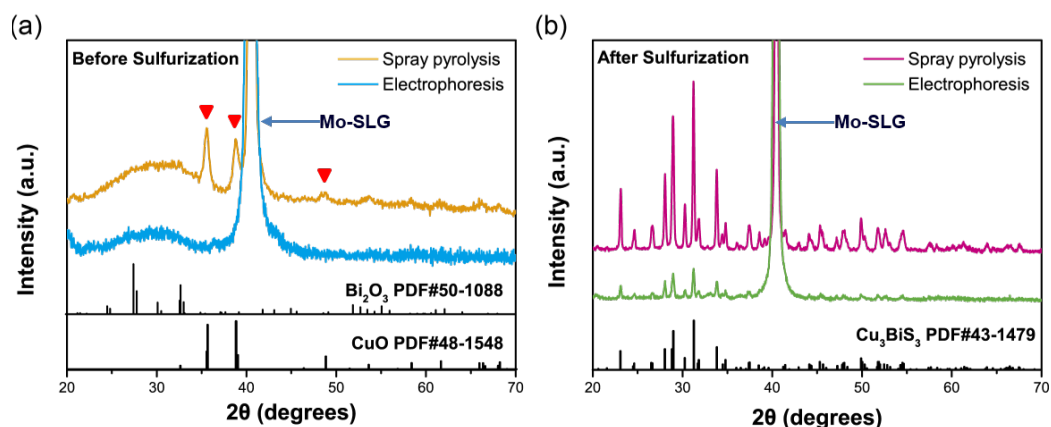


**Figure 2-2.** XRD analysis of  $\text{Cu}_3\text{BiS}_3$  electrodes prepared by SPD and EPD. (a) XRD analysis of photocathode films before sulfurization and (b) after sulfurization.

**Table 2-2.** XRD analysis of several main peaks of  $\text{Cu}_3\text{BiS}_3$ .

2-Theta	hkl	SPD		EPD	
		FWHM (2 $\theta$ )	Peak height (nm)	FWHM (2 $\theta$ )	Peak height (nm)
23.095	200	0.157	560	0.178	60
28.054	211	0.157	535	0.187	76
28.995	031	0.155	570	0.184	113
31.271	131	0.153	780	0.193	138
33.836	122	0.158	321	0.179	77

The  $\text{Cu}_3\text{BiS}_3$  (CBS) electrode was prepared via a two-step method. Firstly, a mixture solution of Bi and Cu was sprayed onto an Mo/SLG substrate. After formation of a mixed thin film of  $\text{Bi}_2\text{O}_3$  and CuO by calcination at the high temperature of 550 °C, the as-prepared metal oxide film was sulfurized in a vacuum-sealed quartz tube. A CBS electrode was also prepared by EPD (EPD was used for preparation of  $\text{Bi}_2\text{O}_3$  and CuO as a sulfurization precursor film.) for comparison. XRD spectra were used to verify the crystallinity of the as-prepared electrodes. As illustrated in XRD patterns (**Figure 2-2a**), it was speculated that the main components of the precursor film prepared by SPD were amorphous  $\text{Bi}_2\text{O}_3$  (JCPDS No. 50-1088) and CuO (JCPDS No. 48-1548). The film prepared by the EPD method showed an amorphous crystalline structure, which is



unfavorable for further sulfurization to obtain a highly crystalline CBS electrode. On the other hand, the film prepared via SPD shown higher crystallinity. Typical diffractions of CuO ( $35.4^\circ$ ,  $38.7^\circ$  and  $48.7^\circ$ ) and Bi<sub>2</sub>O<sub>3</sub> were clearly observed, indicating a precursor film with high crystallinity. After the sulfurization process, the XRD patterns obtained by measuring the films prepared by SPD and EPD (**Figure 2-2b**) perfectly matched with the standard spectrum of CBS (JCPDS No. 43-1479), indicating that a CBS photocathode could be prepared by both methods. It is noteworthy that the full width at half maximum (FWHM, diffractions at  $23.1^\circ$ ,  $28.1^\circ$ ,  $29.0^\circ$ ,  $31.1^\circ$  and  $33.8^\circ$ , details shown in **Table 2-2**) of the CBS electrode prepared by EPD was bigger than those by SPD, thus, a significantly higher crystallinity of the electrode prepared by SPD. Improved crystallinity of a photoelectrode usually results in an improved charge transfer in bulk phase, thus leading to a potentially higher photocurrent and more satisfactory activity.

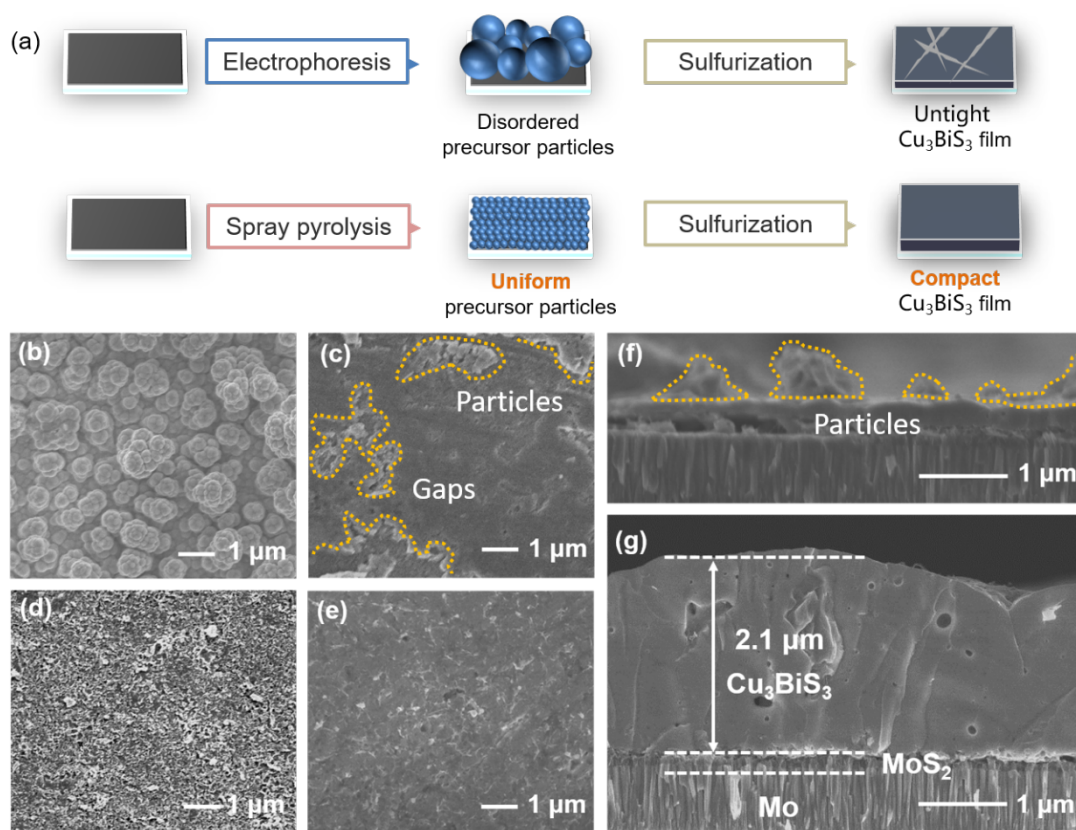


**Figure 2-3. SEM photographs of Cu<sub>3</sub>BiS<sub>3</sub> electrodes prepared by SPD and EPD.** (a) Schematic diagram for preparation for Cu<sub>3</sub>BiS<sub>3</sub> photocathodes via (upper) electrophoresis and (lower) spray pyrolysis. (b) Top-view SEM photographs of photocathode films prepared by EPD before sulfurization and (c) after sulfurization and (d) those of photocathodes films prepared by SPD before sulfurization and (e) after sulfurization. (f) Cross-sectional SEM photograph of photocathode films prepared by EPD and (g)

prepared by SPD after sulfurization.

The morphologies of the as-prepared CBS electrodes were characterized by scanning electron microscopy (SEM). An obvious difference was found in the structures of the CBS electrodes prepared by SPD and EPD. The precursor films prepared by EPD were composited by several large stacked microspheres (**Figure 2-3b**). During the subsequent sulfurization process, these microspheres grew to form protruding particles, and obvious gaps between microspheres (enclosed by yellow dotted lines) were formed as shown in **Figures 2-3c and 2-3f**. This untight film may significantly affect the charge transmission, thus resulting in unsatisfactory photoelectrochemical performance. The precursor film prepared by SPD (**Figure 2-3d**) showed a sponge-like morphology. Although the surface is porous, the tiny particles of  $\text{Bi}_2\text{O}_3$  and  $\text{CuO}$  formed a generally flat surface. During the further sulfurization process, a compact and uniform electrode with a thickness of ca.  $2.1\ \mu\text{m}$  was formed (**Figures 2-3e and 2-3g**). This is beneficial for the charge transfer between the Mo glass and the CBS layer, which may lead to a potentially large photocurrent. Additionally, the smooth surface of the CBS electrode is also beneficial for the charge transfer between the interface of  $\text{Cu}_3\text{BiS}_3$  ( $p$ -type) and  $\text{In}_2\text{S}_3$  ( $n$ -type). A satisfactory charge transfer between the  $p$ - $n$  junctions also results in high photoelectrochemical performance of a photocathode.

UV-vis absorption spectra of CBS electrodes are shown in **Figure 2-4a**. A similar absorption edge is observed in both samples prepared by EPD and SPD, indicating that the phase structure of CBS films has no change. In addition, the CBS electrode samples prepared by EPD had a higher background absorption at longer wavelengths ( $\lambda > 700\ \text{nm}$ ) than that of CBS electrodes samples prepared by SPD, and the band gap was also increased (1.62 eV vs. 1.58 eV) (**Figures 2-4b and 2-5**), indicating a higher density of defects [32].

To further analyze the band structure of as-prepared CBS electrodes, Mott-Schottky analysis was performed. The as-prepared CBS was confirmed to be a  $p$ -type semiconductor due to the negative slope in the Mott-Schottky plot (**Figure 2-4c**) [33]. For  $p$ -type semiconductors,  $E_f$  is usually located near the valence band (VB). That is, the flat

band potential is 0.1-0.3 eV lower than the VB potential [34]. As shown in **Figure 2-4c**,  $E_{VB}$  was confirmed to be 0.44 V (0.64 V vs. RHE). Based on the above results, the  $E_{CB}$  of the CBS electrode prepared by SPD could be considered to be located at -1.13 V vs. RHE. As a comparison, the bandgap of the electrode prepared by EPD was calculated to be 1.62 eV, which has a slight blue-shift compared to that for the electrode prepared by SPD (1.58 eV) (**Figure 2-5**). The difference between the band structures of electrodes prepared by EPD and SPD may be due to the compactness and thickness of the cathodic film [35].

To investigate selectivity of the CBS electrode for ORR, the current-potential response was investigated in an Ar-saturated electrolyte under illumination of a Xe lamp (USHIO UXL-500SX2,  $420 < \lambda < 800$  nm, 100 mW/cm<sup>2</sup>).  $\text{Eu}(\text{NO}_3)_3$  was added to the solution as an electron scavenger (**Figure 2-4d**). The CBS electrode exhibited a cathodic photocurrent in response to irradiation of incident light, confirming that the prepared thin film was a *p*-type semiconductor [36]. The photocurrent increased when the electrode potential was shifted to a negative potential. Accordingly, a cathodic photocurrent could be observed at 0.4 V vs. RHE (pH=6), indicating that photoelectrochemical production occurred at the bias of ca. 0.7 V vs. NHE, and thus a  $2e^-$  ORR could occur on the surface of the electrode.

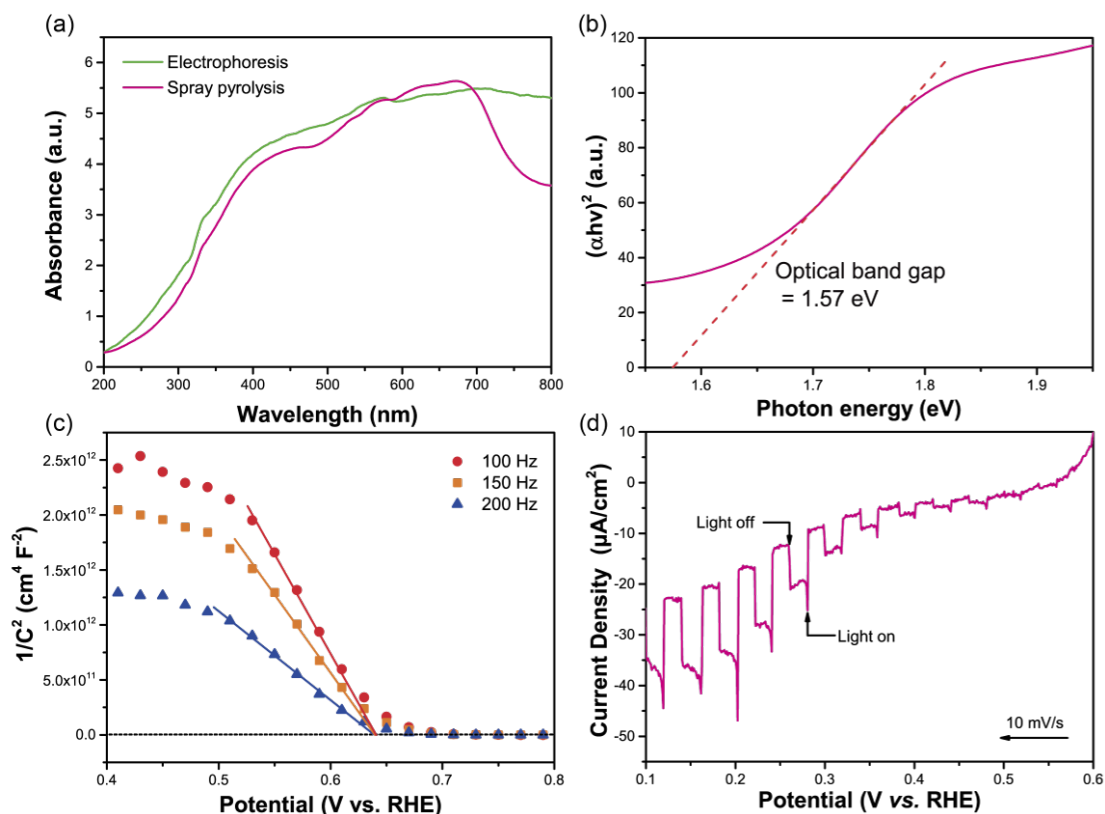


**Figure 2-4. Analysis of the band structures of  $\text{Cu}_3\text{BiS}_3$  electrodes** (a) UV-Vis spectra of  $\text{Cu}_3\text{BiS}_3$  electrodes prepared by SPD and EPD. (b) Tauc plot for the  $\text{Cu}_3\text{BiS}_3$  electrode prepared by SPD. (c) Mott-Schottky plots of the  $\text{Cu}_3\text{BiS}_3$  electrode prepared by SPD. (d) Current-potential curve of the  $\text{Cu}_3\text{BiS}_3$  electrode prepared by SPD in Ar-saturated  $\text{Eu}(\text{NO}_3)_3$  solution (0.1 M, pH = 6) with chopped illumination from visible light (420-800 nm, 100  $\text{mW}/\text{cm}^2$ ).

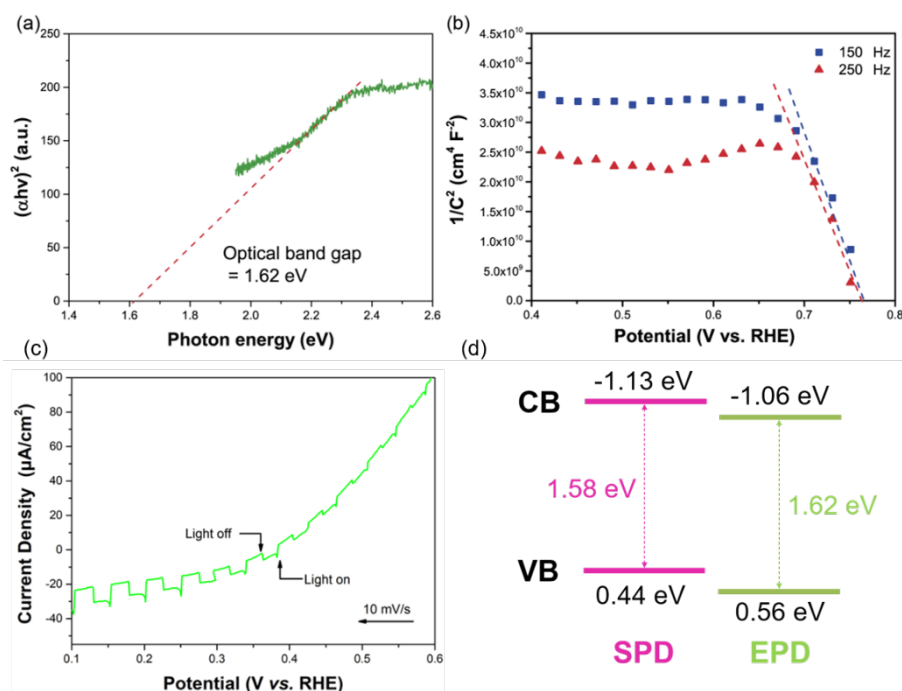


**Figure 2-5.** (a) Tauc plot for the  $\text{Cu}_3\text{BiS}_3$  electrode prepared by electrophoresis deposition. (b) Mott–Schottky plots of  $\text{Cu}_3\text{BiS}_3$  electrode prepared by electrophoresis deposition. (c) Current–potential curve of the  $\text{Cu}_3\text{BiS}_3$  electrode prepared by electrophoresis deposition in Ar-saturated  $\text{Eu}(\text{NO}_3)_3$  solution (0.1 M, pH = 6) with chopped illumination from visible light (420–800 nm, 100  $\text{mW}/\text{cm}^2$ ). (d) Comparison of the bandgaps of  $\text{Cu}_3\text{BiS}_3$  electrodes prepared by SPD and EPD.

SPD was thought to be more advantageous than EPD for the preparation of a CBS electrode [37]. To compare the effects of the two preparation strategies on photoelectrochemical-catalytic activities, we fabricated a typical three-electrode cell by using CBS thin films (prepared by EPD or SPD) as working electrodes. Measurement of Tafel plots was carried out in a 0.1 M  $\text{N}_2$ -saturated  $\text{Na}_2\text{SO}_4$  solution (0.1 M, pH = 6) at 25 °C. The Tafel curve is an intuitive basis for judging the activity of the catalyst. Generally, for HER and ORR, the smaller the Tafel slope means the better activity [38]. As shown in **Figure 2-6a**, the linear regions of the Tafel plots were fitted well to the Tafel equation. Furthermore, the Tafel slope of the electrode prepared by SPD (79  $\text{mV dec}^{-1}$ ) was smaller than that of the electrode prepared by EPD (137  $\text{mV dec}^{-1}$ ). This may be attributable to the greater density of the thin film prepared by SPD, which accelerates carrier transfer. Under the same conditions, the photocurrent of the denser film increased ca. 1.5 times than the untight film prepared by EPD and the dark current was also reduced due to the disappearance of small particles on the surface (**Figure 2-6b**). In addition, we conducted a comparative experiment and found that  $\text{H}_2\text{O}_2$  could not be generated without photoirradiation, indicating that the electrode is undergoing a self-reduction reaction under dark current (**Figure 2-7**). From the perspective of solar-to-chemical energetic conversion, the CBS electrode prepared by SPD was better than that prepared by EPD.

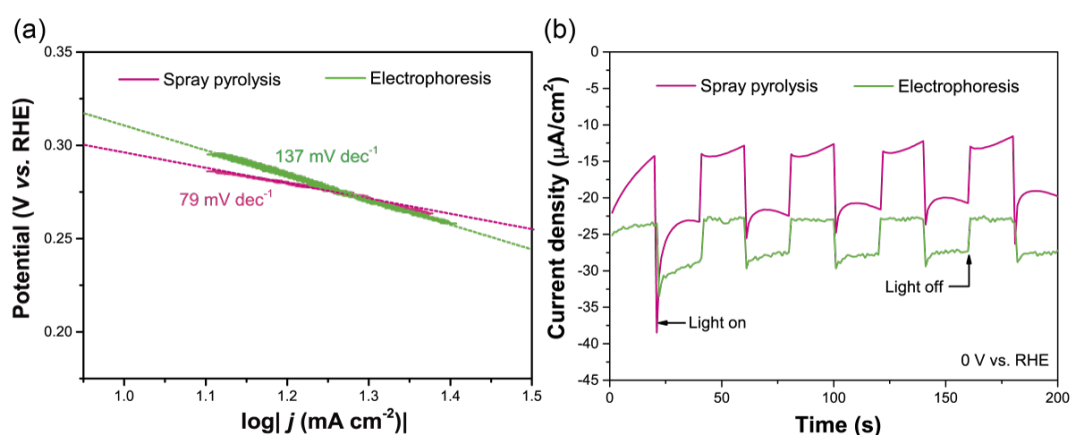


**Figure 2-6. Comparison of the photoactivity of electrodes prepared by electrophoresis and spray pyrolysis deposition.** (a) Tafel plots of CBS films made by the spray pyrolysis deposition (pink) and the electrophoresis deposition (green) with their associated linear fittings (dashed lines) in  $\text{Na}_2\text{SO}_4$  solution (0.1 M, pH = 6). (b) Time courses of the photocurrents of CBS electrodes made by the spray pyrolysis deposition (pink) and the electrophoresis deposition (green) in Ar-saturated  $\text{Eu}(\text{NO}_3)_3$  solution (0.1 M, pH = 6) with visible light (420–800 nm,  $100 \text{ mW}/\text{cm}^2$ ) irradiation under a potentiostatic condition at 0 V vs.  $V_{\text{RHE}}$ .

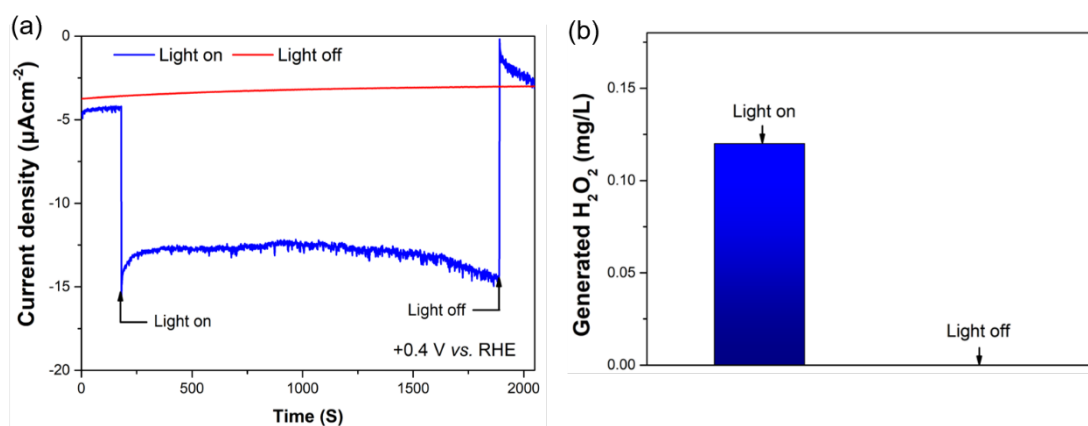


**Figure 2-7.** (a) Time courses of the photocurrent of  $\text{Cu}_3\text{BiS}_3$  electrodes in an  $\text{O}_2$ -bubbling phosphate buffer electrolyte (0.1 M, pH = 7) with a potentiostatic condition at +0.4 V vs.  $V_{\text{RHE}}$  under visible light (420–800 nm,  $100 \text{ mW}/\text{cm}^2$ ) irradiation and dark room. (b) Corresponding generated  $\text{H}_2\text{O}_2$ .

### 3.2 Modification with $\text{In}_2\text{S}_3$ for formation of $p$ - $n$ junctions

In order to improve the responsiveness of the CBS electrode to light, an  $n$ -type semiconductor could be used to modify the electrode for forming  $p$ - $n$  junctions, a well-known strategy for improving the responsiveness to light by increasing the separation efficiency of electrons and holes [39]. In the previous work, the best photo-response could be obtained when  $\text{In}_2\text{S}_3$  was selected for modification [40].

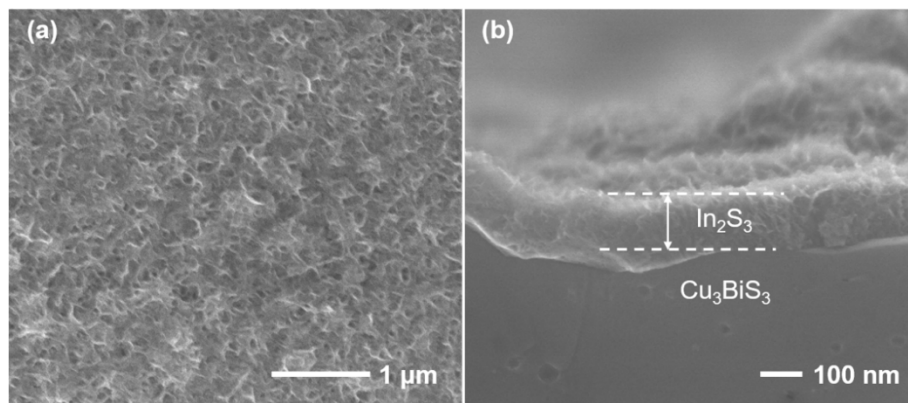


**Figure 2-8.** (a) Top-sectional SEM image of  $\text{In}_2\text{S}_3/\text{Cu}_3\text{BiS}_3$ . (b) Cross-sectional SEM image of  $\text{In}_2\text{S}_3/\text{Cu}_3\text{BiS}_3$ .

As shown in **Figure 2-8** in supplementary material,  $\text{In}_2\text{S}_3$  was uniformly attached to the surface of the CBS electrode, which showed a lamellar flower-like structure. According to the SEM cross-sectional view, the thickness of  $\text{In}_2\text{S}_3$  was ca. 130 nm. Furthermore, the noble metal deposition improved the photoelectric performance and acted as a protective layer for the *p*-type layer electrodes. The distribution of the Au,  $\text{In}_2\text{S}_3$ , CBS and Mo-SLG were clarified by the SEM image and corresponding mapping of the section of the as-prepared electrode (**Figure 2-9 and 2-10**).

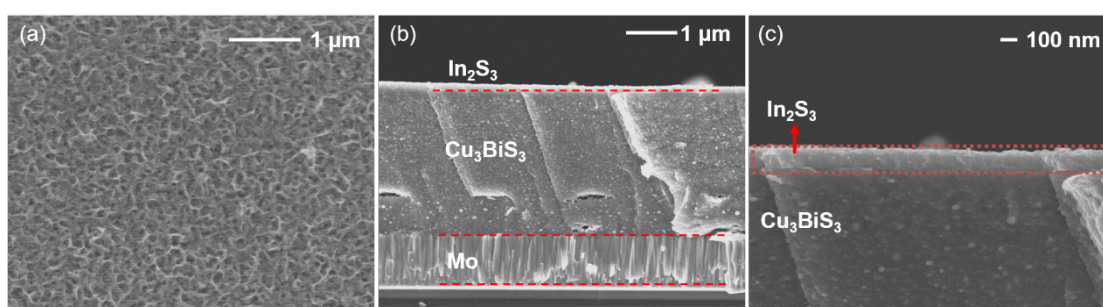


**Figure 2-9.** (a) Top-sectional SEM image of Au- $\text{In}_2\text{S}_3/\text{Cu}_3\text{BiS}_3$ . (b) Cross-sectional SEM image of Au- $\text{In}_2\text{S}_3/\text{Cu}_3\text{BiS}_3$ . (c) Cross-sectional SEM image of Au- $\text{In}_2\text{S}_3/\text{Cu}_3\text{BiS}_3$ .

To make the characterization of the electrode sufficient, we added SEM and EDS mappings of the cross-sectional of Au- $\text{In}_2\text{S}_3/\text{Cu}_3\text{BiS}_3$  electrodes to clarify the distribution of the Au,  $\text{In}_2\text{S}_3$ , CBS and Mo-SLG; XPS spectra of Au- $\text{In}_2\text{S}_3/\text{Cu}_3\text{BiS}_3$  electrodes to prove the valence state of elements in the electrode; Electrochemical impedance spectroscopy (EIS) to compare the ability of charge transfer before and after modification.



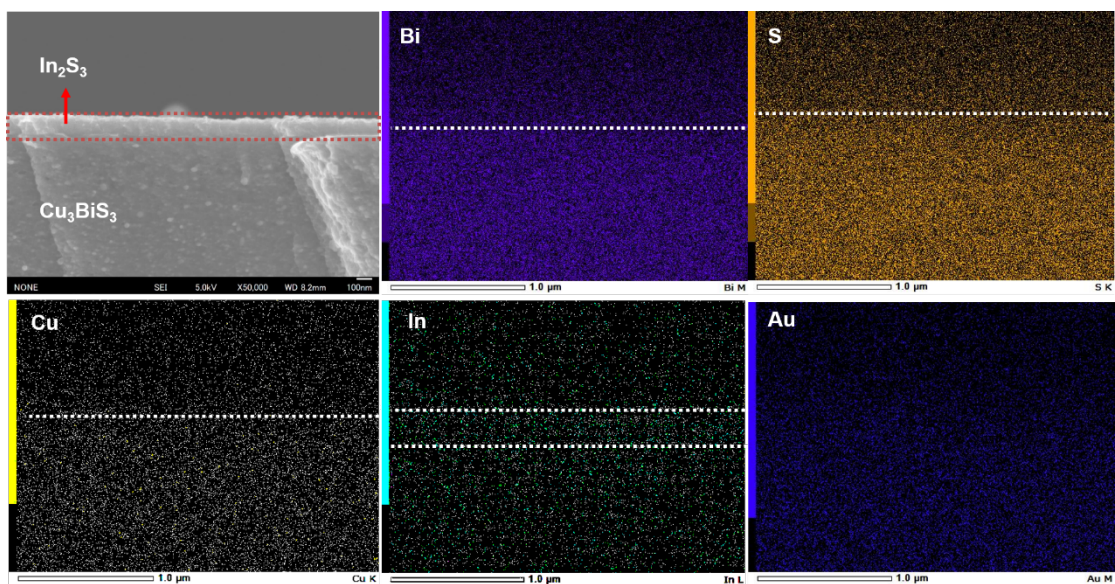


**Figure 2-10.** Energy dispersive spectroscopy on the scanning electron microscope (EDS-SEM). EDS map showing detection of Bi (violet), S (orange), Cu (yellow), In (cyan) and Au (blue).

The elemental compositions and the chemical states of the elements were further verified by XPS analysis (**Figure 2-11**). As displayed in **Figure 2-11a**, main peaks of 952.2 eV, 932.3 eV were found in Cu 2p spectra. This doublet was assigned to the  $\text{Cu}^+$  in CBS. In Bi 4f spectra (**Figure 2-11b**), main peaks of 161.3 eV, 158.1 eV and 163.4 eV were found and these peaks were attributed to typical values of S 2p,  $\text{Bi}^{3+}$  4f<sub>7/2</sub> and  $\text{Bi}^{3+}$  4f<sub>5/2</sub>, respectively [41]. In **Figure 2-11c**, the 3d core of In splits into 3d<sub>5/2</sub> (445.1 eV) and 3d<sub>3/2</sub> (452.6 eV), which were consistent with the values for  $\text{In}^{3+}$  [42]. It can be observed from **Figure 2-11d** that Au 4f signal composed of two peaks at 84.4 eV (Au 4f<sub>7/2</sub>) and 88.1 eV (Au 4f<sub>5/2</sub>), which were consistent with  $\text{Au}^0$  [43].



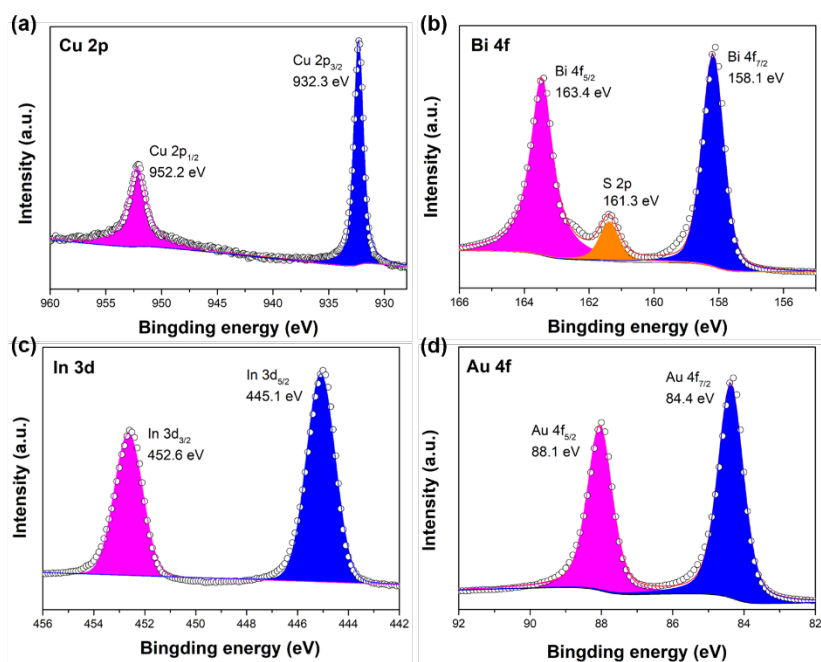


**Figure 2-11.** XPS spectra of Au-In<sub>2</sub>S<sub>3</sub>/Cu<sub>3</sub>BiS<sub>3</sub> electrode. XPS spectra of Cu 2p (a), Bi 4f (b), In 3d (c), and Au 4f (d).

UV-vis spectra showed that the CBS, In<sub>2</sub>S<sub>3</sub>/CBS and Au-In<sub>2</sub>S<sub>3</sub>/CBS electrodes performed the absorption of visible light (**Figure 2-12**).

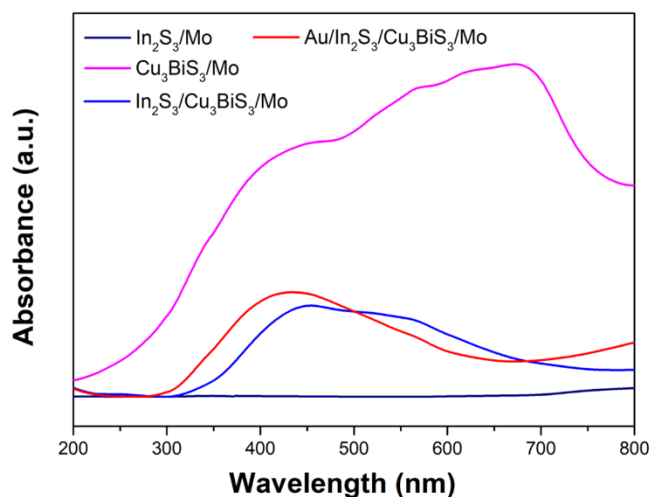


**Figure 2-12.** UV-vis spectra of In<sub>2</sub>S<sub>3</sub>/Mo, Cu<sub>3</sub>BiS<sub>3</sub>/Mo, In<sub>2</sub>S<sub>3</sub>/Cu<sub>3</sub>BiS<sub>3</sub>/Mo and Au-In<sub>2</sub>S<sub>3</sub>/Cu<sub>3</sub>BiS<sub>3</sub>/Mo electrodes.

**Figure 2-13a** shows linear sweep voltammograms (LSV) of Au-CBS, In<sub>2</sub>S<sub>3</sub>/CBS and Au-In<sub>2</sub>S<sub>3</sub>/CBS in O<sub>2</sub>-bubbling phosphate buffer electrolyte (0.1 M, pH = 7) under chopped illumination from visible light (420-800 nm, 100 mW/cm<sup>2</sup>). By blocking the light source once every 2 seconds, the current generated by the light irradiation was illustrated directly.

When an  $\text{In}_2\text{S}_3$  buffer layer was used to modify the CBS electrode, the photocurrent of the  $\text{Au-In}_2\text{S}_3/\text{CBS}$  electrode became the highest at ca.  $-125 \mu\text{Acm}^{-2}$  under the base potential of  $+0.4 \text{ V vs. RHE}$ . Compared with the electrode that was not modified with  $\text{In}_2\text{S}_3$  ( $\text{Au-CBS}$ ) under the same bias potential, the photocurrent of  $\text{Au-In}_2\text{S}_3/\text{CBS}$  electrode prepared by SPD was significantly increased by 131 times. Nevertheless, the photocurrent of the electrode ( $\text{Au-In}_2\text{S}_3/\text{CBS}$ ) prepared by EPD increased only ca. 5 times than that of  $\text{Au-CBS}$  under same condition according to our previous study [30]. This result may be attributed to the smooth CBS electrode surface that made the charge transfer at the interface between the two semiconductors easier, resulting in a larger photocurrent.

Electrochemical impedance spectroscopy (EIS) of the samples were performed in a phosphate buffer electrolyte (0.1 M,  $\text{pH} = 7$ ) with visible light (420–800 nm,  $100 \text{ mW/cm}^2$ ) irradiation. The exchange of charge carriers between the catalyst and the electrolyte at the interface is generally called the charge transfer process. The smaller semicircle in the Nyquist diagram indicates better charge transfer kinetics. With the modification of  $\text{In}_2\text{S}_3$ , the charge transfer resistance of CBS electrode decreased obviously, and this value even further decreased after the modification of Au nanoparticles (**Figure 2-13b**). The results were in line with the conclusion of the previous LSV test. The increase in the charge transfer rate during the PEC process can be manifested as an increase in the photocurrent.

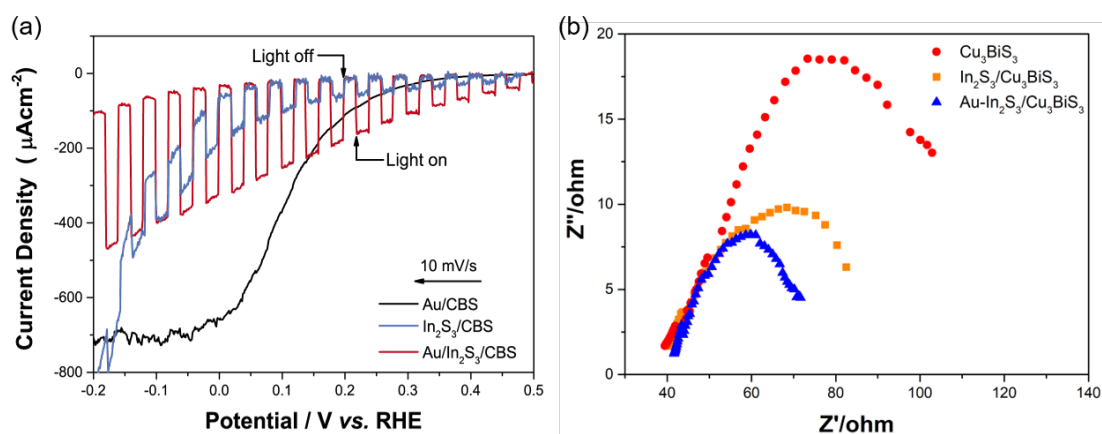


**Figure 2-13. Comparison of  $\text{Cu}_3\text{BiS}_3$  electrodes with and without modification.** (a) Linear sweep voltammograms of  $\text{Au-Cu}_3\text{BiS}_3$ ,  $\text{In}_2\text{S}_3/\text{Cu}_3\text{BiS}_3$  and  $\text{Au-In}_2\text{S}_3/\text{Cu}_3\text{BiS}_3$  electrodes in  $\text{O}_2$ -bubbling phosphate buffer electrolyte (0.1 M,  $\text{pH} = 7$ ) under chopped illumination from visible light (420-800 nm,  $100 \text{ mW/cm}^2$ ) irradiation. (b) Nyquist plots of  $\text{Cu}_3\text{BiS}_3$  (red),  $\text{In}_2\text{S}_3/\text{Cu}_3\text{BiS}_3$  (orange) and  $\text{Au-In}_2\text{S}_3/\text{Cu}_3\text{BiS}_3$  (blue) in a phosphate buffer electrolyte (0.1 M,  $\text{pH} = 7$ ) with visible light (420–800 nm,  $100 \text{ mW/cm}^2$ )

irradiation.

### 3.3 Optimization of the co-catalytic layer for H<sub>2</sub>O<sub>2</sub> production

To investigate the optimized co-catalyst for the as-prepared electrode, several metals were loaded on In<sub>2</sub>S<sub>3</sub>/CBS electrodes. The activities of the as-prepared metal-modified In<sub>2</sub>S<sub>3</sub>/CBS electrodes were compared by measuring the photocurrents. The oxygen reduction reaction was carried out in an O<sub>2</sub>-saturated phosphate buffer electrolyte (0.1 M, pH = 7) with visible light (420–800 nm, 100 mW/cm<sup>2</sup>) irradiation under a potentiostatic condition at +0.4 V vs. V<sub>RHE</sub>. The concentration of H<sub>2</sub>O<sub>2</sub> produced by the Au-loaded electrode within one hour was 1.5 mg/L and a Faraday efficiency of ca. 64% was obtained, indicating an obvious advantage over other metal-loaded and non-loaded electrodes (**Figure 2-15**). It is worth mentioning that the photocathodic compartment was gas-proof, which means the Au-loaded In<sub>2</sub>S<sub>3</sub>/CBS electrode showed selectivity for 2e<sup>-</sup> ORR since H<sub>2</sub> was not detected. The high selectivity may be due to the high activity of Au nanoparticles for ORR. The critical step was the formation of O-Au bonds with a corresponding decrease in the activation energy of molecular oxygen [44].

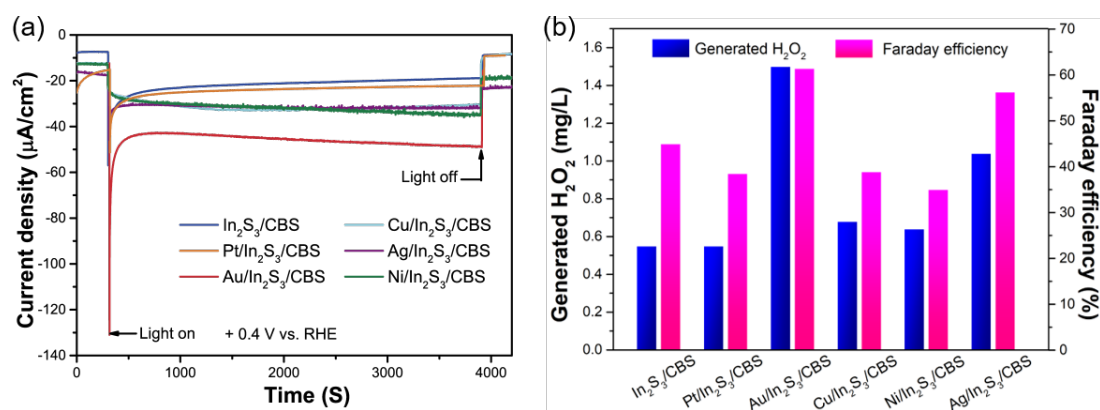


**Figure 2-15. Comparison of the activities of Cu<sub>3</sub>BiS<sub>3</sub> electrodes with different loading metals for generating H<sub>2</sub>O<sub>2</sub>.** (a) Time courses of the photocurrents of metal-loaded In<sub>2</sub>S<sub>3</sub>/Cu<sub>3</sub>BiS<sub>3</sub> electrodes in an O<sub>2</sub>-saturated phosphate buffer electrolyte (0.1 M, pH = 7) with visible light (420–800 nm, 100 mW/cm<sup>2</sup>) irradiation under a potentiostatic condition at +0.4 V vs. V<sub>RHE</sub>. (b) Amounts of generated H<sub>2</sub>O<sub>2</sub> by metal-loaded In<sub>2</sub>S<sub>3</sub>/Cu<sub>3</sub>BiS<sub>3</sub> electrodes with visible light (420–800 nm, 100 mW/cm<sup>2</sup>) irradiation for 1 h and corresponding Faraday efficiencies.

In order to explain this, we need first to understand how the oxygen reduction reaction proceeds in our system. O<sub>2</sub> molecule initially adsorbs on the active sites and

then reduced by electrons to generate superoxide radicals ( $\cdot\text{O}_2^-$ ), which could be easily disproportionated in water to generate  $\text{H}_2\text{O}_2$ . Among them, the adsorption of  $\text{O}_2$  molecules is the first and rate-determining step [45]. Based on DFT calculations (**Figure 2-16**), the free energy required for the formation of Au-O bonds is low, suggesting a fast proton transfer rate [46, 47].

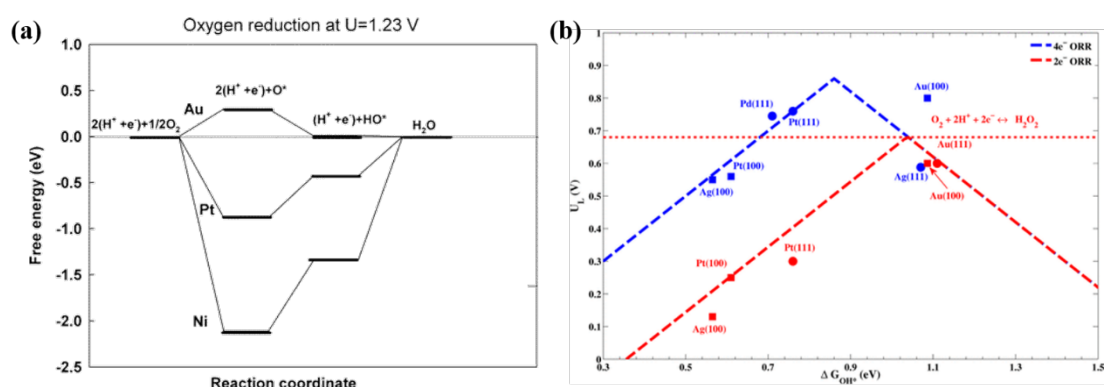


**Figure 2-16.** (1) Free-energy diagram for oxygen reduction at the equilibrium potential  $U_0 = 1.23$  V over Pt, Au, and Ni. (2) Activity volcanoes for the  $2e^-$  and  $4e^-$  reduction of oxygen are shown in red and blue respectively.

The amounts of produced  $\text{H}_2\text{O}_2$  over time and the corresponding changes in Faraday efficiency were investigated to estimate the performance of the electrode (**Figures 2-17**).

As the reaction time increased, the Faradaic efficiency gradually decreased.

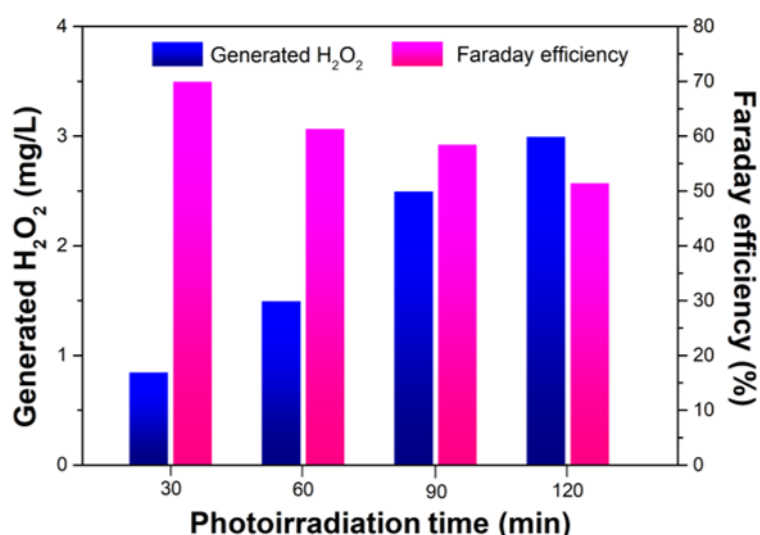


**Figure 2-17.**  $\text{H}_2\text{O}_2$  generated by the  $\text{Au-In}_2\text{S}_3/\text{Cu}_3\text{BiS}_3$  electrode in an  $\text{O}_2$ -saturated phosphate buffer electrolyte (0.1 M, pH = 7) under potentiostatic conditions at  $+0.4$  V<sub>RHE</sub> with visible light (420–800 nm, 100 mW/cm<sup>2</sup>) irradiation and corresponding Faraday efficiency.

**Figures 2-18** showed the corresponding time courses of the photocurrent of Au-In<sub>2</sub>S<sub>3</sub>/Cu<sub>3</sub>BiS<sub>3</sub> electrodes in an O<sub>2</sub>-saturated phosphate buffer electrolyte under a potentiostatic condition at +0.4 V vs. V<sub>RHE</sub>.

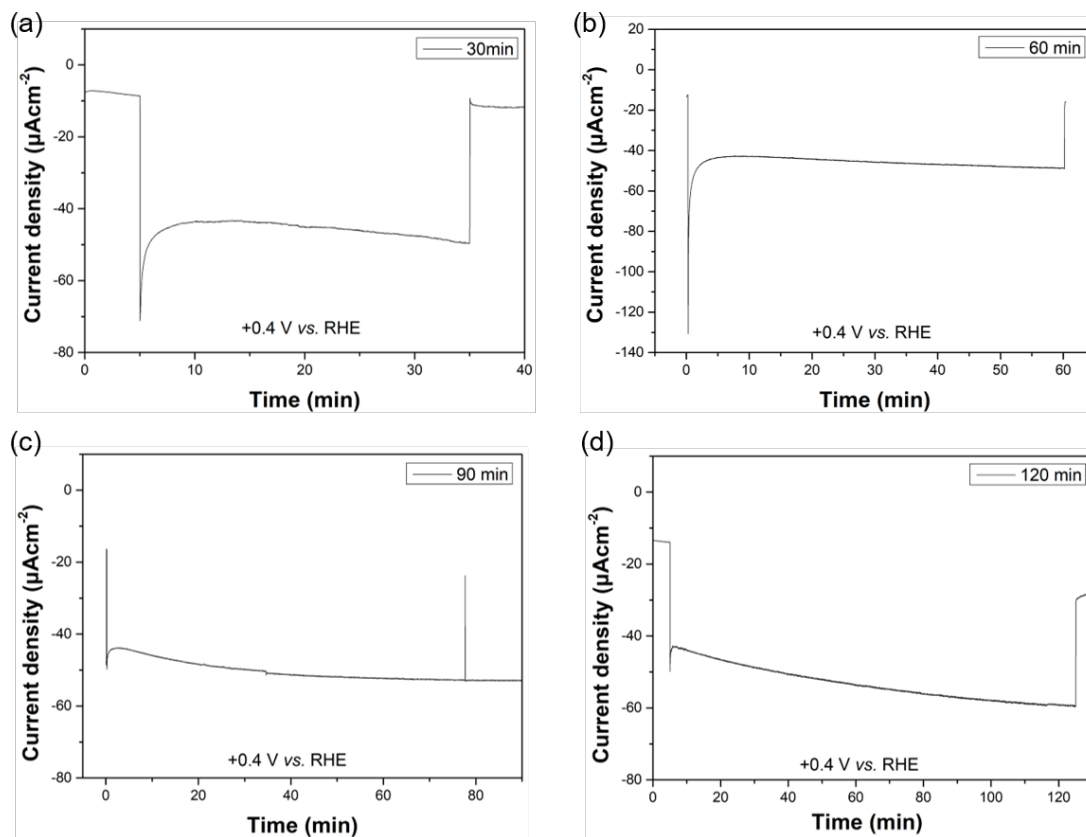


**Figure 2-18.** Time courses of the photocurrent of Au-In<sub>2</sub>S<sub>3</sub>/Cu<sub>3</sub>BiS<sub>3</sub> electrodes in an O<sub>2</sub>-saturated phosphate buffer electrolyte (0.1 M, pH = 7) with visible light (420–800 nm, 100 mW/cm<sup>2</sup>) irradiation under a potentiostatic condition at +0.4 V vs. V<sub>RHE</sub>. (a) Irradiation time was 30 min (b) Irradiation time was 60 min (c) Irradiation time was 90 min (d) Irradiation time was 120 min. (In **Figure 2-18c**, we turned off the light source for 0.1s to check the photo-response of the electrode.)

Under the condition of O<sub>2</sub> bubbling, the amount of generated H<sub>2</sub>O<sub>2</sub> was larger than that under the O<sub>2</sub>-saturated condition (**Figure 2-19a and 2-20**). After visible light irradiation for one hour, the concentration of H<sub>2</sub>O<sub>2</sub> reached 5.5 mg/L, corresponding to a Faraday efficiency of 71%. Moreover, Faraday efficiency remained almost constant with elapse of time.

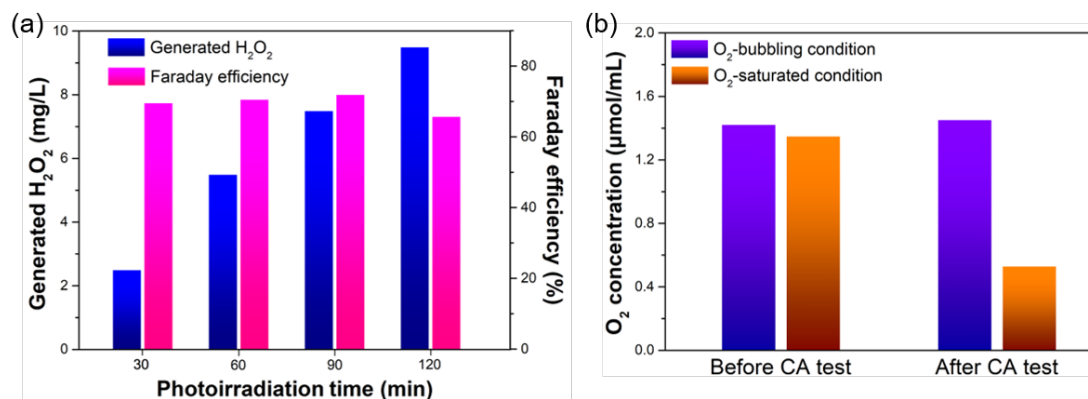


**Figure 2-19.** Amounts of H<sub>2</sub>O<sub>2</sub> produced as a function of photoirradiation time and effect of O<sub>2</sub> concentration. (a) H<sub>2</sub>O<sub>2</sub> generated by the Au-In<sub>2</sub>S<sub>3</sub>/Cu<sub>3</sub>BiS<sub>3</sub> electrode in an O<sub>2</sub>-bubbling phosphate buffer electrolyte (0.1 M, pH = 7) under a potentiostatic condition at +0.4 V<sub>RHE</sub> with visible light (420–800 nm, 100 mW/cm<sup>2</sup>) irradiation and corresponding Faraday efficiency. (b) O<sub>2</sub> concentrations before and after a 1 h CA test under O<sub>2</sub>-bubbling and O<sub>2</sub>-saturated conditions.

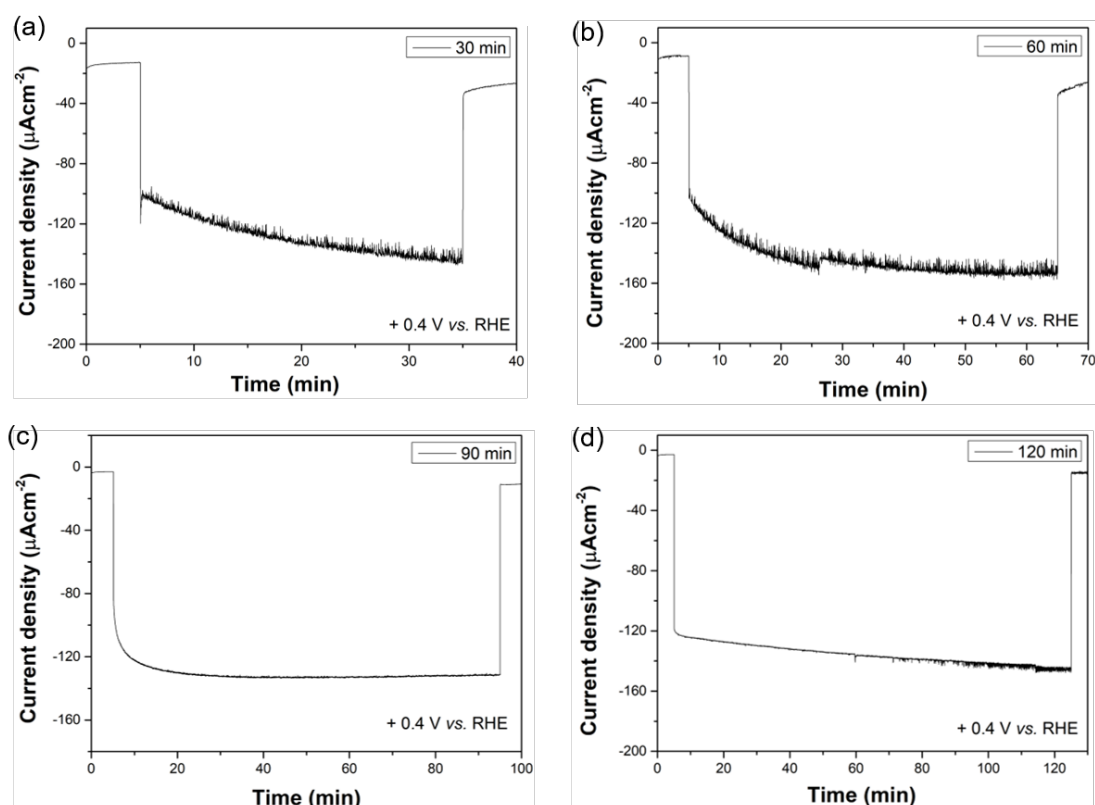


**Figure 2-20.** Time courses of the photocurrent of Au-In<sub>2</sub>S<sub>3</sub>/Cu<sub>3</sub>BiS<sub>3</sub> electrodes in an O<sub>2</sub>-bubbling phosphate buffer electrolyte (0.1 M, pH = 7) with visible light (420–800 nm, 100 mW/cm<sup>2</sup>) irradiation under a potentiostatic condition at +0.4 V vs. V<sub>RHE</sub>. (a) Irradiation time was 30 min (b) Irradiation time was 60 min (c) Irradiation time was 90 min (d) Irradiation time was 120 min.

We are convinced that the use of Au-In<sub>2</sub>S<sub>3</sub>/Cu<sub>3</sub>BiS<sub>3</sub> to generate H<sub>2</sub>O<sub>2</sub> is a pioneering work because the previously electrodes with PEC ORR activity are mostly organic

compounds such as polymers or dyes. Compared with the advanced photocathode materials reported in recent years, Au-In<sub>2</sub>S<sub>3</sub>/Cu<sub>3</sub>BiS<sub>3</sub> electrodes can provide a competitive level of H<sub>2</sub>O<sub>2</sub> production (details could be seen in **Table 2-3**). C. Li et al. reported the highest rate of stable and continuous generation of hydrogen peroxide using photocathodes made by pTTh. However, the cost of precursor for preparing the electrode was extremely high (26200 yen/g). Gd-doped CuBi<sub>2</sub>O<sub>4</sub>/CuO electrode reported by Z. Li et al. could generate 1.3 mmol of H<sub>2</sub>O<sub>2</sub> within 30 minutes. Unfortunately, this system required an electrolyte of 0.1 M KOH since the CuO coating could be easily decomposed under acidic and neutral conditions. In this case, such strong alkaline conditions restricted the accumulation of H<sub>2</sub>O<sub>2</sub>. Therefore, developing a relatively-stable and cost-efficient inorganic photocathode for efficient H<sub>2</sub>O<sub>2</sub> production is still of great urgent. Au-In<sub>2</sub>S<sub>3</sub>/Cu<sub>3</sub>BiS<sub>3</sub> could photoelectrochemically generate H<sub>2</sub>O<sub>2</sub> in the acidic/neutral condition. The stability is also significantly higher than other inorganic electrodes for PEC production of H<sub>2</sub>O<sub>2</sub>. Additionally, this Au-In<sub>2</sub>S<sub>3</sub>/Cu<sub>3</sub>BiS<sub>3</sub> electrode is cost-efficient and highly selective, which could inspire other researchers to further develop efficient PEC systems for H<sub>2</sub>O<sub>2</sub> production.

**Table 2-3.** Comparison of different photocathodes for H<sub>2</sub>O<sub>2</sub> producing with current study.

Photocathode	Light source	Added bias	Rate of producing H <sub>2</sub> O <sub>2</sub>	Faraday efficiency	Ref.
Au-In <sub>2</sub> S <sub>3</sub> /CBS	420-800 nm 100 mW/cm <sup>2</sup>	0.40 V vs. RHE	161.7 μM/h	71%	This work
BH <sub>4</sub> dyes sensitized NiO	λ>400 nm 100 mW/cm <sup>2</sup>	0.42 V vs. RHE	53.8 μM/h	60%	[48]
Porphyrin sensitized NiO	623 nm LED light	0.55 V vs. RHE	54.2 μM/h	100%	[49]
Epindolidione	Tungsten halogen lamp 60 mW/cm <sup>2</sup>	0.26 V vs. RHE	62.5 μM/h	95%	[50]
Eumelanin	White LED 255 mW/cm <sup>2</sup>	0.26 V vs. RHE	29.2 μM/h	90%	[51]
PN/Au/PTCDI	Tungsten halogen lamp 100 mW/cm <sup>2</sup>	0.32 V vs. RHE	-	60-80%	[52]
Polyterthiophene	λ>420 nm 100 mW cm <sup>-2</sup>	0.65 V vs. RHE	1.1 mM/h	80-96%	[53]
Gd-doped CuBi <sub>2</sub> O <sub>4</sub> /CuO	AM 1.5G sunlight	0.65 V vs. RHE	1.3 mM in 30 min	-	[54]

The difference between activities may be due to the changes of O<sub>2</sub> concentrations in the aqueous electrolyte over time. Under the gas-proof condition (O<sub>2</sub>-saturated), O<sub>2</sub> was continuously converted to H<sub>2</sub>O<sub>2</sub>, resulting in a decrease in O<sub>2</sub> concentration in the cathode compartment. Under the condition of O<sub>2</sub>-bubbling, the O<sub>2</sub> concentration remains constant, and the interaction between the electrode surface and O<sub>2</sub> will be more efficient. To prove this assumption, O<sub>2</sub> concentrations before and after a 1 h CA test under the two conditions were measured by Micro-GC (**Figure 2-19b**), and the results showed that the O<sub>2</sub> concentration after the reaction under the gas-proof condition (O<sub>2</sub>-saturated) was only 1/3 of that under the condition of O<sub>2</sub> bubbling. Furthermore, the oxygen bubbling may accelerate the electrode surface's mass transfer process [55]. Since the superoxide radical could be more uniformly dispersed in the electrolyte, it caused minor damage to the electrodes so that the system could maintain a higher Faraday efficiency. Moreover, we performed XRD analysis and ICP-AES analysis to compare the CBS electrodes before and after the reaction, and the species of the CBS electrodes did not change (**Figure 2-21 and 2-22**).

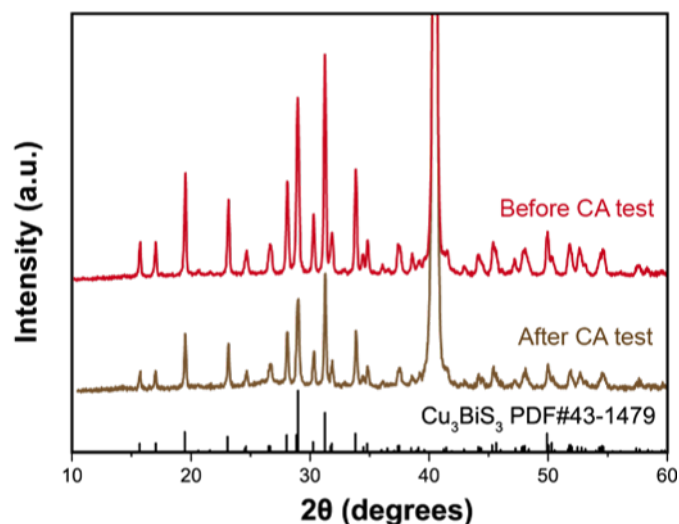


**Figure 2-21.** XRD analysis of Cu<sub>3</sub>BiS<sub>3</sub> before and after a 2 h CA test.



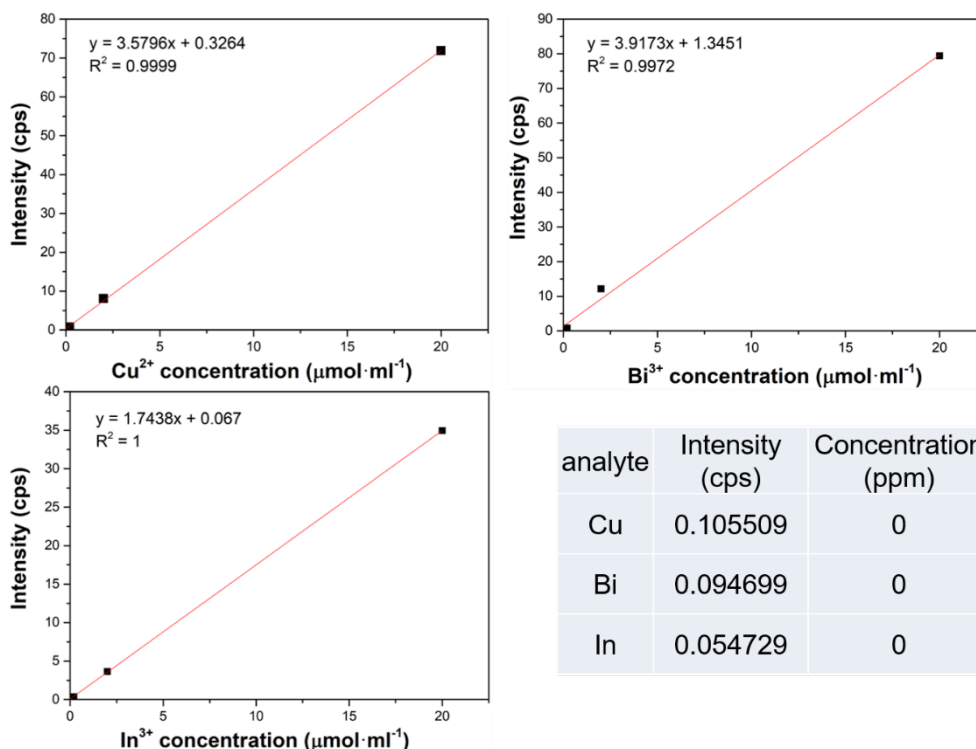


**Figure 2-22.** ICP-AES analysis for the aqueous electrolyte after photoelectrochemical reaction.

Subsequently, three cycle experiments (two hours each time) for  $\text{H}_2\text{O}_2$  generation were carried out, and the Faraday efficiency could be maintained at 84.5% of the first time (**Figure 2-23**). The results indicated that the as-prepared  $\text{Au-In}_2\text{S}_3/\text{CBS}$  electrode showed satisfactory stability for PEC production of  $\text{H}_2\text{O}_2$ .

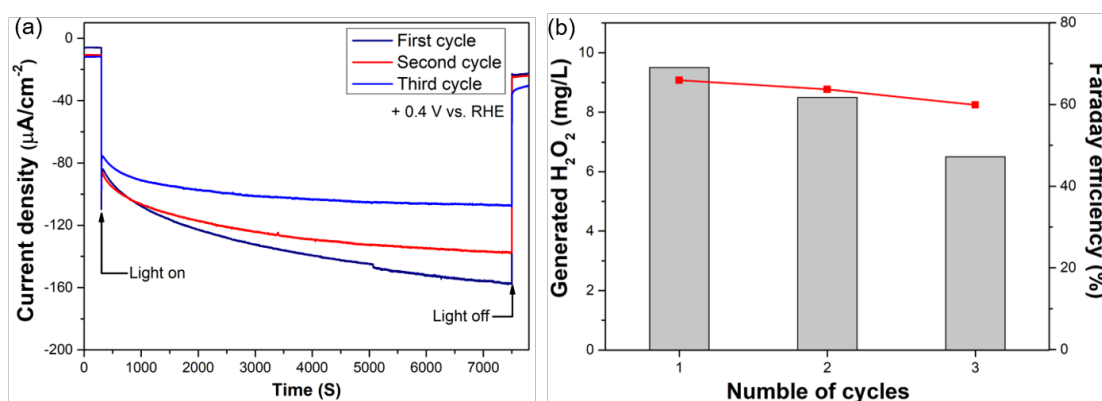


**Figure 2-23.** (a) Time courses of the photocurrent of an  $\text{Au-In}_2\text{S}_3/\text{CBS}$  electrode in an  $\text{O}_2$ -bubbling phosphate buffer electrolyte (0.1 M, pH = 7) with visible light (420–800 nm,  $100 \text{ mW}/\text{cm}^2$ ) irradiation under a potentiostatic condition at +0.4 V vs.  $V_{\text{RHE}}$ . (b) Generated  $\text{H}_2\text{O}_2$  for each cycle and corresponding Faraday efficiency.

### 3.4 Photoelectrocatalytic mechanism analysis

In order to further confirm the reaction mechanism, we performed a superoxide radical capture experiment based on the nucleophilic substitution reactions between acyl halides and superoxide. In an aqueous solution, superoxide radicals quickly react with protons to generate  $\text{H}_2\text{O}_2$  and  $\text{O}_2$ . Therefore, the superoxide radical capture experiment was carried out in a non-aqueous solution with benzoyl chloride (BzCl) as a model compound to react with photoelectrochemically generated superoxide radical anion ( $\cdot\text{O}_2^-$ ) (**Figure 2-24a**). As shown in **Figure 2-24b**, the amount of  $\text{H}_2\text{O}_2$  in the non-aqueous solution and the corresponding Faraday efficiency both decreased. This may be due to the fact that the electrode is more hydrophilic as an inorganic sulfide. After adding BzCl, the amount of  $\text{H}_2\text{O}_2$  generated decreased obviously (**Figure 2-24c**), indicating that  $\cdot\text{O}_2^-$ , as an important intermediate product, was captured by BzCl and could not be further reduced to  $\text{H}_2\text{O}_2$  [56]. Therefore, the reaction mechanism can be briefly described as photoexcited electrons on CBS reducing  $\text{O}_2$  to  $\cdot\text{O}_2^-$  and then further being disproportionated to generate  $\text{H}_2\text{O}_2$ . The above conclusion is similar to previous works on  $2e^-$  ORR to generate  $\text{H}_2\text{O}_2$  [57-59]. In addition, the single interfacial electron transfer simplified the PEC system and minimized the opportunities for charge recombination [49].

The process of photoelectrochemical generation of  $\text{H}_2\text{O}_2$  is summarized in **Figure 2-24d**. A compact and uniform CBS and  $\text{In}_2\text{S}_3$  layer formed a typical type II heterojunction structure, which helped the separation and transfer of charge. Au nanoparticles worked as a co-catalyst to further enhance the charge transfer and selectivity of  $\text{O}_2/\text{H}_2\text{O}_2$  reduction. Photon absorption caused both semiconductors to be excited (step 1). The holes transferred (HT) from  $\text{In}_2\text{S}_3$  to CBS and then further transferred to the photoanode instead of recombining with the electrons (step 2). As a result, electrons were transferred (ET) from CBS to Au nanoparticles and then further reduced  $\text{O}_2$  to form  $\cdot\text{O}_2^-$  (step 3), which could be easily disproportionated in water to generate  $\text{H}_2\text{O}_2$ . Thus, we have constructed a photoelectrode activity-selectivity improvement strategy. Firstly, the film prepared by the SPD was excellent in denseness, which resulted in faster charge transmission and 1.5 times increased photocurrent than that of the films prepared by EPD. Secondly, the  $p$ - $n$  heterojunction between the  $p$ -type semiconductor CBS and the  $n$ -type semiconductor

$\text{In}_2\text{S}_3$  further promoted charge separation. In this step, the smooth CBS electrode surface will play an important role to improve the charge transfer at the interface between the two semiconductors. The tight combination of  $p$ -type and  $n$ -type semiconductors increased the photocurrent by 131 times than before  $\text{In}_2\text{S}_3$  modification. Thirdly, the deposition of Au nanoparticles reduced the free energy required for ORR, improving the selectivity of  $\text{O}_2$  to  $\text{H}_2\text{O}_2$ . Compared with the electrode without Au deposition, the rate of  $\text{H}_2\text{O}_2$  generation is increased *ca.* 3 times.

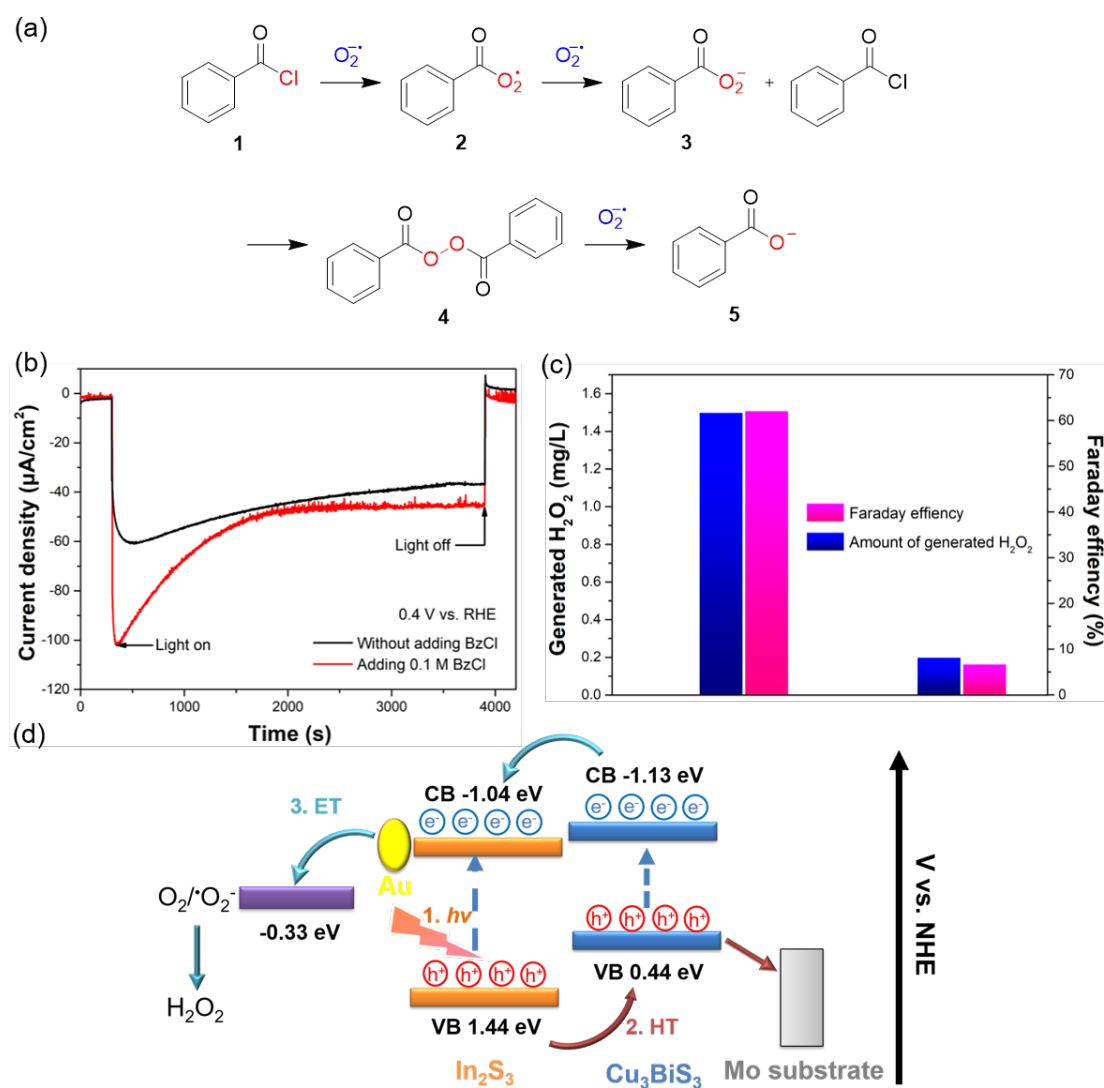


**Figure 2-24. Superoxide radical capture experiment and speculated reaction mechanism.** (a) Proposed reactions between benzoyl chloride and superoxide radical anions. (b) CA test for adding BzCl (red line) and without adding BzCl (blue line). Time courses of the photocurrent of Au- $\text{In}_2\text{S}_3$ /CBS electrodes in an  $\text{O}_2$ -bubbling non-aqueous electrolyte with visible light (420–800 nm, 100  $\text{mW}/\text{cm}^2$ ) irradiation under a potentiostatic condition at +0.4 V vs.  $V_{\text{RHE}}$ . (c) Amounts of  $\text{H}_2\text{O}_2$  generated by Au- $\text{In}_2\text{S}_3$ /CBS electrodes under the condition of addition or without no addition of BzCl with visible light

(420-800 nm, 100 mW/cm<sup>2</sup>) irradiation for 1 h and corresponding Faraday efficiencies. (d) Energy diagram for Au-In<sub>2</sub>S<sub>3</sub>/CBS electrodes depicting the process of H<sub>2</sub>O<sub>2</sub> formation.

## 4. Conclusions

In summary, in situ photoelectrochemical synthesis of H<sub>2</sub>O<sub>2</sub> was achieved in this study for the first time by using an inorganic sulphide photocathode under visible light irradiation. Under the condition of visible light irradiation, the Au-loaded In<sub>2</sub>S<sub>3</sub>/CBS electrode could produce H<sub>2</sub>O<sub>2</sub> at a rate of 5.5 mg·L<sup>-1</sup>·h<sup>-1</sup>·cm<sup>-1</sup> with good Faraday efficiency. The PEC pathway can be briefly described as photo-excited electrons on CBS reducing O<sub>2</sub> to <sup>•</sup>O<sub>2</sub><sup>-</sup> and then further being disproportionated to generate H<sub>2</sub>O<sub>2</sub>. Although superoxide radicals could cause some damage to the surface of the electrode, they minimize the opportunities for charge recombination. Compared with the traditional dye-sensitized photocathode, this study provided a practical strategy for designing a highly efficient inorganic photocathode for producing H<sub>2</sub>O<sub>2</sub> and will evoke more interest in ORR via a PEC system.

## References

- [1] S. Fukuzumi, Production of liquid solar fuels and their use in fuel cells, *Joule*, 1 (2017), pp. 689–738. <https://doi.org/10.1016/j.joule.2017.07.007>.
- [2] S. Fukuzumi, Y. M. Lee, W. Nam, Solar-driven production of hydrogen peroxide from water and dioxygen, *Chem.*, 24 (2018), pp. 5016–5031. <https://doi.org/10.1002/chem.201704512>.
- [3] S. Siahrostami, S. J. Villegas, A. H. B. Mostaghimi, S. Back, A. B. Farimani, H. Wang, K. A. Persson, J. Montoya, A review on challenges and successes in atomic-scale design of catalysts for electrochemical synthesis of hydrogen peroxide, *ACS Catal.*, 10 (2020), pp. 7495–7511. <https://doi.org/10.1021/acscatal.0c01641>.
- [4] X. Zeng, Y. Liu, X. Hu, X. Zhang, Photoredox catalysis over semiconductors for light-driven hydrogen peroxide production, *Green Chem.*, 23 (2021), pp. 1466–1494. <https://doi.org/10.1039/D0GC04236F>.
- [5] S. A. Mousavi Shaegh, N.-T. Nguyen, S. M. Mousavi Ehteshami, S. H. Chan, A membraneless hydrogen peroxide fuel cell using prussian blue as cathode material, *Energy Environ. Sci.*, 5 (2012), pp. 8225–8228. <https://doi.org/10.1039/C2EE21806B>.
- [6] Y. Yamada, M. Yoneda, S. Fukuzumi, High and robust performance of H<sub>2</sub>O<sub>2</sub> fuel cells in the presence of scandium ion, *Energy Environ. Sci.*, 8 (2015), pp. 1698–1701. <https://doi.org/10.1039/C5EE00748H>.
- [7] M. Xiao, Z. Wang, M. Lyu, B. Luo, S. Wang, G. Liu, H. M. Cheng, L. Wang, Hollow nanostructures for photocatalysis: Advantages and challenges, *Adv. Mater.*, 31 (2019), Article 1801369. <https://doi.org/10.1002/adma.201801369>.
- [8] Z. Teng, H. Lv, C. Wang, H. Xue, H. Pang, G. Wang, Bandgap engineering of ultrathin graphene-like carbon nitride nanosheets with controllable oxygenous functionalization, *Carbon*, 113 (2017), pp. 63–75. <https://doi.org/10.1016/j.carbon.2016.11.030>.
- [9] Z. Teng, W. Cai, W. Sim, Q. Zhang, C. Wang, C. Su, T. Ohno, Photoexcited single metal atom catalysts for heterogeneous photocatalytic H<sub>2</sub>O<sub>2</sub> production: Pragmatic guidelines for predicting charge separation, *Appl. Catal. B-Environ.*, 282 (2021), Article 119589. <https://doi.org/10.1016/j.apcatb.2020.119589>.
- [10] Z. Teng, Q. Zhang, H. Yang, K. Kato, W. Yang, Y. Lu, S. Liu, C. Wang, A. Yamakata, C. Su, B. Liu, T. Ohno, Atomically dispersed antimony on carbon nitride for the artificial photosynthesis of hydrogen peroxide, *Nat. Catal.*, 4 (2021), pp. 374–384. <https://doi.org/10.1038/s41929-021-00605-1>.
- [11] M. Teranishi, R. Hoshino, S. Naya, H. Tada, Gold-nanoparticle-loaded carbonate-modified titanium(IV) oxide surface: visible-light-driven formation of hydrogen peroxide from oxygen, *Angew. Chem., Int. Ed.*, 55 (2016), pp. 12773–12777. <https://doi.org/10.1002/anie.201606734>.
- [12] J. Liu, Y. Zou, B. Jin, K. Zhang, J. H. Park, Hydrogen peroxide production from solar water oxidation, *ACS Energy Lett.*, 4 (2019), pp. 3018–3027. <https://doi.org/10.1021/acseenergylett.9b02199>.
- [13] K. Fuku, Y. Miyase, Y. Miseki, T. Gunji, K. Sayama, WO<sub>3</sub>/BiVO<sub>4</sub> photoanode coated with mesoporous Al<sub>2</sub>O<sub>3</sub> layer for oxidative production of hydrogen peroxide from water with high selectivity, *RSC Adv.*, 7 (2017), pp. 47619–47623. <https://doi.org/10.1039/C7RA09693C>.

- [14] S. Jin, X. Ma, J. Pan, C. Zhu, S. E. Saji, J. Hua, X. Xu, L. Sun, Z. Yin, Oxygen vacancies activating surface reactivity to favor charge separation and transfer in nanoporous BiVO<sub>4</sub> photoanodes, *Appl. Catal. B-Environ.*, 281 (2021), Article 119477. <https://doi.org/10.1016/j.apcatb.2020.119477>.
- [15] J. Sun, Y. Yu, A. E. Curtze, X. Liang, Y. Wu, Dye-sensitized photocathodes for oxygen reduction: efficient H<sub>2</sub>O<sub>2</sub> production and aprotic redox reactions, *Chem. Sci.*, 10 (2019), pp. 5519–5527. <https://doi.org/10.1039/C9SC01626K>.
- [16] W. Fan, B. Zhang, X. Wang, W. Ma, D. Li, Z. Wang, M. Dupuis, J. Shi, S. Liao, C. Li, Efficient hydrogen peroxide synthesis by metal-free polyterthiophene via photoelectrocatalytic dioxygen reduction, *Energy Environ. Sci.*, 13 (2020), pp. 238–245. <https://doi.org/10.1039/C9EE02247C>.
- [17] H. Thadani, A. Deacon, T. Peters, Diagnosis and management of porphyria, *BMJ*, 320 (2000), pp. 1647–1651. <https://doi.org/10.1136/bmj.320.7250.1647>.
- [18] Z. Li, Q. Xu, F. Gou, B. He, W. Chen, W. Zheng, X. Jiang, K. Chen, C. Qi, D. Ma, Gd-doped CuBi<sub>2</sub>O<sub>4</sub>/CuO heterojunction film photocathodes for photoelectrochemical H<sub>2</sub>O<sub>2</sub> production through oxygen reduction. *Nano Res.*, (2021). <https://doi.org/10.1007/s12274-021-3638-y>.
- [19] Y. Xu, Schoonen, A. A. Martin, The absolute energy positions of conduction and valence bands of selected semiconducting minerals, *Am. Mineral.*, 85 (2000), pp. 543–556. <https://doi.org/10.2138/am-2000-0416>.
- [20] M. Li, R. Zhao, Y. Su, J. Hu, Z. Yang, Y. Zhang, Synthesis of CuInS<sub>2</sub> nanowire arrays via solution transformation of Cu<sub>2</sub>S self-template for enhanced photoelectrochemical performance, *Appl. Catal. B-Environ.*, 203 (2017), pp. 715–724. <https://doi.org/10.1016/j.apcatb.2016.10.051>.
- [21] F. Xu, J. Zhang, B. Zhu, J. Yu, J. Xu, CuInS<sub>2</sub> sensitized TiO<sub>2</sub> hybrid nanofibers for improved photocatalytic CO<sub>2</sub> reduction, *Appl. Catal. B-Environ.*, 23 (2018), pp. 194–202. <https://doi.org/10.1016/j.apcatb.2018.02.042>.
- [22] R. Wang, X. Tong, A. I. Channa, Q. Zeng, J. Sun, C. Liu, X. Li, J. Xu, F. Lin, G. S. Selopal, F. Rosei, Y. Zhang, J. Wu, H. Zhao, A. Vomiero, X. Sun, Z. M. Wang, Environmentally friendly Mn-alloyed core/shell quantum dots for high-efficiency photoelectrochemical cells, *J. Mater. Chem. A*, 8 (2020), pp. 10736–10741. <https://doi.org/10.1039/D0TA00953A>.
- [23] W. Yang, Y. Oh, J. Kim, M. J. Jeong, J. H. Park, J. Moon, Molecular chemistry-controlled hybrid ink-derived efficient Cu<sub>2</sub>ZnSnS<sub>4</sub> photocathodes for photoelectrochemical water splitting, *ACS Energy Lett.*, 1 (2016), pp. 1127–1136. <https://doi.org/10.1021/acsenergylett.6b00453>.
- [24] F. Ozel, E. Aslan, B. Istanbulu, O. Akay, I. H. Patir, Photocatalytic hydrogen evolution based on Cu<sub>2</sub>ZnSnS<sub>4</sub>, Cu<sub>2</sub>NiSnS<sub>4</sub> and Cu<sub>2</sub>CoSnS<sub>4</sub> nanocrystals, *Appl. Catal. B-Environ.*, 198 (2016), pp. 67–73. <https://doi.org/10.1016/j.apcatb.2016.05.053>.
- [25] L. Yu, R. S. Kokenyesi, D. A. Keszler, and A. Zunger, Inverse design of high absorption thin-film photovoltaic materials, *Adv. Energy Mater.*, 3 (2013), pp. 43–48. <https://doi.org/10.1002/aenm.201200538>.
- [26] T. Ohno, M. Akiyoshi, T. Umebayashi, K. Asai, T. Mitsui, M. Matsumura, Preparation of S-doped TiO<sub>2</sub> photocatalysts and their photocatalytic activities under visible light, *Appl. Catal. A*, 265 (2004), pp. 115–121. <https://doi.org/10.1016/j.apcata.2004.01.007>.

- [27] N. Mufti, T. Amrillah, A. Taufiq, Sunaryono, Aripriharta, M. Diantoro, Zulhadjri, H. Nur, Review of CIGS-based solar cells manufacturing by structural engineering, *Solar Energy*, 207 (2020), pp. 1146–1157. <https://doi.org/10.1016/j.solener.2020.07.065>.
- [28] T. J. Whittles, T. D. Veal, C. N. Savory, P. J. Yates, P. A. E. Murgatroyd, J. T. Gibbon, M. Birkett, R. J. Potter, J. D. Major, K. Durose, D. O. Scanlon, V. R. Dhanak, Band alignments, band gap, core levels, and valence band states in  $\text{Cu}_3\text{BiS}_3$  for photovoltaics, *ACS Appl. Mater. Interfaces*, 11 (2019), pp. 27033–27047. <https://doi.org/10.1021/acsami.9b04268>.
- [29] J. Li, Y. Zhao, X. Han, D. Xiao, A facile strategy for fabricating particle-on-flower  $\text{Au-Cu}_3\text{BiS}_3$  nanostructures for enhanced photoelectrocatalytic activity in water splitting, *New J. Chem.*, 45 (2021), pp. 1231–1239. <https://doi.org/10.1039/D0NJ03448G>.
- [30] S. Kamimura, N. Beppu, Y. Sasaki, T. Tsubota, T. Ohno, Platinum and indium sulfide-modified  $\text{Cu}_3\text{BiS}_3$  photocathode for photoelectrochemical hydrogen evolution, *J. Mater. Chem. A*, 5 (2017), pp. 10450–10456. <https://doi.org/10.1039/C7TA02740K>.
- [31] J. K. Nørskov, J. Rossmeisl, A. Logadottir and L. Lindqvist, Origin of the overpotential for oxygen reduction at a fuel-cell cathode, *J. Phys. Chem. B*, 108 (2004), pp. 17886–17892. <https://doi.org/10.1021/jp047349j>.
- [32] B. Dong, Y. Qi, J. Cui, B. Liu, F. Xiong, X. Jiang, Z. Li, Y. Xiao, F. Zhang, C. Li, Synthesis of  $\text{BaTaO}_2\text{N}$  oxynitride from Ba-rich oxide precursor for construction of visible-light-driven Z-scheme overall water splitting, *Dalton Trans.*, 46 (2017), pp. 10707–10713. <https://doi.org/10.1039/C7DT00854F>.
- [33] J. Wang, Y. Song, J. Hu, Y. Li, Z. Wang, P. Yang, G. Wang, Q. Ma, Q. Che, Y. Dai, B. Huang, Photocatalytic hydrogen evolution on p-type tetragonal zircon  $\text{BiVO}_4$ , *Appl. Catal. B-Environ.*, 251 (2019), pp. 94–101. <https://doi.org/10.1016/j.apcatb.2019.03.049>.
- [34] J. Zheng, Z. Lei, Incorporation of  $\text{CoO}$  nanoparticles in 3D marigold flower-like hierarchical architecture  $\text{MnCo}_2\text{O}_4$  for highly boosting solar light photo-oxidation and reduction ability, *Appl. Catal. B-Environ.*, 237 (2018), pp. 1–8. <https://doi.org/10.1016/j.apcatb.2018.05.060>.
- [35] S. Xu, N. Cheng, H. Yin, D. Cao, B. Mi, Electro spray preparation of  $\text{CuInS}_2$  films as efficient counter electrode for dye-sensitized solar cells, *Chem. Eng. J.*, 397 (2020), pp. 1385–8947. <https://doi.org/10.1016/j.cej.2020.125463>.
- [36] H. Deng, X. Fei, Y. Yang, J. Fan, J. Yu, B. Cheng, L. Zhang, S-scheme heterojunction based on p-type  $\text{ZnMn}_2\text{O}_4$  and n-type  $\text{ZnO}$  with improved photocatalytic  $\text{CO}_2$  reduction activity, *Chem. Eng. J.*, 409 (2021), Article 127377. <https://doi.org/10.1016/j.cej.2020.127377>.
- [37] J. Leng, Z. Wang, J. Wang, H. Wu, G. Yan, X. Li, H. Guo, Y. Liu, Q. Zhang, Z. Guo, Advances in nanostructures fabricated via spray pyrolysis and their applications in energy storage and conversion, *Chem. Soc. Rev.*, 48 (2019), pp. 3015–3072. <https://doi.org/10.1039/C8CS00904J>.
- [38] Y. Li, H. L. Wang, L. M. Xie, Y. Y. Liang, G. S. Hong and H. J. Dai,  $\text{MoS}_2$  nanoparticles grown on graphene: an advanced catalyst for the hydrogen evolution reaction, *J. Am. Chem. Soc.*, 133 (2011), pp. 7296–7299. <https://doi.org/10.1021/ja201269b>.
- [39] S. Yang, K. Liu, W. Han, L. Li, F. Wang, X. Zhou, H. Li, T. Zhai, Salt-assisted growth of p-type  $\text{Cu}_9\text{S}_5$  nanoflakes for p-n heterojunction photodetectors with high responsivity, *Adv. Funct. Mater.*, 30 (2019), Article 1908382. <https://doi.org/10.1002/adfm.201908382>.
- [40] S. Kamimura, Y. Sasaki, M. Kanaya, T. Tsubota, T. Ohno, Improvement of selectivity for  $\text{CO}_2$  reduction by using  $\text{Cu}_2\text{ZnSnS}_4$  electrodes modified with different buffer layers ( $\text{CdS}$  and

- In<sub>2</sub>S<sub>3</sub>) under visible light irradiation, *RSC Adv.*, 6 (2016), pp. 112594–112601. <https://doi.org/10.1039/C6RA22546B>.
- [41] T. J. Whittles, T. D. Veal, C. N. Savory, P. J. Yates, P. A. E. Murgatroyd, J. T. Gibbon, M. Birkett, R. J. Potter, J. D. Major, K. Durose, D. O. Scanlon, V. R. Dhanak, Band alignments, band gap, core levels, and valence band states in Cu<sub>3</sub>BiS<sub>3</sub> for photovoltaics, *ACS Appl. Mater. Interfaces*, 11 (2019), pp. 27033–27047. <https://doi.org/10.1021/acsami.9b04268>.
- [42] A. Mumtaz, N. M. Mohamed, M. Mazhar, M. A. Ehsan, M. Saheed, Core–shell vanadium modified titania@β-In<sub>2</sub>S<sub>3</sub> hybrid nanorod arrays for superior interface stability and photochemical activity, *ACS Appl. Mater. Interfaces*, 8 (2016), pp. 9037–9049. <https://doi.org/10.1021/acsami.5b10147>.
- [43] A. J. Young, M. Sauer, G. M. D. M. Rubio, A. Sato, A. Foelske, C. J. Serpell, J. M. Chin, M. R. Reithofer, One-step synthesis and XPS investigations of chiral NHC–Au(0)/Au(i) nanoparticles, *Nanoscale*, (11) 2019, pp. 8327–8333. <https://doi.org/10.1039/C9NR00905A>.
- [44] W. Tang, H. Lin, A. Kleiman-Shwarsctein, G. D. Stucky, E. W. McFarland, Size-dependent activity of gold nanoparticles for oxygen electroreduction in alkaline electrolyte, *J. Phys. Chem. C*, 112 (2008), pp. 10515–10519. <https://doi.org/10.1021/jp710929n>.
- [45] K. Wang, J. Huang, H. Chen, Y. Wang, S. Song, Recent advances in electrochemical 2e oxygen reduction reaction for on-site hydrogen peroxide production and beyond, *Chem. Commun.*, 56 (2020), pp. 12109–12121. <https://doi.org/10.1039/D0CC05156J>.
- [46] J. K. Nørskov, J. Rossmeisl, A. Logadottir, L. Lindqvist, J. R. Kitchin, T. Bligaard, H. Jónsson, Origin of the Overpotential for Oxygen Reduction at a Fuel-Cell Cathode, *J. Phys. Chem. B*, 108 (2004), pp. 17886–17892. <https://doi.org/10.1021/jp047349j>.
- [47] V. Viswanathan, H. A. Hansen, J. Rossmeisl, J. K. Nørskov, Unifying the 2e– and 4e– Reduction of Oxygen on Metal Surfaces, *J. Phys. Chem. Lett.*, 3 (2012), pp. 2948–2951. <https://doi.org/10.1021/jz301476w>.
- [48] J. Sun, Y. Yu, A. E. Curtze, X. Liang, Y. Wu, Dye-sensitized photocathodes for oxygen reduction: efficient H<sub>2</sub>O<sub>2</sub> production and aprotic redox reactions, *Chem. Sci.*, 10 (2019) 5519–5527. <https://doi.org/10.1039/C9SC01626K>.
- [49] O. Jung, M. L. Pegis, Z. Wang, G. Banerjee, C. T. Nemes, W. L. Hoffeditz, J. T. Hupp, C. A. Schmuttenmaer, G. W. Brudvig, J. M. Mayer, Highly active NiO photocathodes for H<sub>2</sub>O<sub>2</sub> production enabled via outer-sphere electron transfer, *J. Am. Chem. Soc.*, 140 (2018) 11, 4079–4084. <https://doi.org/10.1021/jacs.8b00015>.
- [50] M. Jakešová, D. H. Apaydin, M. Sytnyk, K. Oppelt, W. Heiss, N. S. Sariciftci, E. D. Głowacki, Hydrogen-bonded organic semiconductors as stable photoelectrocatalysts for efficient hydrogen peroxide photosynthesis, *Adv. Funct. Mater.*, 26 (2016) 29, 5248–5254. <https://doi.org/10.1002/adfm.201601946>.
- [51] L. Migliaccio, M. Gryszel, V. Đerek, A. Pezzella, E. D. Głowacki, Aqueous photo(electro)catalysis with eumelanin thin films, *Mater. Horiz.*, 5 (2018) 984–990. <https://doi.org/10.1039/C8MH00715B>.
- [52] M. Gryszel, A. Markov, M. Vagin, E. D. Głowacki, Organic heterojunction photocathodes for optimized photoelectrochemical hydrogen peroxide production, *J. Mater. Chem. A*, 6 (2018) 24709–24716. <https://doi.org/10.1039/C8TA08151D>.
- [53] W. Fan, B. Zhang, X. Wang, W. Ma, D. Li, Z. Wang, M. Dupuis, J. Shi, S. Liao, C. Li, Efficient hydrogen peroxide synthesis by metal-free polyterthiophene via photoelectrocatalytic



- dioxygen reduction, *Energy Environ. Sci.*, 13 (2020) 238-245. <https://doi.org/10.1039/C9EE02247C>.
- [54] Z. Li, Q. Xu, F. Gou, B. He, W. Chen, W. Zheng, X. Jiang, K. Chen, C. Qi, D. Ma, Gd-doped  $\text{CuBi}_2\text{O}_4/\text{CuO}$  heterojunction film photocathodes for photoelectrochemical  $\text{H}_2\text{O}_2$  production through oxygen reduction. *Nano Res.* 14 (2021) 3439–3445. <https://doi.org/10.1007/s12274-021-3638-y>.
- [55] L. Li, Z. Hu, J. C. Yu, On-demand synthesis of  $\text{H}_2\text{O}_2$  by water oxidation for sustainable resource production and organic pollutant degradation, *Angew. Chem. Int. Ed.*, 59 (2020), pp. 20538–20544. <https://doi.org/10.1002/ange.202008031>.
- [56] J. Sun, Y. Yu, A. E. Curtze, X. Liang, Y. Wu, Dye-sensitized photocathodes for oxygen reduction: efficient  $\text{H}_2\text{O}_2$  production and aprotic redox reactions, *Chem. Sci.*, 10 (2019), pp. 5519–5527. <https://doi.org/10.1039/C9SC01626K>.
- [57] W. Fan, B. Zhang, X. Wang, W. Ma, D. Li, Z. Wang, M. Dupuis, J. Shi, S. Liao, C. Li, Efficient hydrogen peroxide synthesis by metal-free polyterthiophene via photoelectrocatalytic dioxygen reduction, *Energy Environ. Sci.*, 13 (2020), pp. 238–245. <https://doi.org/10.1039/C9EE02247C>.
- [58] J. Sun, Y. Wu, Anthraquinone redox relay for dye-sensitized photo-electrochemical  $\text{H}_2\text{O}_2$  production, *Angew. Chem. Int. Ed.*, 59 (2020), pp. 10904–10908. <https://doi.org/10.1002/anie.202003745>.
- [59] L. Migliaccio, M. Gryszel, V. Ęrek, A. Pezzella, E. D. Głowacki, Aqueous photo(electro)catalysis with eumelanin thin films, *Mater. Horiz.*, 5 (2018), pp. 984–990. <https://doi.org/10.1039/C8MH00715B>.

## PART 3

**Preparation of  $\text{Cu}_3\text{VS}_4$  photocathode and its application in the preparation of  $\text{H}_2\text{O}_2$  by oxygen reduction**

## 1. Introduction

In our group's previous work, Kawano San found that the CVS photocathode has extremely high selectivity for the reduction of oxygen to hydrogen peroxide, and the preparation conditions were optimized [1]. However, there are still a series of problems:

1. The photocurrent density of the CVS photocathode is only about  $50 \mu\text{A}\cdot\text{cm}^{-1}$ , and the corresponding Faradaic efficiency is 84.8%.

2. The CVS photocathode is susceptible to photo-corrosion and has poor stability. The melted Cu ions can also catalyze the decomposition of hydrogen peroxide.

3. Several n-type semiconductors were used to modify the CVS electrode, but the energy band structure was not matched, and the photocurrent density could not be effectively improved.

A copper-based sulfide semiconductor with cubic unit cells,  $\text{Cu}_3\text{VS}_4$ , exists as a p-type semiconductor (Figure 3-1a). The valence band maximum is formed by the Cu 3d + S 3p hybrid orbital and the conduction band minimum is formed by the V 3d + S 3p hybrid orbital (Figure 3-1b) [2]. By changing the valence band maximum,  $\text{Cu}_3\text{VS}_4$  can be made to conform to the energy band structure of other n-type semiconductors, resulting in p-n heterojunctions for improved charge separation efficiency. As  $\text{Cu}_3\text{VS}_4$  has a conduction band value of -1.13 V vs. NHE, there is no need to change the conduction band minimum to ensure reduction capability. Copper ions can be substituted during the doping process to change the valence band maximum. Apart from changing the conduction band minimum, doping with Se and Te ions (the most commonly used methods for replacing sulfur ions) will also lead to a further reduction in the band gap for  $\text{Cu}_3\text{VS}_4$  [3], which is only 1.56 eV for our preparing method. A further reduction in the band gap may lead to an increase in the electron-hole complexation rate, resulting in a reduction in photocurrent density.

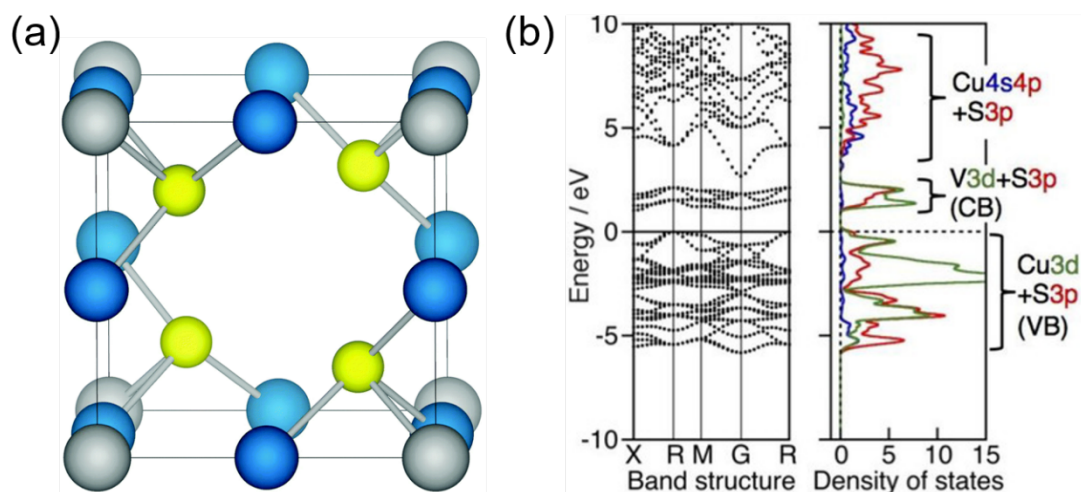


**Figure 3-1.** (a) The structure of the cubic chalcogenides  $\text{Cu}_3\text{VS}_4$ . Copper ions, vanadium ions, and sulfur anions are shown in blue, grey, and yellow, respectively [3]. (b) Band structure and density of states for  $\text{Cu}_3\text{VS}_4$  calculated by density functional theory [2].

Many elements have been reported to replace copper ions, including Ni, Zn, Cd, Hg, Ag, Ga, In, Sn, etc [4]. Divalent cations (e.g., Zn, Cd) usually do not form a homogeneous phase upon incorporation into copper-based sulfide. Exposure of binary copper sulfides to divalent cations usually leads to cation exchange, which can produce heterostructures of two different compositions and crystal phases. Trivalent and tetravalent cations (e.g., In, Sn, Ga) can generally be incorporated to form homogeneous doped or alloyed nanomaterials. A monovalent cation may be able to replace  $\text{Cu}^{1+}$  in some cases, but the ionic radius must be taken into account. S.Yilmaz et al. reported that Ga-doping was beneficial for increasing the carrier concentration and improving the carrier mobility in the application of CdS films [5]. W. Septina et al. reported  $\text{Cu}(\text{In,Ga})\text{S}_2$  thin films with different Ga doping ratios, and found that Ga doping can effectively increase the valence band maximum and enhance the onset potential [6]. Doping with Ag mainly affects the morphology of the film [7]. As reported by W. Liu et al. [8], Ag doping increases carrier concentration, decreases carrier mobility, and lowers conductivity and power. However, as the main group element of Cu ions, Ag doping is still a worthy choice. Based on the above reasons, Ag and Ga ions with similar ionic radii to  $\text{Cu}^{1+}$  ions were chosen for doping in order to change the valence band maximum of the CVS electrode.

In this work, the CVS electrodes were modified by Ag and Ga doping, which effectively improved the photocurrent density and hydrogen peroxide yield, respectively. The Ag-doped CVS electrode effectively increases the particle size of the material, resulting in a significant increase in photocurrent density and stability. The optimal Ag doping level was determined to be 3%, in which the photocurrent density reached  $160 \mu\text{A}\cdot\text{cm}^{-1}$ , the  $\text{H}_2\text{O}_2$  yield was  $4.04 \text{ mg}\cdot\text{L}^{-1}\cdot\text{h}^{-1}\cdot\text{cm}^{-1}$ , and the Faradaic efficiency was 95.6%. Ga doping increases the photocurrent density by a factor of six, which can be attributed to two factors: first, Ga doping effectively increases the bandgap width of the CVS electrode, leading to an increase in light absorption efficiency; The conductivity increases, indicating an increase in charge concentration, thereby increasing the charge separation efficiency. The optimum Ga doping amount was determined to be 0.5%, in which the photocurrent density reached  $325 \mu\text{A}\cdot\text{cm}^{-1}$ , the  $\text{H}_2\text{O}_2$  yield was  $7.52 \text{ mg}\cdot\text{L}^{-1}\cdot\text{h}^{-1}\cdot\text{cm}^{-1}$ , and the Faradaic efficiency was 99%. Meanwhile, we found the reason why the photocurrent density could not be improved may be because of the pores between the CVS and Mo substrate and the formation of the  $\text{MoS}_2$  layer, which would lead to a decrease in the rate of charge transfer from the CVS to the Mo substrate, which affected the photocurrent density and hydrogen peroxide production. The reason for the decrease of the photocurrent density on the n-type semiconductor modified CVS electrode is summarized as the formation of Z-scheme heterojunction, which leads to the occurrence of competitive reactions, resulting in the reduction of the generation of  $\text{H}_2\text{O}_2$ .

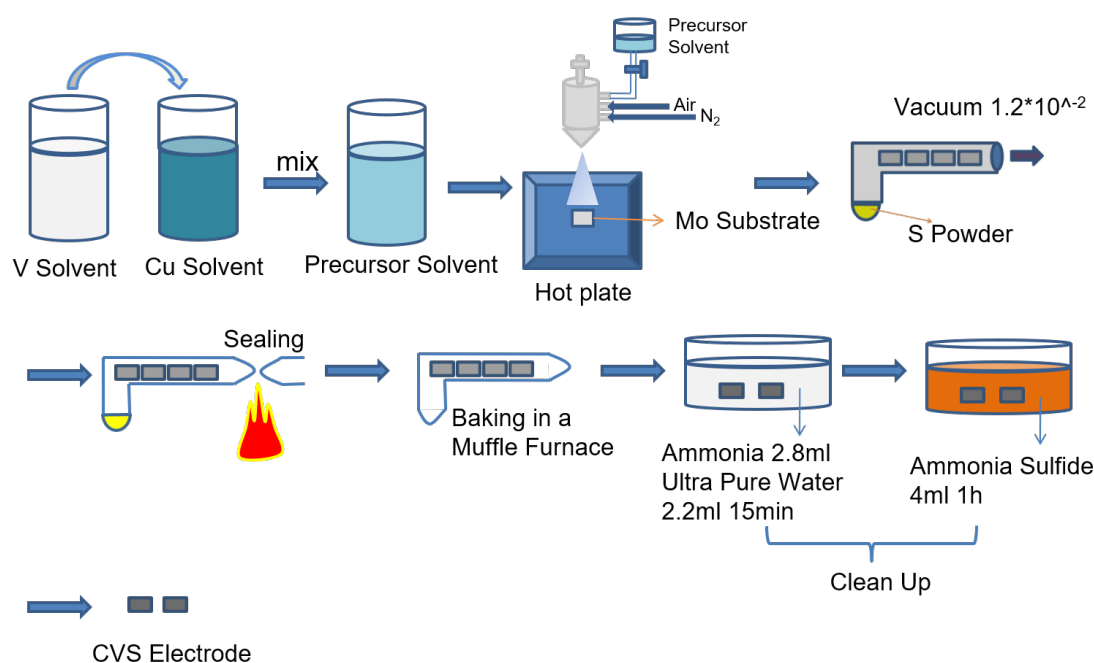
## 2. Experimental section

### 2.1 Chemicals

Unless otherwise stated, all of the chemicals used in the study were of analytical grade and used without further purification. All solutions were prepared by using ultra-pure water.  $\text{VO}(\text{acac})_2$ ,  $\text{Cu}(\text{NO}_3)_2\cdot 3\text{H}_2\text{O}$ ,  $\text{AgNO}_3$ ,  $\text{Ga}(\text{NO}_3)_3\cdot x\text{H}_2\text{O}$ , S powder,  $\text{InCl}_3\cdot 4\text{H}_2\text{O}$  and nitric acid of analytical grade were purchased from Wako Pure Chemical Industries, Ltd., Japan.  $\text{C}_2\text{H}_5\text{NS}$  of analytical grade was purchased from Tokyo Chemical Industry, Japan. Mo/SLG substrate was purchased from GEOMATEC Co. Ltd., Japan.

## 2.2 Fabrication of a $\text{Cu}_3\text{VS}_4$ photocathode

In this study, typically, 0.02 M  $\text{VO}(\text{acac})_2$  (99.9%) and 0.06 M  $\text{Cu}(\text{NO}_3)_2 \cdot 3\text{H}_2\text{O}$  (99.9%) were fully dissolved in ultra-pure water with stirring overnight and then the two solutions were mixed at a volume ratio of 1:1 to obtain the precursor solvent. The temperature of the reaction stage was controlled at 380 °C, and 2 mL of the precursor solvent was sprayed onto an Mo/SLG substrate (16 mm × 20 mm). The spraying time was controlled at 5 min. The precursor film was put into a glass tube together with 20 mg of sulfur (99.9%), evacuated to  $1.2 \times 10^{-2}$  Pa, and then heated at 600 °C for 10 min. After cleaning with ammonia aqueous solution (25%) and ammonium sulfide (99.9%), the CVS photocathode was obtained.



**Scheme 1.** Flow chart of  $\text{Cu}_3\text{VS}_4$  photocathode preparation.

## 2.3 Modification with n-type buffer layers

### 2.3.1 Surface modification with an n-type $\text{In}_2\text{S}_3$ layer

An n-type  $\text{In}_2\text{S}_3$  layer was formed by the chemical bath deposition method. During the process, 2.5 mmol of  $\text{InCl}_3$  (99.9%), 10 mmol of thioacetamide (99.9%) and 0.6 mL of acetic acid (99.9%) were added into 100 mL of ultrapure water and stirred until they were completely dissolved. The electrode was immersed in the aqueous solution, and the bath

was heated at 65 °C for 30 minutes. After that, the electrode was taken out, washed with ultrapure water, and then annealed at 100 °C for 20 minutes to obtain In<sub>2</sub>S<sub>3</sub>/CVS.

### **2.3.2 Surface modification with an n-type CdS layer**

An n-type CdS layer was formed by the chemical bath deposition method. 79.6 mL of ultrapure water, 12.5 mmol of Cd(CH<sub>3</sub>COO)<sub>2</sub>·2H<sub>2</sub>O (99.9 %), 220 mmol of SC(NH<sub>2</sub>)<sub>2</sub> (98 %) and 20.4 mL of NH<sub>3</sub> aqueous solution (25 %) were added to the beaker and the mixture was stirred until they were completely dissolved. The electrode was immersed in the aqueous solution, and the bath was heated at 65 °C for 9 minutes. After that, the electrode was taken out, washed with ultrapure water, and then annealed at 200 °C for 10 minutes to obtain CdS/CVS.

### **2.3.3 Surface modification with an n-type TiO<sub>x</sub> layer**

The precursor solution of TiO<sub>x</sub> was obtained by solving the tetrabutyl titanate (180 μL) in the mixture solvents of ethanol/isopropanol (5 mL:5 mL), then stirred for 5 min before adding 10 μL of concentrated hydrochloric acid (HCl). Then, the solution was stirred for 72 h at room temperature in a sealed vial. The TiO<sub>x</sub> film was prepared by spin-coating this solution onto the sample at a speed of 1000 rpm min<sup>-1</sup> for 1 min in with thermal annealing at 160 °C for 20 min in air [2].

## **2.4 Doping of Ag or Ga in CVS electrodes**

The Ag/(Ag + V) molar ratio was varied to control the different Ag amounts in the individual precursor solutions, while the total molar amounts of Ag and V were kept at 0.02M. The same conditions apply to Ga.

## **2.5 Characterization of catalysts**

The crystalline phases were characterized by using a powder X-ray diffraction (XRD) instrument (MiniFlex II, Rigaku Co.) with CuKα (λ = 1.5418 Å) radiation (cathode voltage: 30 kV, current: 15 mA). The absorption properties of an Au-In<sub>2</sub>S<sub>3</sub>/CBS electrode were measured using the diffuse reflection method with a UV-VIS spectrometer (UV-2600,

Shimadzu Co.) attached to an integral sphere at room temperature. X-ray photoelectron spectroscopy (XPS) measurements were performed by using a Kratos AXIS Nova spectrometer (Shimadzu Co.) with a monochromatic Al K $\alpha$  X-ray source. The binding energy was calibrated by taking the C1s peak of contaminant carbon as a reference at 284.6 eV. Raman spectroscopy measurements were performed with 532 nm excitation wavelength (NRS-5100, JASCO Co.).

## 2.6 Photoelectrochemical (PEC) measurement

The PEC performance of the CVS electrode was investigated in a three-electrode configuration by using a silver-silver chloride (Ag/AgCl) reference electrode and a Pt coil counter electrode. In order to avoid the influence of Pt<sup>2+</sup>, an H-type electrolytic cell is used, and the Nafion™ membrane is used for isolation. The electrolytes were 0.1 M Eu<sup>3+</sup>-containing aqueous solution, 0.1 M Na<sub>2</sub>SO<sub>4</sub> solution (pH = 6) or 0.1 M phosphate buffer solution (pH = 7). All electrolytes were stirred and purged with N<sub>2</sub> gas or O<sub>2</sub> gas for 30 min before PEC measurement. In the case of 0.1 M phosphate buffer solution (pH = 7), the measured potential vs. Ag/AgCl was converted to RHE by Nernst's equation ( $E_{RHE} = E_{Ag/AgCl} + 0.059 \text{ pH} + 0.197$ ). Linear sweep voltammetry and chronoamperometry measurements were carried out by an automatic polarization system (HSV-110, Hokuto Denko Co.) under visible light (420-800 nm) irradiation. The scan rate for the linear sweep voltammetry was 10 mV/s<sup>-1</sup>.

## 2.7 Analysis of products

The amount of H<sub>2</sub>O<sub>2</sub> was determined by a colorimetric method using PACKTEST (WAK-H<sub>2</sub>O<sub>2</sub>, KYORITSU CHEMICAL-CHECK Lab., Corp.) equipped with a digital PACKTEST spectrometer (ED723, GL Sciences Inc.).

# 3. Results and discussion

## 3.1 Ag doped Cu<sub>3</sub>VS<sub>4</sub> photocathode

The surface morphology of the Cu<sub>3</sub>VS<sub>4</sub> film was characterized and analyzed using field scanning electron microscopy (SEM), as shown in **Figure 3-2**. With the increase of



Ag doping content (mol%), the average particle size of the material increases, and when the doping content reaches 3%, the particles are larger and uniformly distributed. In general, an increase in particle size results in a decrease in charge recombination, thereby increasing the photocurrent density.

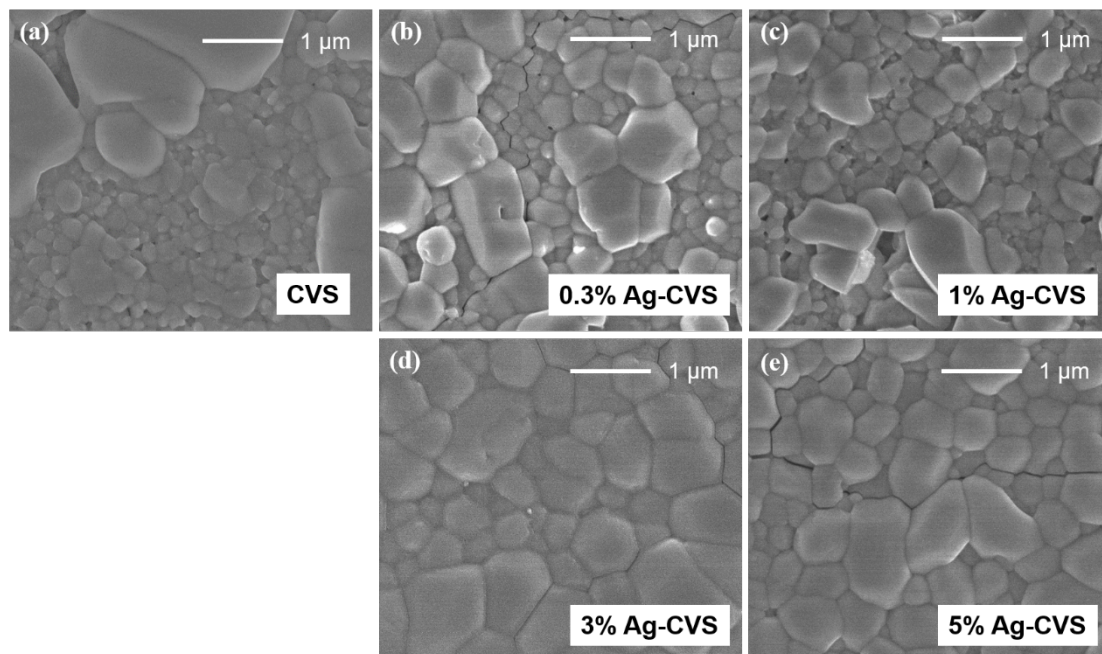


**Figure 3-2.** SEM photographs of (a) bare  $\text{Cu}_3\text{VS}_4$  electrodes; (b) 0.3% Ag-  $\text{Cu}_3\text{VS}_4$ ; (c) 1% Ag-  $\text{Cu}_3\text{VS}_4$ ; (d) 3% Ag-  $\text{Cu}_3\text{VS}_4$ ; (e) 5% Ag-  $\text{Cu}_3\text{VS}_4$ .

The crystal structure and phase composition of the film were characterized and analyzed by X-ray diffractometer (XRD) (**Figure 3-3**). The XRD pattern is shown in Figure 3-2. As can be seen from the figure, the XRD pattern of the  $\text{Cu}_3\text{VS}_4$  film has the typical diffraction peaks of  $\text{Cu}_3\text{VS}_4$  (JCPDS No. 11-0104) [9]. It can be found that the doping of Ag has little effect on the species of  $\text{Cu}_3\text{VS}_4$  electrode, since no extra peaks were found. Negligible variation in lattice parameter values of nanoparticles having Ag dopant above 3% compared to undoped sample might be due to migration of  $\text{Ag}^+$  ions from  $\text{Cu}_3\text{VS}_4$  lattice to its surface. Also, the large gap between the ionic radius of  $\text{Ag}^+$  (1Å) [10] and  $\text{Cu}^{1+}$  (0.6Å) [11] ions suggests that the Ag ions in lesser content can only fill the interstitial sites in the  $\text{Cu}_3\text{VS}_4$  lattice.

The main characteristic diffraction peaks with  $2\theta$  values of  $16.402^\circ$ ,  $28.586^\circ$ ,  $37.441^\circ$  and  $47.568^\circ$  were selected to analyze their full width at half-maximum (FWHM) (**Table 3-1**). In general, the smaller the FWHM value, the larger the particle size. These results

show that the crystal quality obtained with 3 mol% Ag is better than any other concentration.

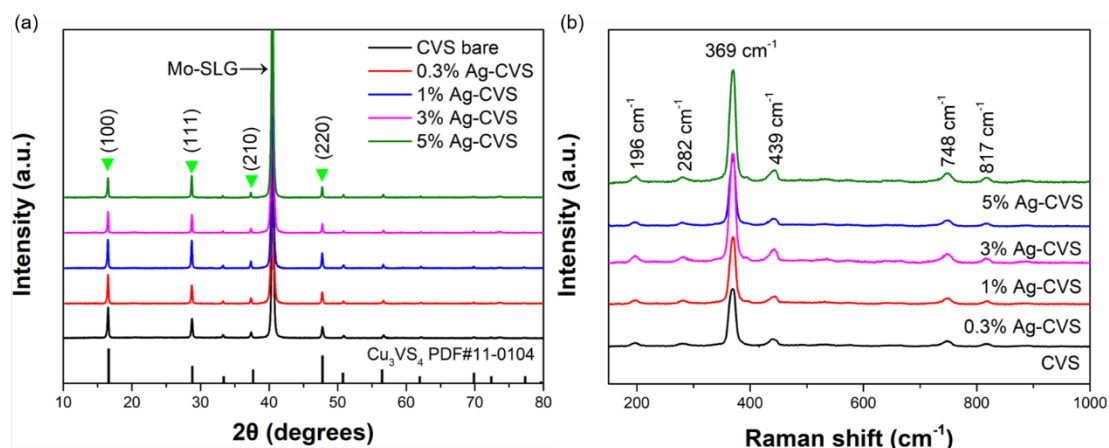


**Figure 3-3.** (a) XRD patterns of pure  $\text{Cu}_3\text{VS}_4$  and  $\text{Ag-Cu}_3\text{VS}_4$  with different Ag addition amounts. (b) Raman spectra of pure  $\text{Cu}_3\text{VS}_4$  and  $\text{Ag-Cu}_3\text{VS}_4$  with different Ag addition amounts.

**Table 3-1.** Full width at half-maximum (FWHM) of pure  $\text{Cu}_3\text{VS}_4$  and  $\text{Ag-Cu}_3\text{VS}_4$  with different Ag addition amounts.

		CVS	0.3% Ag-CVS	1% Ag-CVS	3% Ag-CVS	5% Ag-CVS
2-Theta	hkl	FWHM (2 $\theta$ )	FWHM (2 $\theta$ )	FWHM (2 $\theta$ )	FWHM (2 $\theta$ )	FWHM (2 $\theta$ )
16.402	<100>	0.209	0.186	0.187	0.18	0.178
28.586	<111>	0.211	0.203	0.203	0.166	0.175
37.441	<210>	0.207	0.19	0.193	0.152	0.162
47.568	<220>	0.224	0.223	0.219	0.178	0.184

CVS material is a direct allowed transition material. The optical band-gap is estimated via the Tauc relation:  $h\nu = \alpha(h\nu - E_g)^2$ , where  $\alpha$ ,  $h$  and  $\nu$  are the optical absorption coefficient, Planck's constant, and frequency, respectively. The linear variation behavior of  $(\alpha h\nu)^2$  versus  $(h\nu)$  designates a direct transition in CVS material. **Figure 3-4** illustrates the UV-VIS-NIR optical absorption spectroscopy and the corresponding  $(\alpha h\nu)^2$ -( $h\nu$ ) plots of CVS and Ag-CATS thin films. It can be seen that all films exhibit strong absorptions in the entire visible light regions, but the spectral response of Ag-CATS films were greatly increased due to the Ag incorporation. The band-gap of CVS and Ag-CATS thin films was found to be 1.51, 1.52, 1.52, 1.56 and 1.58 eV, respectively. It might be due to the increased particle size of the CVS material with the increased Ag doping amount.

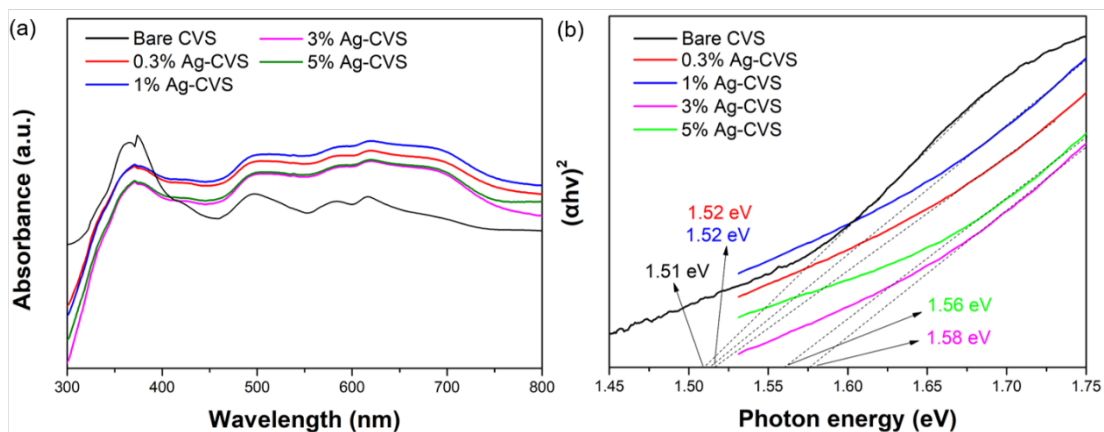


**Figure 3-4.** UV–VIS–NIR absorption spectra and (b)  $(\alpha h\nu)^2$  vs  $(h\nu)$  plots for different amount of Ag doped CVS films.

Electrochemical impedance spectroscopy (EIS) of the samples were performed in a phosphate buffer electrolyte (0.1 M, pH = 7) with visible light (420–800 nm, 100 mW/cm<sup>2</sup>) irradiation. The exchange of charge carriers between the catalyst and the electrolyte at the interface is generally called the charge transfer process. The smaller semicircle in the Nyquist diagram indicates better charge transfer kinetics. (**Figure 3-5**). Charge transfer resistance of the CVS electrode decreased significantly with Ag doping, with 3% Ag-CVS being the best. This result is consistent with our previous conclusion that 3% Ag-CVS has the highest crystallinity. A photocurrent density increase can be observed during the PEC process as a result of the increased charge transfer rate.

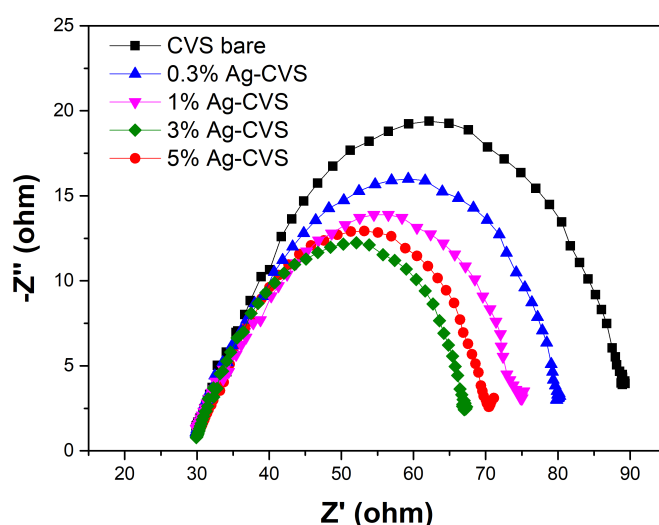


**Figure 3-5.** Nyquist plots of pure  $\text{Cu}_3\text{VS}_4$  and Ag– $\text{Cu}_3\text{VS}_4$  with different Ag addition amounts. (a) bare  $\text{Cu}_3\text{VS}_4$  electrodes; (b) 0.3% Ag– $\text{Cu}_3\text{VS}_4$ ; (c) 1% Ag– $\text{Cu}_3\text{VS}_4$ ; (d) 3% Ag– $\text{Cu}_3\text{VS}_4$ ; (e) 5% Ag– $\text{Cu}_3\text{VS}_4$ .

The activities of the as-prepared Ag-doping CVS electrodes were compared by measuring the photocurrents. The oxygen reduction reaction was carried out in an O<sub>2</sub>-saturated phosphate buffer electrolyte (0.1 M, pH = 7) with visible light (420–800 nm, 100 mW/cm<sup>2</sup>) irradiation under a potentiostatic condition at +0.7 V vs. V<sub>RHE</sub> (**Figure 3-6**). First of all, it can be seen that the photocurrent density is generally improved after Ag doping compared with the bare CVS electrode. Although the photocurrent density of 0.3%Ag-Cu<sub>3</sub>VS<sub>4</sub> started out at the highest, a clear decreasing trend was seen after half an hour. While electrodes with a higher amount of Ag-doped CVS electrodes were more stable, which may be related to particle size. The electrodes with larger particles are more corrosion-resistant. A final optimized amount of Ag doping is 3%, which could produce H<sub>2</sub>O<sub>2</sub> at a rate of 4.04 mg·L<sup>-1</sup>·h<sup>-1</sup>·cm<sup>-1</sup> with a Faraday efficiency of 95.6%.

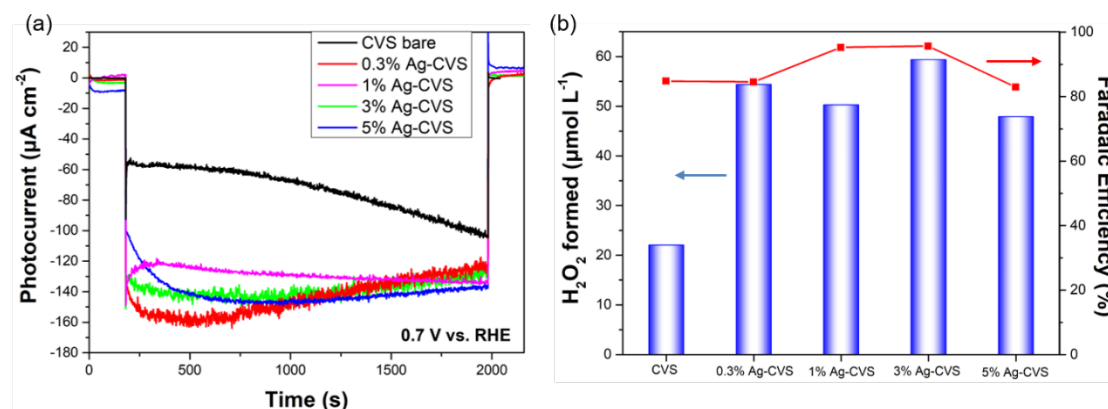


**Figure 3-6.** (a) Time courses of the photocurrent of Ag-doping Cu<sub>3</sub>VS<sub>4</sub> electrodes in an O<sub>2</sub>-saturated phosphate buffer electrolyte (0.1 M, pH = 7) with visible light (420–800 nm, 100 mW/cm<sup>2</sup>) irradiation under a potentiostatic condition at +0.7 V vs. V<sub>RHE</sub>. (b) Amounts of generated H<sub>2</sub>O<sub>2</sub> by Ag-doping Cu<sub>3</sub>VS<sub>4</sub> electrodes with visible light (420-800 nm, 100 mW/cm<sup>2</sup>) irradiation for 0.5 h and corresponding Faraday efficiencies.

### 3.2 Ga doped Cu<sub>3</sub>VS<sub>4</sub> photocathode

The doping of Ag can effectively increase the particle size of the CVS electrode and greatly improve the photocurrent density. However, Ag ions does not replace Cu<sup>1+</sup> ions as expected, which results in a change in the band structure. As the CVS electrode was doped with Ga, its valence band maximum was changed to match the modified n-type semiconductor and further separate charge and hole. From the ionic radius, in the CVS electrode, the ionic radius of Cu<sup>1+</sup> is 0.6 Å, the ionic radius of Ag<sup>1+</sup> is 1 Å, and the ionic

radius of  $\text{Ga}^{3+}$  is  $0.47 \text{ \AA}$  [12]. It can be inferred that Ga ions are easier to replace  $\text{Cu}^{1+}$  ions than Ag ions.

The surface morphology of the  $\text{Cu}_3\text{VS}_4$  film was characterized and analyzed using field scanning electron microscopy (SEM), as shown in **Figure 3-7**. The average particle size of the material increases with Ga doping, but the effect is not as obvious as that of Ag doping.

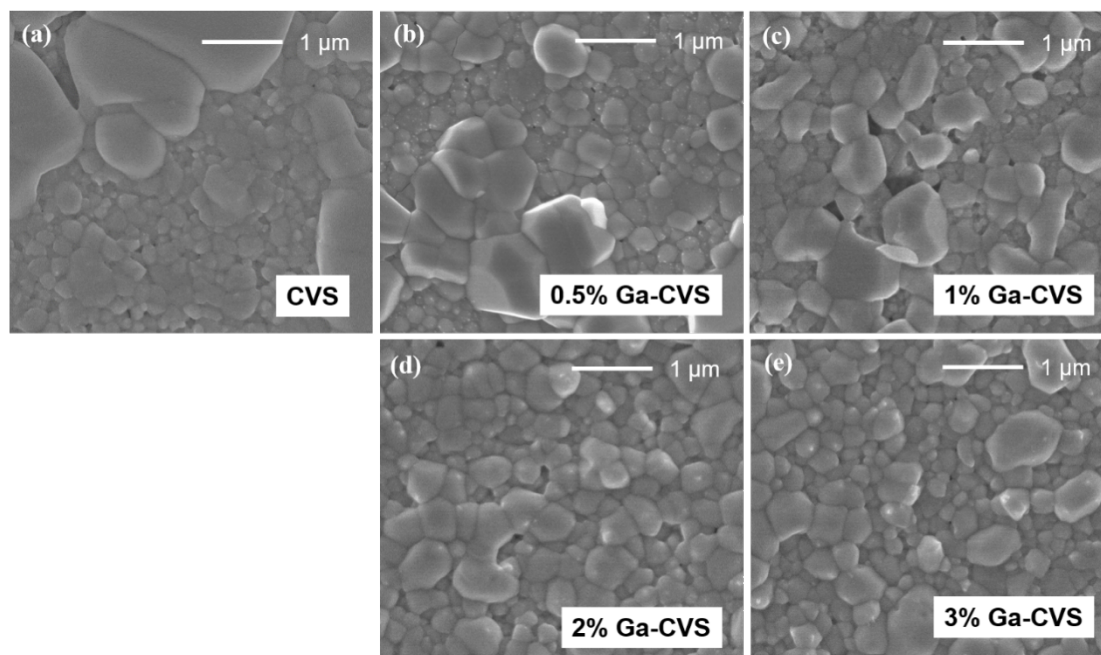


**Figure 3-7.** SEM photographs of (a) bare  $\text{Cu}_3\text{VS}_4$  electrodes; (b) 0.5% Ga- $\text{Cu}_3\text{VS}_4$ ; (c) 1% Ga -  $\text{Cu}_3\text{VS}_4$ ; (d) 2% Ga- $\text{Cu}_3\text{VS}_4$ ; (e) 3% Ga -  $\text{Cu}_3\text{VS}_4$ .

The crystal structure and phase composition of the film were characterized and analyzed by X-ray diffractometer (XRD) (**Figure 3-8a**). The XRD pattern is shown in Figure 3-2. As can be seen from the figure, the XRD pattern of the  $\text{Cu}_3\text{VS}_4$  film has the typical diffraction peaks of  $\text{Cu}_3\text{VS}_4$  (JCPDS No. 11-0104). No extra peaks were observed when Ga was doped in  $\text{Cu}_3\text{VS}_4$  electrodes, indicating that Ga doping does not significantly impact the species. It could be noticed that the diffraction peak positions of the Ga-doped  $\text{Cu}_3\text{VS}_4$  displayed a moderate shift towards lower  $2\theta$  values as the Ga doping content increased. This distinctly implies lattice compression consistent with the smaller ionic radius of  $\text{Ga}^{3+}$  ( $0.47 \text{ \AA}$ ) compared to that of  $\text{Cu}^{1+}$  ( $0.6 \text{ \AA}$ ), affirming the incorporation of Ga ions as a substituent in the prepared  $\text{Cu}_3\text{VS}_4$ .

In order to further explain what form of Ga exists in  $\text{Cu}_3\text{VS}_4$ , we conducted Raman tests on  $\text{Cu}_3\text{VS}_4$  electrodes with different Ga doping amounts (**Figure 3-8c**). According to the Raman spectrum of  $\text{Cu}_3\text{VS}_4$ , peaks can be observed at  $196\text{ cm}^{-1}$ ,  $282\text{ cm}^{-1}$ ,  $369\text{ cm}^{-1}$ ,  $392\text{ cm}^{-1}$ ,  $439\text{ cm}^{-1}$ ,  $748\text{ cm}^{-1}$  and  $817\text{ cm}^{-1}$ , which is in accordance with the earlier studies [13]. As the amount of Ga doping increases, the peak at  $392\text{ cm}^{-1}$  becomes more prominent, indicating the formation of Ga-S bonds [14].

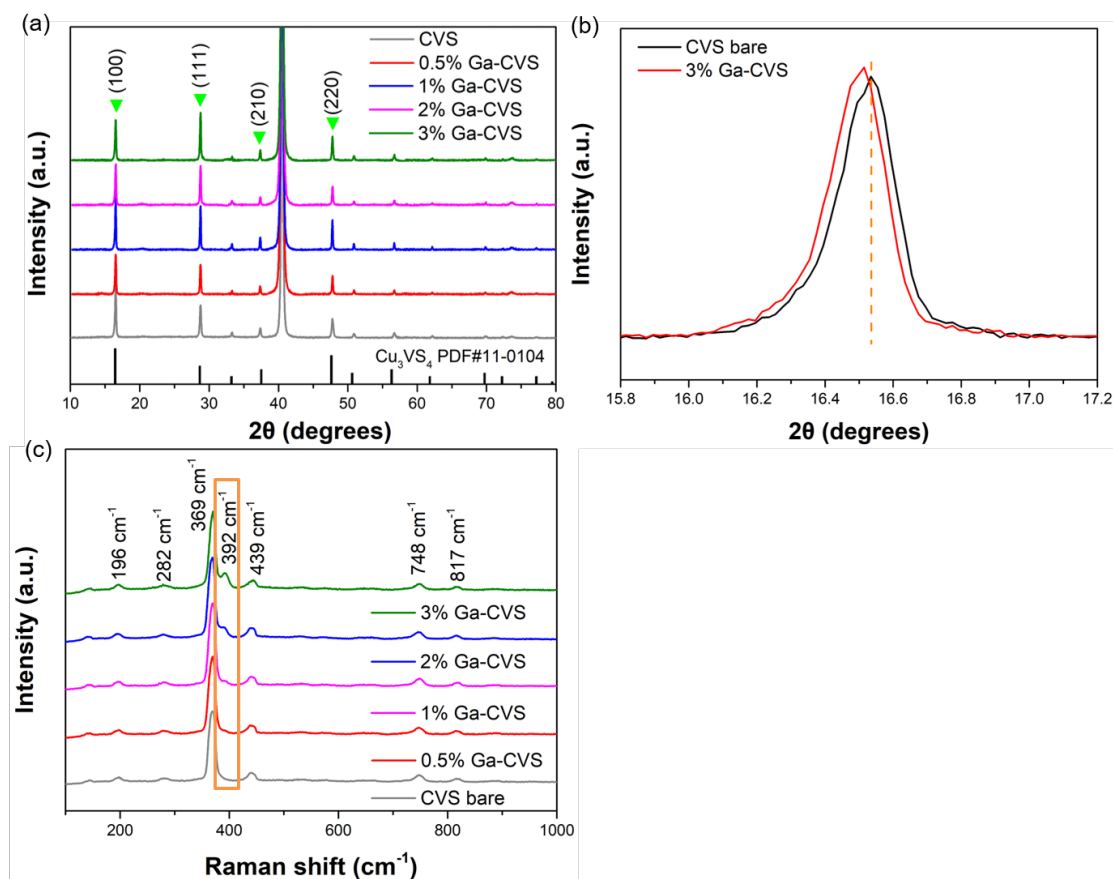


**Figure 3-8.** (a) XRD patterns of pure  $\text{Cu}_3\text{VS}_4$  and  $\text{Ga-Cu}_3\text{VS}_4$  with different Ga addition amounts. (b) A partial enlarged view of the XRD pattern. (c) Raman spectra of pure  $\text{Cu}_3\text{VS}_4$  and  $\text{Ga-Cu}_3\text{VS}_4$  with different Ga addition amounts.

As illustrated in **Figure 3-9**, the UV-VIS-NIR optical absorption spectroscopy and the corresponding  $(\alpha h\nu)^2 - (h\nu)$  plots of CVS and Ga-CVS thin films are demonstrated. Doping with Ga increases absorbance significantly, but excessive doping decreases it. In CVS, the valence band maximum is formed by the Cu 3d + S 3p hybrid orbital and the conduction band minimum is formed by the V 3d + S 3p hybrid orbital [15]. As reported in previous reports, replacing Cu with Ga leads to increased VBM without affecting CBM,



thereby increasing the bandgap. Furthermore, VBM increased with increasing Ga doping in the CVS electrode.

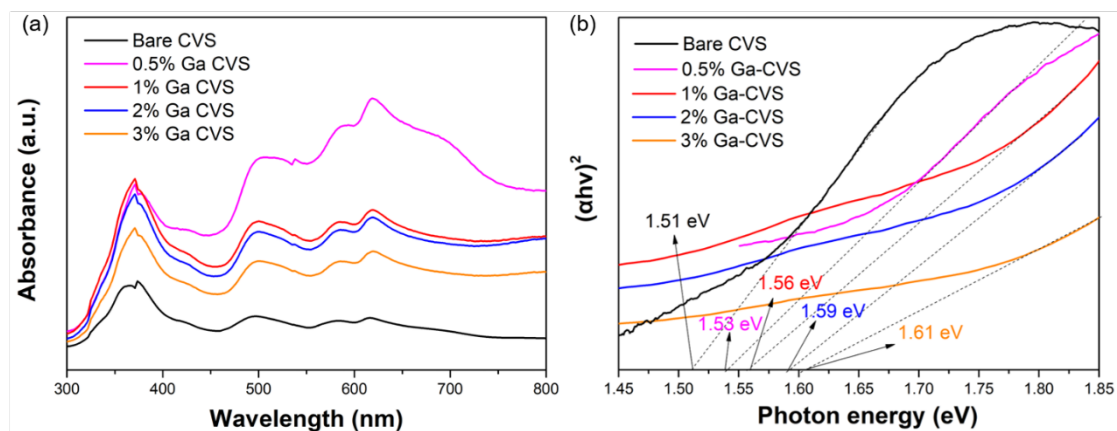


**Figure 3-9.** UV–VIS–NIR absorption spectra and (b)  $(\alpha h\nu)^2$  versus  $h\nu$  plots for CTS and x-CATS films.

Electrochemical impedance spectroscopy (EIS) of the samples were performed in a phosphate buffer electrolyte (0.1 M, pH = 7) with visible light (420–800 nm, 100 mW/cm<sup>2</sup>) irradiation. The exchange of charge carriers between the catalyst and the electrolyte at the interface is generally called the charge transfer process. The smaller semicircle in the Nyquist diagram indicates better charge transfer kinetics. (**Figure 3-10**). Ga-doped CVS electrodes have lower charge transfer resistance than the bare CVS electrode, with 1% Ga-CVS exhibiting the lowest resistance. The increase in the charge transfer rate during the PEC process can be manifested as an increase in the photocurrent density.

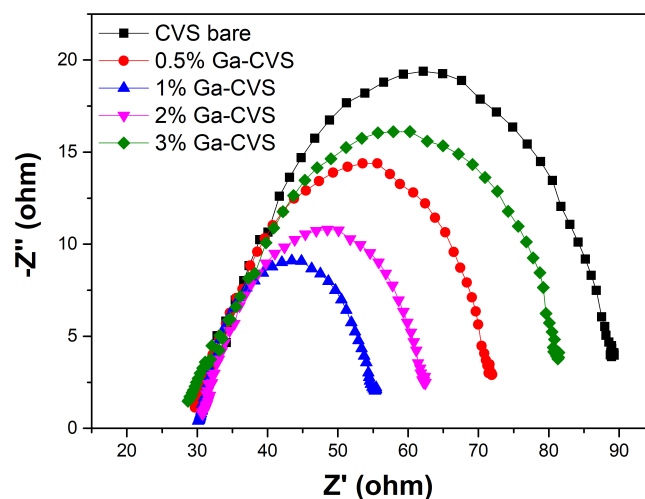


**Figure 3-10.** Nyquist plots of pure  $\text{Cu}_3\text{VS}_4$  and Ga- $\text{Cu}_3\text{VS}_4$  with different Ga addition amounts. (a) bare  $\text{Cu}_3\text{VS}_4$  electrode; (b) 0.5% Ga- $\text{Cu}_3\text{VS}_4$ ; (c) 1% Ga- $\text{Cu}_3\text{VS}_4$ ; (d) 2% Ga- $\text{Cu}_3\text{VS}_4$ ; (e) 3% Ga- $\text{Cu}_3\text{VS}_4$ .

The activities of the as-prepared Ga-doping CVS electrodes were compared by measuring the photocurrents. The oxygen reduction reaction was carried out in an O<sub>2</sub>-saturated phosphate buffer electrolyte (0.1 M, pH = 7) with visible light (420–800 nm, 100 mW/cm<sup>2</sup>) irradiation under a potentiostatic condition at +0.7 V vs. V<sub>RHE</sub> (**Figure 3-11**). First of all, it can be seen that the photocurrent density is generally improved after Ga doping compared with the bare CVS electrode. It can be found that the photocurrent density of 0.5% Ga-Cu<sub>3</sub>VS<sub>4</sub> started to be the highest, but a clear decreasing trend was seen after half an hour. However, the photocurrent density decreased for electrodes with higher Ga concentrations in CVS electrodes. The optimized amount of Ga doping was determined to be 0.5%, which could produce H<sub>2</sub>O<sub>2</sub> at a rate of 7.52 mg·L<sup>-1</sup>·h<sup>-1</sup>·cm<sup>-1</sup> with an excellent Faraday efficiency of 99%.

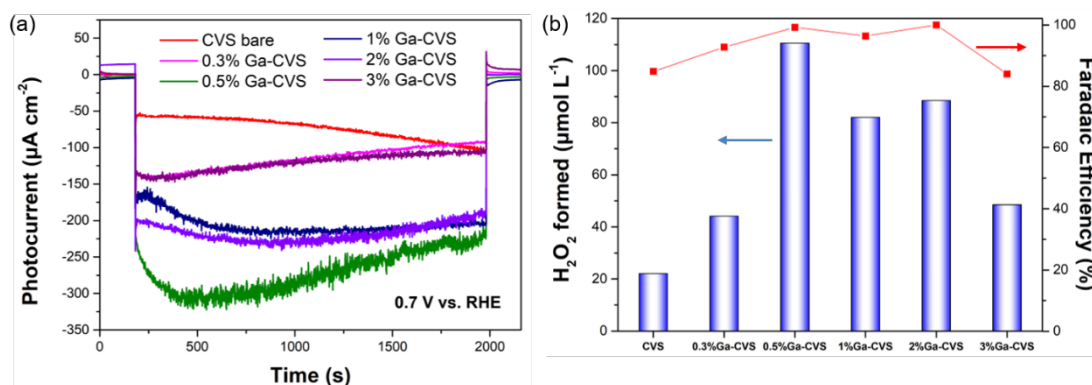


**Figure 3-11.** (a) Time courses of the photocurrent of Ga-doping Cu<sub>3</sub>VS<sub>4</sub> electrodes in an O<sub>2</sub>-saturated phosphate buffer electrolyte (0.1 M, pH = 7) with visible light (420–800 nm, 100 mW/cm<sup>2</sup>) irradiation under a potentiostatic condition at +0.7 V vs. V<sub>RHE</sub>. (b) Amounts of generated H<sub>2</sub>O<sub>2</sub> by Ga-doping Cu<sub>3</sub>VS<sub>4</sub> electrodes with visible light (420-800 nm, 100 mW/cm<sup>2</sup>) irradiation for 0.5 h and corresponding Faraday efficiencies.

### 3.3 Ga, Ag co-doped Cu<sub>3</sub>VS<sub>4</sub> photocathode

Even though Ga doping greatly enhances photocurrent density, photocurrent attenuation is also apparent. It has been reported that the co-doping of the two metals may produce a synergistic effect, thereby enhancing the charge separation efficiency and increasing the photocurrent density. Previous work has shown that Ag doping can effectively increase the particle size of CVS, thereby greatly improving the stability of the photocathode; Ga doping can replace Cu atoms to a certain extent, form lattice defects and introduce impurity energy levels, which effectively increases charge separation



efficiency. As a result, we attempted to improve CVS electrode photocurrent density and stability through Ag and Ga co-doping.

The activities of the as-prepared Ga, Ag-doping CVS electrodes were compared by measuring the photocurrents. The oxygen reduction reaction was carried out in an O<sub>2</sub>-saturated phosphate buffer electrolyte (0.1 M, pH = 7) with visible light (420–800 nm, 100 mW/cm<sup>2</sup>) irradiation under a potentiostatic condition at +0.7 V vs. V<sub>RHE</sub> (**Figure 3-12**). According to the previous optimization results, the doping amount of Ag was fixed at 3%, and the doping amount of Ga was regulated. Unfortunately, the photocurrent density was not as high as that of the Ga-doped CVS electrode (0.5% Ga-CVS), and the hydrogen peroxide generation and Faradaic efficiency were also reduced.

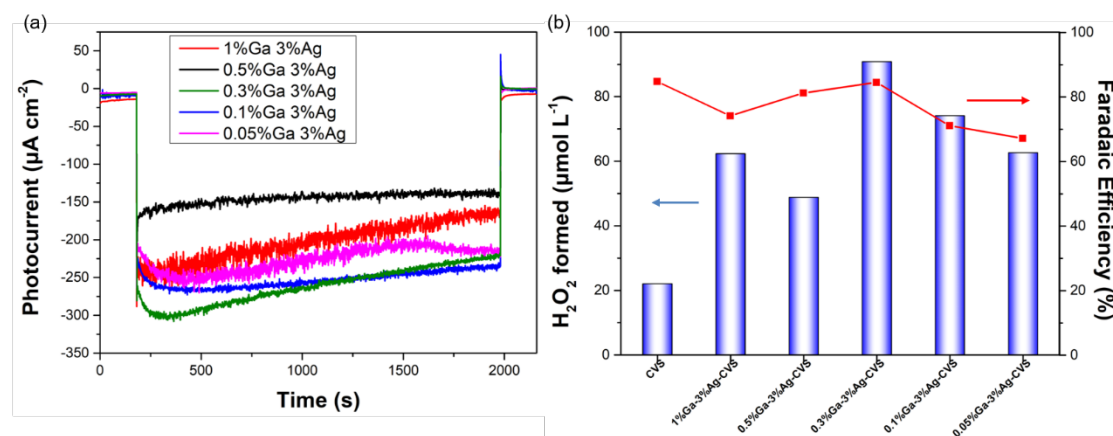


**Figure 3-12.** (a) Time courses of the photocurrent of Ga-doping Cu<sub>3</sub>VS<sub>4</sub> electrodes in an O<sub>2</sub>-saturated phosphate buffer electrolyte (0.1 M, pH = 7) with visible light (420–800 nm, 100 mW/cm<sup>2</sup>) irradiation under a potentiostatic condition at +0.7 V vs. V<sub>RHE</sub>. (b) Amounts of generated H<sub>2</sub>O<sub>2</sub> by Ga-doping Cu<sub>3</sub>VS<sub>4</sub> electrodes with visible light (420-800 nm, 100 mW/cm<sup>2</sup>) irradiation for 0.5 h and corresponding Faraday efficiencies.

As displayed in **Figure 3-13a**, main peaks of 956.6 eV, 952.9 eV, 936.4 eV, 933.0 eV were found in Cu 2p spectra. The double peaks of 956.6 eV and 936.4 eV were assigned to the Cu<sup>+</sup>, while the peaks of 952.9 eV and 933.0 eV were assigned to the Cu<sup>2+</sup>. In V 2p spectra (**Figure 3-13b**), main peaks of 514.5 eV and 522.0 eV were attributed to typical values of V 2P<sub>1/2</sub> and V 2P<sub>3/2</sub>, respectively. By comparing this value with the one reported in the XPS database it corresponds to the vanadium oxidation state +3 [16]. This result is surprising considering that the XRD data show Cu<sub>3</sub>VS<sub>4</sub> as the only phase, where vanadium is present as V<sup>+5</sup>. It may be due to the fact that peak positions relative to

V(IV)-S and V(III)-S seem to shift towards lower binding energies than those in oxides; similar results were found by Buonsanti et. al [9]. In **Figure 3-13c**, the 2p core of Ga split into  $2p_{3/2}$  (1117.9 eV), which were consistent with the values for  $\text{Ga}^{3+}$  [16-18]. It can be observed from **Figure 3-13d** that Ag 3d signal was composed of two peaks at 368.6 eV (Ag  $3d_{5/2}$ ) and 374.6 eV (Ag  $3d_{3/2}$ ), which were consistent with  $\text{Ag}^+$  [19]. The S 2p XPS spectrum in **Figure 3-13e** contains the peaks of two kinds of sulfur, one of which is located at 161.5 eV and 162.7 eV, matching with S-Cu  $2p_{3/2}$  and S-Cu  $2p_{1/2}$  respectively, and belong to crystalline  $\text{Cu}_3\text{VS}_4$  [20]. The other peak corresponds to the Ga-S bond of sulphate species, located at 163.8 eV and 165.1 eV, which represents the chemical anchoring of CVS towards sulfur.

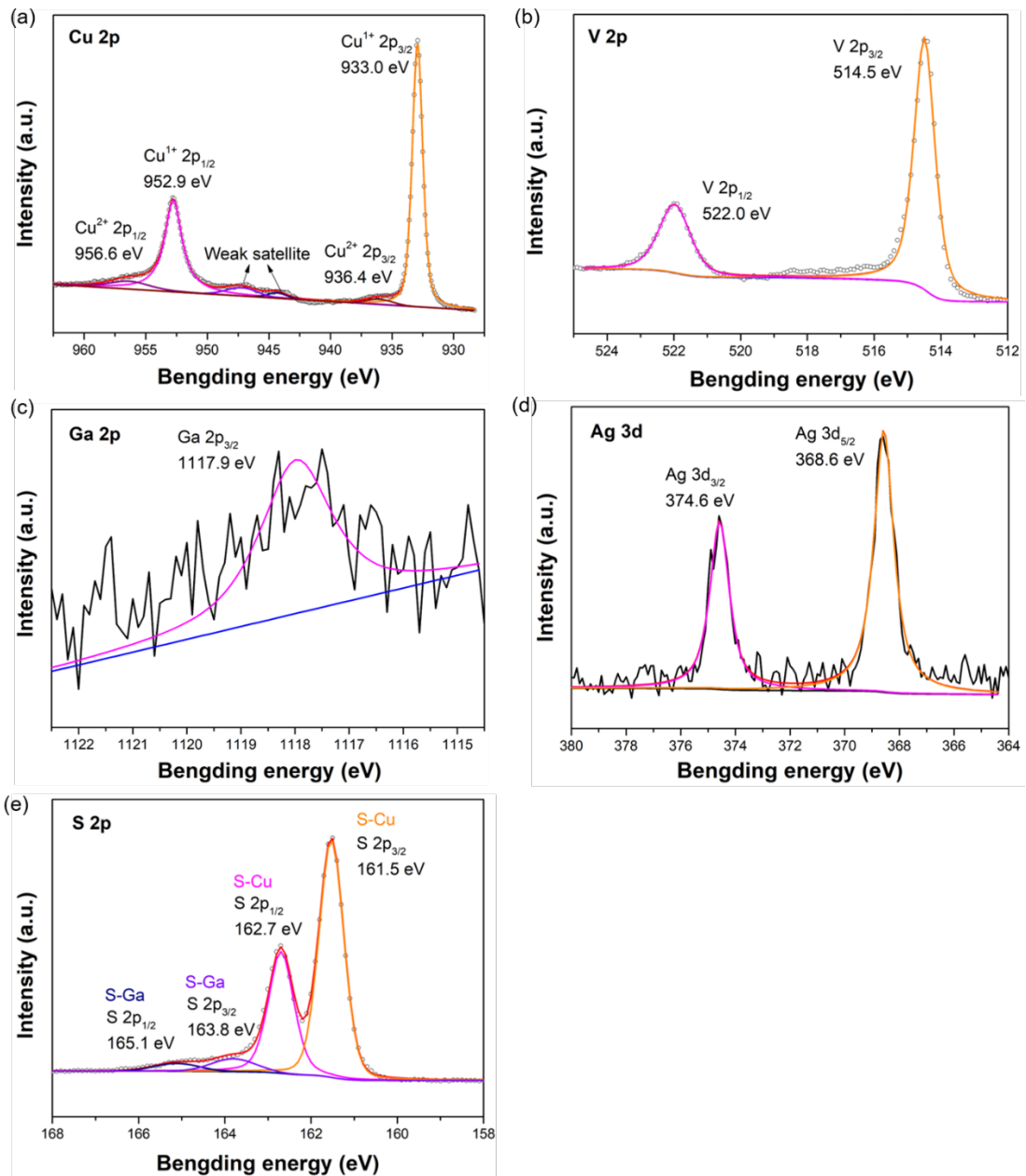


**Figure 3-13.** XPS spectra of Ag, Ga-doped  $\text{Cu}_3\text{VS}_4$  electrode. XPS spectra of Cu 2p (a), V 2p (b), Ga 2p (c), Ag 3d (d) and S 2p (e).

### 3.4 Sulfurization time and temperature optimization

The photocurrent density has not yet reached the expected value despite the optimization of Ag and Ga doping. We carried out TEM observation on the cross-section of Ag, Ga co-doped CVS photocathode (**Figure 3-14**). Voids and gaps were found at the junction of the CVS material and the Mo substrate, which may decrease the charge transfer rate. Additionally, Mo substrate was partially sulfided to form  $\text{MoS}_2$  layers, which

may also decrease charge transfer efficiency, resulting in reduced photocurrent density.

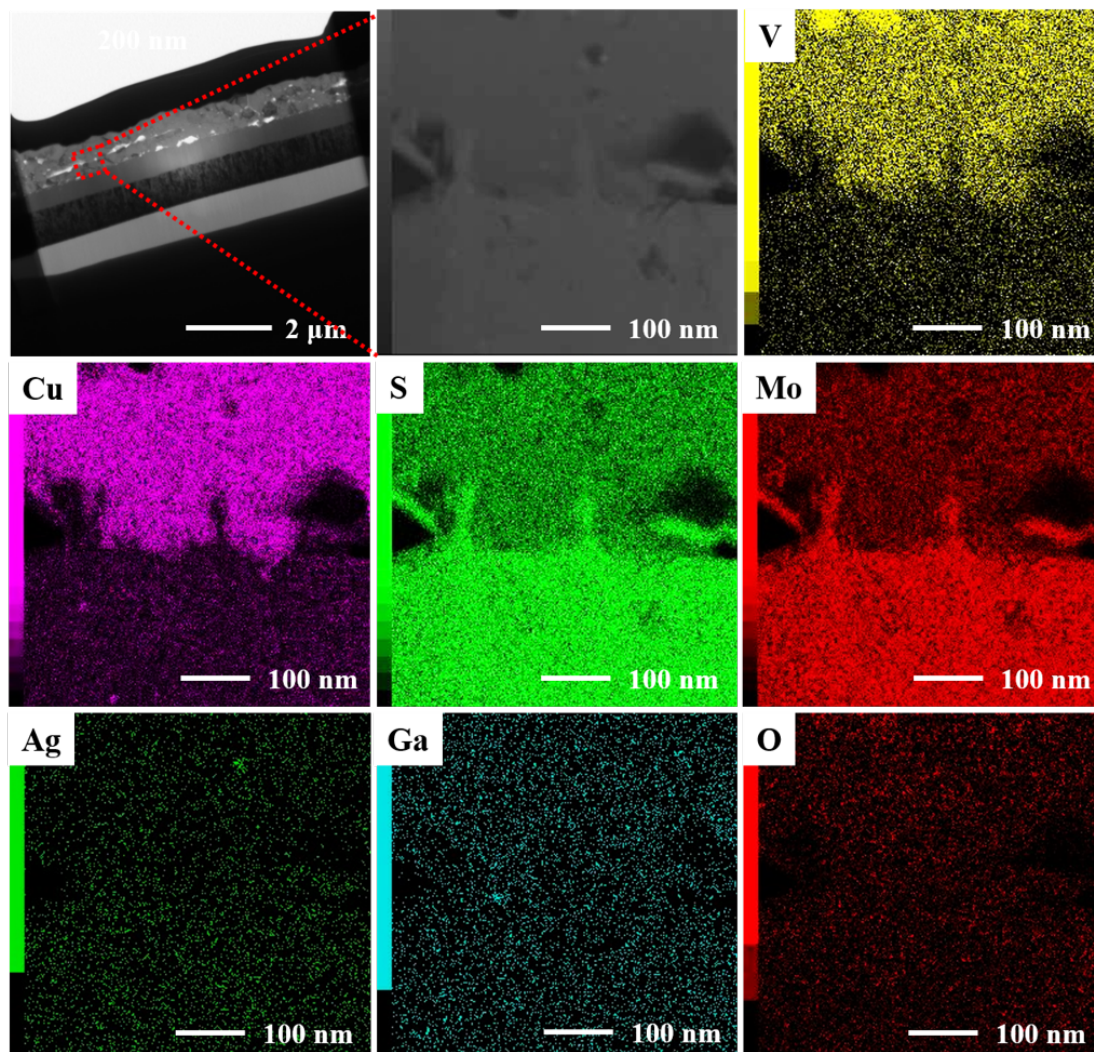


**Figure 3-14.** Energy dispersive spectroscopy on the transmission electron microscope (EDS-TEM). EDS map showing detection of Cu (purple), V (orange), S (green), Mo (red).

In order to reduce the thickness of the MoS<sub>2</sub> layer while maintaining good crystallinity and large particle size, we further optimized the sulfurization temperature and time. From the top and cross-sectional view images of SEM (**Figure 3-15**), it can be found that with the increase of sulfurization time, the particle size increases, but at the same time, the thickness of the MoS<sub>2</sub> layer also increases. The same rule applies to sulfurization temperature.

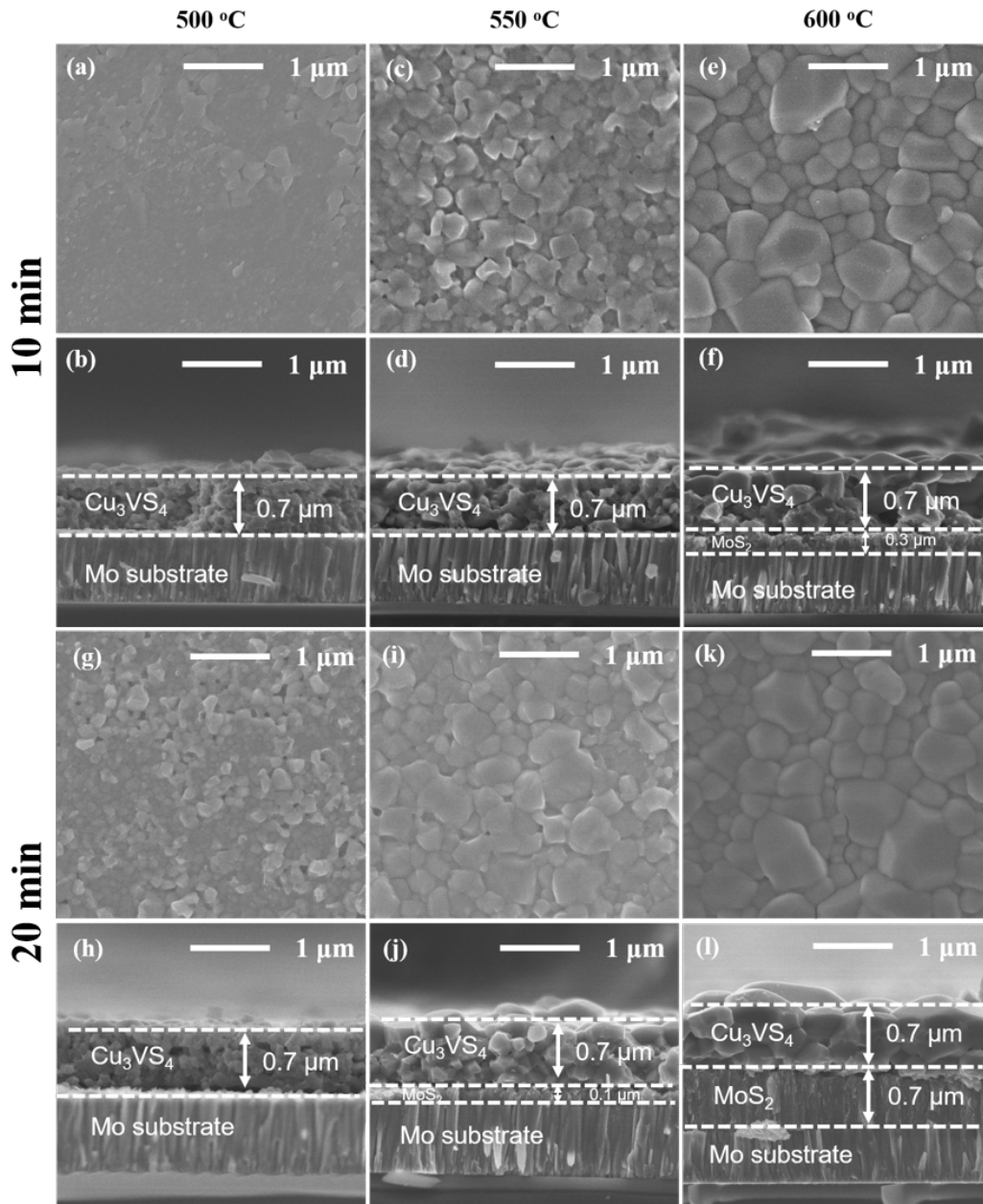


**Figure 3-15.** SEM photographs of 0.5% Ga-Cu<sub>3</sub>VS<sub>4</sub> electrodes prepared under different sulfurization time and temperature.

Linear scanning voltammograms (LSV) were used to evaluate the photoelectrochemical (PEC) performance of 0.5% Ga-Cu<sub>3</sub>VS<sub>4</sub> electrodes prepared at different sulfurization temperatures and times (**Figure 3-16a**). In particular, the CVS electrode with the largest MoS<sub>2</sub> layer thickness (0.7 μm) showed a high dark current density after heating at 600 °C for 20 minutes. Similar to our previous guess, this may be due to the poor conductivity of MoS<sub>2</sub>, which makes it difficult for the charge to be rapidly delivered to the Mo substrate. Finally, the sulfurization time and temperature were



optimized to 600 °C and 10 min, at which point the photocurrent density was the largest under a bias of 0.7 V<sub>RHE</sub>. This result was further confirmed by the relevant CA tests (Figure 3-16b) and the corresponding hydrogen peroxide generated and Faradaic efficiencies (Figure 3-16c).

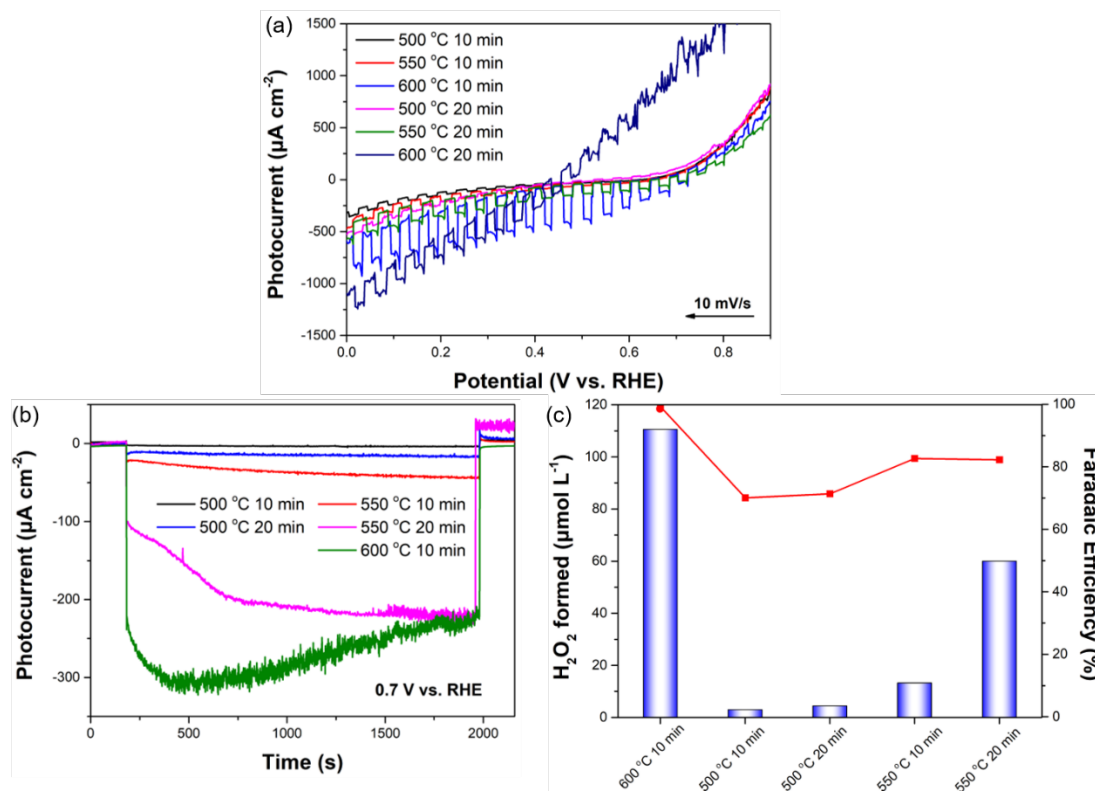


**Figure 3-16.** (a) Linear sweep voltammograms of 0.5%Ga-Cu<sub>3</sub>VS<sub>4</sub> electrodes in O<sub>2</sub>-bubbling phosphate buffer electrolyte (0.1 M, pH = 7) under chopped illumination from visible light (420-800 nm, 100 mW/cm<sup>2</sup>) irradiation. (b) Time courses of the photocurrent of 0.5%Ga-doping Cu<sub>3</sub>VS<sub>4</sub> electrodes in an O<sub>2</sub>-saturated phosphate buffer electrolyte (0.1 M, pH = 7) with visible light (420–800 nm, 100 mW/cm<sup>2</sup>) irradiation under a potentiostatic condition at +0.7 V vs. V<sub>RHE</sub>. (c) Amounts of generated H<sub>2</sub>O<sub>2</sub> by 0.5%Ga-doping Cu<sub>3</sub>VS<sub>4</sub> electrodes with visible light (420-800 nm, 100 mW/cm<sup>2</sup>) irradiation for 0.5 h and corresponding Faraday efficiencies.

### 3.5 The modification of n-type semiconductors

To improve the charge separation efficiency of the photocathode, the 0.5% Ga-doped CVS was further modified using several common n-type semiconductors. The In<sub>2</sub>S<sub>3</sub> and CdS layers were prepared by the chemical bath method, and the TiO<sub>x</sub> layer was prepared by a spin coating method. The specific preparation steps are shown in the experimental part.

Under a bias of  $0.7 V_{RHE}$ , the n-type semiconductor  $In_2S_3$  modification reduced dark current, but also photocurrent density (**Figure 3-17**). As the bias became more negative, the density of the photocurrent increased. Generally, the decrease in dark current is due to a reduction of photo-corrosion, meaning that the  $In_2S_3$  layer also serves as a protective layer for CVS electrodes. The current-time curves of the  $In_2S_3/ CVS$  photocathode were performed at bias voltages of  $0.7 V_{RHE}$  and  $0.3 V_{RHE}$ , respectively. Under the bias of  $0.7 V_{RHE}$ , the photocurrent was very low and no hydrogen peroxide generation was detected; Under the bias of  $0.3 V_{RHE}$ , the photocurrent density was about  $400 \mu A cm^{-2}$ , but this was accompanied by the rapid decay of the photocurrent and a hydrogen peroxide generation rate of  $1.62 mg \cdot L^{-1} \cdot h^{-1} \cdot cm^{-1}$ , corresponding to a Faraday efficiency of 17%.

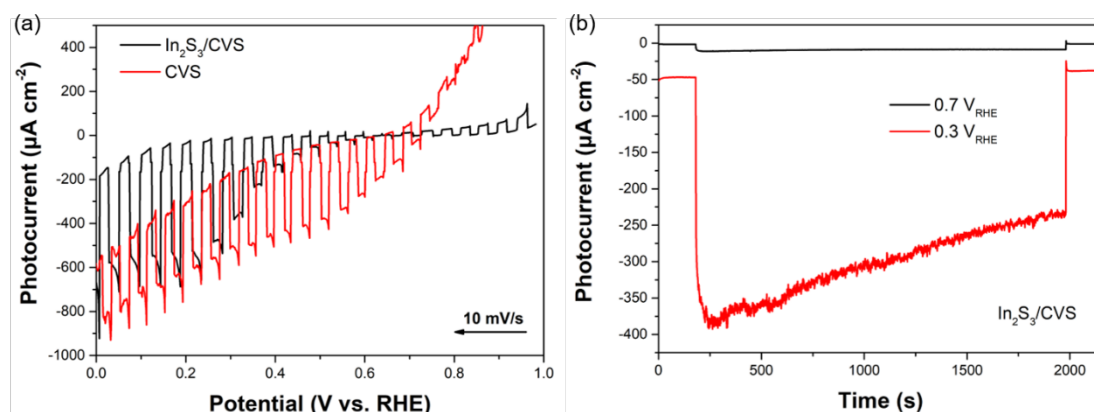


**Figure 3-17.** (a) Linear sweep voltammograms of 0.5% Ga- $Cu_3VS_4$  and  $In_2S_3$  modified 0.5% Ga-CVS electrodes in  $O_2$ -bubbling phosphate buffer electrolyte (0.1 M, pH = 7) under chopped illumination from visible light (420-800 nm,  $100 mW/cm^2$ ) irradiation. (b) Time courses of the photocurrent of  $In_2S_3/ CVS$  electrodes in an  $O_2$ -saturated phosphate buffer electrolyte (0.1 M, pH = 7) with visible light (420–800 nm,  $100 mW/cm^2$ ) irradiation under the potentiostatic conditions at  $+0.7 V$  and  $+0.3 V$  vs.  $V_{RHE}$ , respectively.

Interestingly, when the CdS layer is used for modification, the CdS/ CVS electrode shows n-type semiconductor properties at a high applied bias ( $> 0.6 V_{RHE}$ ) (**Figure 3-18**). Similar to the  $In_2S_3$  modification, a significantly lower dark current as well as photocurrent density was found after the CdS modification. In addition, onset voltage is also reduced to  $0.5 V_{RHE}$  relative to the CVS electrode. CA tests were conducted under the bias of 0.7 and  $0.3 V_{RHE}$  for CdS/ CVS photocathodes, respectively. Under the bias of  $0.7 V_{RHE}$ , the photocurrent showed the signature of an n-type semiconductor with no detectable hydrogen peroxide production; under the bias of  $0.3 V_{RHE}$ , the photocurrent density was approximately  $400 \mu A cm^{-2}$  but was accompanied by the rapid decay of the photocurrent

and a hydrogen peroxide production rate of  $1.62 \text{ mg}\cdot\text{L}^{-1}\cdot\text{h}^{-1}\cdot\text{cm}^{-1}$ , corresponding to a Faraday efficiency of 64%.

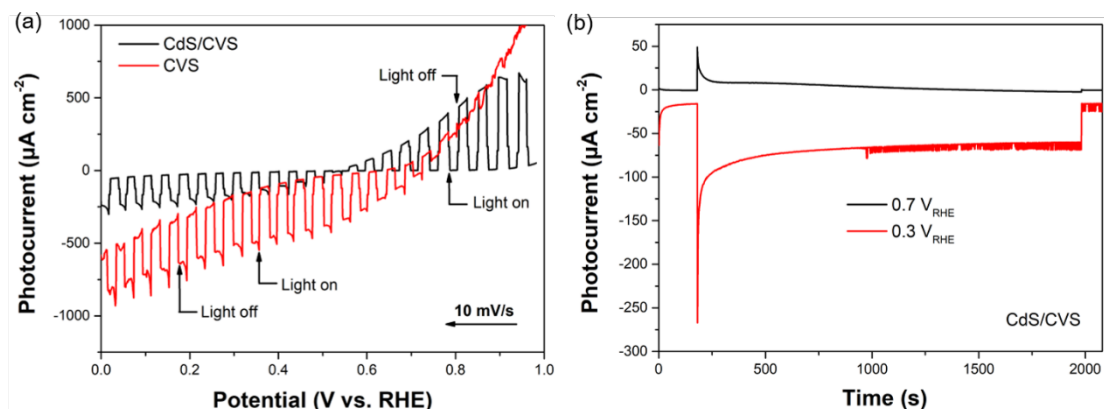


**Figure 3-18.** (a) Linear sweep voltammograms of 0.5%Ga-Cu<sub>3</sub>VS<sub>4</sub> and CdS modified 0.5%Ga-CVS electrodes in O<sub>2</sub>-bubbling phosphate buffer electrolyte (0.1 M, pH = 7) under chopped illumination from visible light (420-800 nm, 100 mW/cm<sup>2</sup>) irradiation. (b) Time courses of the photocurrent of CdS/CVS electrodes in an O<sub>2</sub>-saturated phosphate buffer electrolyte (0.1 M, pH = 7) with visible light (420–800 nm, 100 mW/cm<sup>2</sup>) irradiation under the potentiostatic conditions at +0.7 V and +0.3 V vs. V<sub>RHE</sub>, respectively.

The TiO<sub>2</sub> layer was prepared according to the method described by C Li et al. Compared to the In<sub>2</sub>S<sub>3</sub> and CdS layers, TiO<sub>x</sub> has the advantage of good stability and resistance to photocorrosion. As the thickness of the TiO<sub>x</sub> is only ca. 13 nm, there is not significant reduction in the dark current (**Figure 3-19**). Obviously, the onset potentials of the reaction increased to 0.98 V<sub>RHE</sub>, making the oxygen reduction reaction more likely to occur. Under the bias of 0.7 V<sub>RHE</sub>, the photocurrent density was around 335 µA·cm<sup>-2</sup>, but the photocurrent decayed very quickly and hydrogen peroxide was generated at a rate of  $4.38 \text{ mg}\cdot\text{L}^{-1}\cdot\text{h}^{-1}\cdot\text{cm}^{-1}$ , corresponding to a Faraday efficiency of 49%.

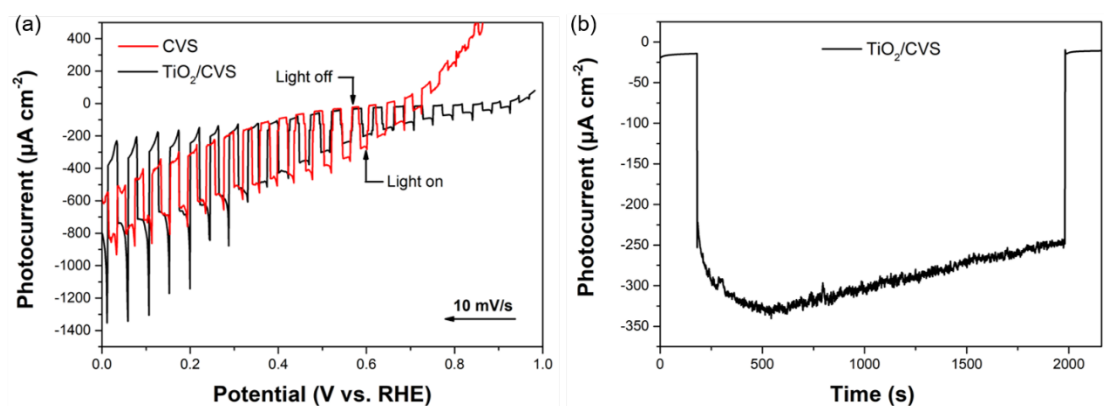


**Figure 3-19.** (a) Linear sweep voltammograms of 0.5%Ga-Cu<sub>3</sub>VS<sub>4</sub> and TiO<sub>x</sub> modified 0.5%Ga-CVS electrodes in O<sub>2</sub>-bubbling phosphate buffer electrolyte (0.1 M, pH = 7) under chopped illumination from visible light (420-800 nm, 100 mW/cm<sup>2</sup>) irradiation. (b) Time courses of the photocurrent of TiO<sub>x</sub>/CVS



electrodes in an O<sub>2</sub>-saturated phosphate buffer electrolyte (0.1 M, pH = 7) with visible light (420–800 nm, 100 mW/cm<sup>2</sup>) irradiation under the potentiostatic conditions at +0.7 V and +0.3 V vs. V<sub>RHE</sub>, respectively.

The band structures of CVS, In<sub>2</sub>S<sub>3</sub>, CdS and TiO<sub>2</sub> were further analyzed since those n-type semiconductors modified with Ga-doped CVS electrodes did not significantly increase in photocurrent density (**Figure 3-20**). It is expected that CVS will form a type II heterojunction structure with several other n-type semiconductors, facilitating charge separation and transfer. Electrons are transferred from CVS to the n-type semiconductors, which then further reduces O<sub>2</sub> to form ·O<sup>2-</sup>, which could be easily disproportionated in water to form H<sub>2</sub>O<sub>2</sub>. However, the Faraday efficiency of the In<sub>2</sub>S<sub>3</sub>/CVS electrode was surprisingly low at 17% (**Figure 3-21**). This may be due to the fact that In<sub>2</sub>S<sub>3</sub> forms a Z-scheme conjunction with CVS, meaning that the holes on the valence band of CVS were directly complex with the electrons on the conduction band of In<sub>2</sub>S<sub>3</sub>, resulting in a competing reaction that prevents further reduction of O<sub>2</sub> to form ·O<sup>2-</sup>. As the valence band of the n-type semiconductor became more positive, this competitive reaction gradually decreases and hydrogen peroxide production increased.

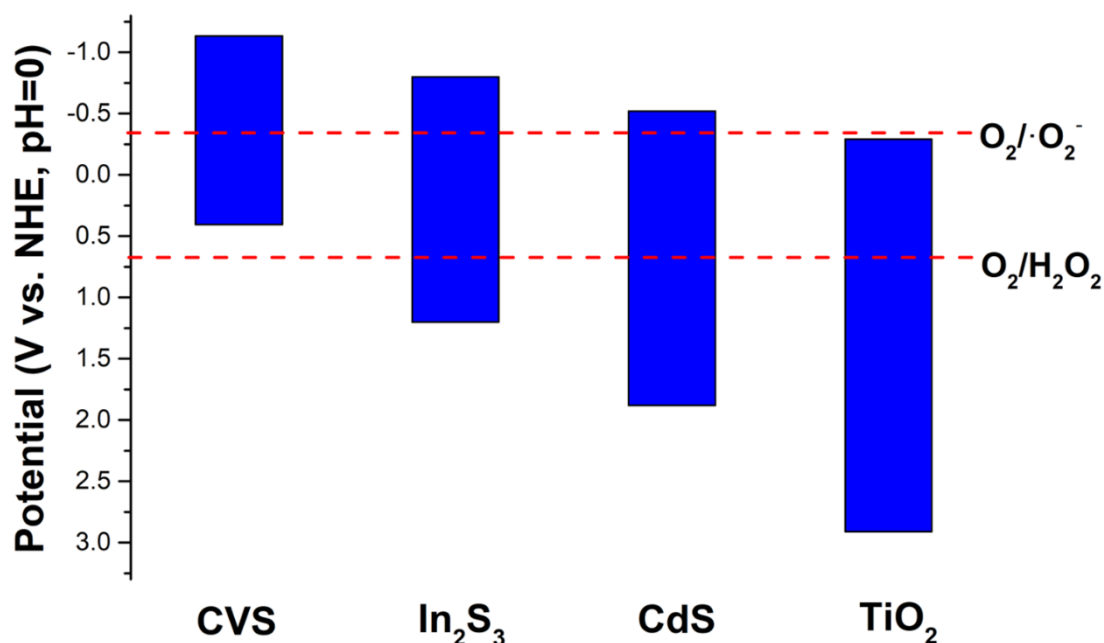


**Figure 3-20.** Band diagram of CVS, In<sub>2</sub>S<sub>3</sub>, CdS, TiO<sub>2</sub>.

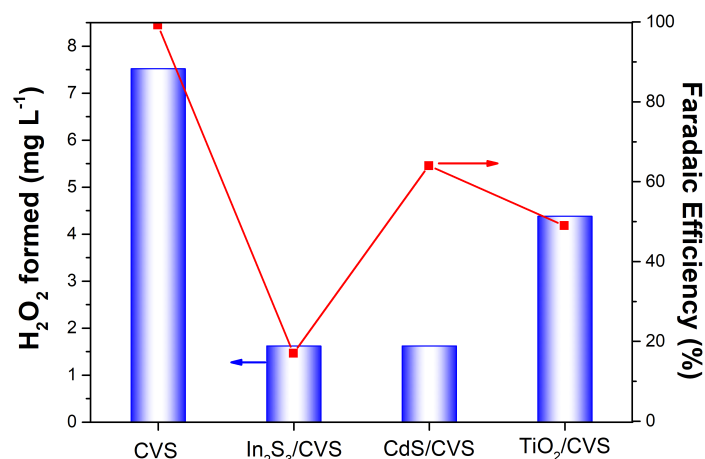


**Figure 3-21.** amounts of generated H<sub>2</sub>O<sub>2</sub> by 0.5%Ga-doping Cu<sub>3</sub>VS<sub>4</sub>, In<sub>2</sub>S<sub>3</sub> modified 0.5%Ga-doping Cu<sub>3</sub>VS<sub>4</sub>, CdS modified 0.5%Ga-doping Cu<sub>3</sub>VS<sub>4</sub>, TiO<sub>2</sub> modified 0.5%Ga-doping Cu<sub>3</sub>VS<sub>4</sub> electrodes with visible light (420-800 nm, 100 mW/cm<sup>2</sup>) irradiation for 1 h and corresponding Faraday efficiencies.

To further verify this conjecture, we first deposited the Mo substrate with In<sub>2</sub>S<sub>3</sub> layers using a chemical bath and then prepared CVS/In<sub>2</sub>S<sub>3</sub>/Mo electrodes using a spray pyrolysis-vacuum sulfurization method as a comparison (**Figure 3-22**). As expected, the photocurrent density was greatly enhanced in comparison to the In<sub>2</sub>S<sub>3</sub>/CVS/Mo electrode at a bias voltage of 0.7 V<sub>RHE</sub>. Notably, the CVS/In<sub>2</sub>S<sub>3</sub>/Mo electrode reached an onset voltage of 0.92 V<sub>RHE</sub>, which is more favorable for the oxygen reduction reaction. Under the bias of 0.7 V<sub>RHE</sub>, the photocurrent density was about 192 μA·cm<sup>-2</sup>, but this was accompanied by a rapid decay of the photocurrent and a hydrogen peroxide generation rate of 4.98 mg·L<sup>-1</sup>·h<sup>-1</sup>·cm<sup>-1</sup>, corresponding to a Faraday efficiency of 99%. However, the photocurrent density is still not as expected, which may require further optimization of the preparation process.

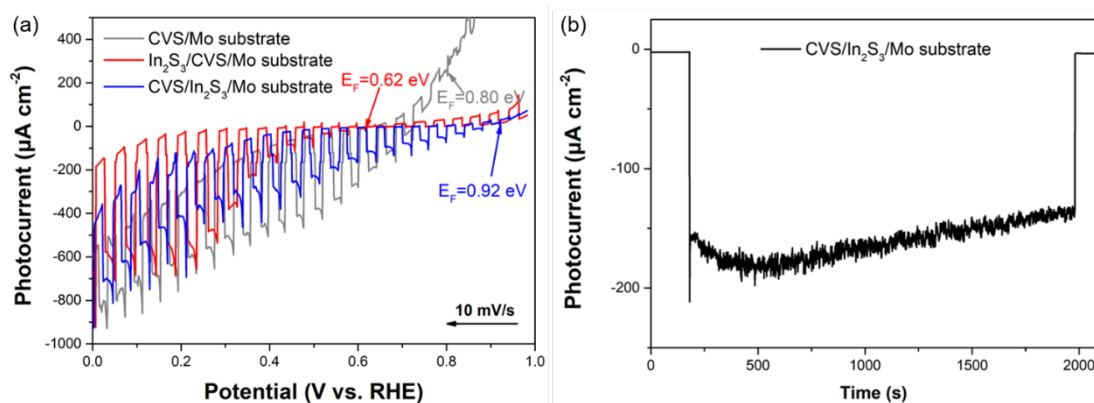


**Figure 3-22.** (a) Linear sweep voltammograms of 0.5%Ga-Cu<sub>3</sub>VS<sub>4</sub>, In<sub>2</sub>S<sub>3</sub>/CVS/Mo and CVS/In<sub>2</sub>S<sub>3</sub>/Mo electrodes in O<sub>2</sub>-bubbling phosphate buffer electrolyte (0.1 M, pH = 7) under chopped illumination from

visible light (420–800 nm, 100 mW/cm<sup>2</sup>) irradiation. (b) Time courses of the photocurrent of the CVS/In<sub>2</sub>S<sub>3</sub>/Mo electrode in an O<sub>2</sub>-saturated phosphate buffer electrolyte (0.1 M, pH = 7) with visible light (420–800 nm, 100 mW/cm<sup>2</sup>) irradiation under the potentiostatic conditions at +0.7 V vs. V<sub>RHE</sub>.

## 4. Conclusions

Photocurrent density and hydrogen peroxide production can be effectively enhanced by the CVS electrode modified with Ag and Ga doping. The Ag-doped CVS electrode effectively increased the particle size of the material, resulting in a significant increase in photocurrent density and stability. The optimum Ag doping amount was determined to be 3%, where the photocurrent density reached 160  $\mu\text{A}\cdot\text{cm}^{-1}$  and the H<sub>2</sub>O<sub>2</sub> production was 4.04  $\text{mg}\cdot\text{L}^{-1}\cdot\text{h}^{-1}\cdot\text{cm}^{-1}$  with a Faraday efficiency of 95.6%. Two factors contribute to the improvement in photocurrent density caused by Ga doping: firstly, Ga doping effectively widens the bandgap of the CVS electrode, increasing light absorption efficiency; secondly, Ga doping increases electrical conductivity, increasing charge concentration and therefore charge separation efficiency. The optimum Ga doping amount was determined to be 0.5%, where the photocurrent density reached 325  $\mu\text{A}\cdot\text{cm}^{-1}$  and the H<sub>2</sub>O<sub>2</sub> production was 7.52  $\text{mg}\cdot\text{L}^{-1}\cdot\text{h}^{-1}\cdot\text{cm}^{-1}$  with a Faraday efficiency of 99%. In contrast, Ag and Ga co-doping resulted in lower hydrogen peroxide production and corresponding Faraday efficiency, probably due to the formation of complex centers within the electrode.

To further improve the photocurrent density, the 0.5% Ga-doped CVS electrode was characterized by TEM-EDS and it was found that a large number of voids existed between the CVS and the Mo substrate, along with the presence of a MoS<sub>2</sub> layer. These two causes resulted in a reduced rate of charge transfer from the CVS to the Mo substrate, which affected the photocurrent density and hydrogen peroxide generation. Finally, the sulfurization time and temperature were optimized to 600 °C and 10 min, at which point the photocurrent density was the largest under a bias of 0.7 V<sub>RHE</sub>.

Several n-type semiconductors have been used to modify the 0.5% Ga-doped CVS electrode, but the energy band structure does not match and does not improve charge separation efficiency or photocurrent density.

## References

- [1] 河野浩貴、平成 31 年度卒業論文.
- [2] S. Ikeda, N. Aono, A. Iwase, H. Kobayashi, A. Kudo,  $\text{Cu}_3\text{MS}_4$  ( $M=\text{V}, \text{Nb}, \text{Ta}$ ) and its Solid Solutions with Sulvanite Structure for Photocatalytic and Photoelectrochemical  $\text{H}_2$  Evolution under Visible-Light Irradiation, *ChemSusChem*, 12 (2019) 1977-1983.
- [3] A.B. Kehoe, D.O. Scanlon, G.W. Watson, The electronic structure of sulvanite structured semiconductors  $\text{Cu}_3\text{MCh}_4$  ( $M = \text{V}, \text{Nb}, \text{Ta}$ ;  $\text{Ch} = \text{S}, \text{Se}, \text{Te}$ ): prospects for optoelectronic applications, *Journal of Materials Chemistry C*, 3 (2015) 12236-12244.
- [4] P. Lemoine, G. Guelou, B. Raveau, E. Guilmeau, Crystal Structure Classification of Copper-Based Sulfides as a Tool for the Design of Inorganic Functional Materials, *Angew Chem Int Ed Engl*, 61 (2022) e202108686.
- [5] S. Yılmaz, S.B. Törelı, İ. Polat, M.A. Olgar, M. Tomakin, E. Bacaksız, Enhancement in the optical and electrical properties of CdS thin films through Ga and K co-doping, *Materials Science in Semiconductor Processing*, 60 (2017) 45-52.
- [6] W. Septina, Gunawan, S. Ikeda, T. Harada, M. Higashi, R. Abe, M. Matsumura, Photosplitting of Water from Wide-Gap  $\text{Cu}(\text{In}, \text{Ga})\text{S}_2$  Thin Films Modified with a CdS Layer and Pt Nanoparticles for a High-Onset-Potential Photocathode, *The Journal of Physical Chemistry C*, 119 (2015) 8576-8583.
- [7] M.R. Fadavieslam, Effect of Ag doping on the physical properties of tin-sulfide thin films for optoelectronic applications prepared by spray pyrolysis, *Applied Physics A*, 124 (2018).
- [8] W. Liu, X. Shi, M. Hong, L. Yang, R. Moshwan, Z.-G. Chen, J. Zou, Ag doping induced abnormal lattice thermal conductivity in  $\text{Cu}_2\text{Se}$ , *Journal of Materials Chemistry C*, 6 (2018) 13225-13231.
- [9] V. Mantella, S. Ninova, S. Saris, A. Loiudice, U. Aschauer, R. Buonsanti, Synthesis and Size-Dependent Optical Properties of Intermediate Band Gap  $\text{Cu}_3\text{VS}_4$  Nanocrystals, *Chemistry of Materials*, 31 (2018) 532-540.
- [10] M. Riaz, R. Zia, A. Ijaz, T. Hussain, M. Mohsin, A. Malik, Synthesis of monophasic Ag doped hydroxyapatite and evaluation of antibacterial activity, *Mater Sci Eng C Mater Biol Appl*, 90 (2018) 308-313.
- [11] Z. Ahmad, B. Gao, A. Mosa, H. Yu, X. Yin, A. Bashir, H. Ghozeisi, S. Wang, Removal of  $\text{Cu}(\text{II})$ ,  $\text{Cd}(\text{II})$  and  $\text{Pb}(\text{II})$  ions from aqueous solutions by biochars derived from potassium-rich biomass, *Journal of Cleaner Production*, 180 (2018) 437-449.
- [12] C.R. Conti, J.R. McBride, G.F. Strouse, Examining the Effect of Dopant Ionic Radius on Plasmonic  $\text{M}:\text{ZnO}$  Nanocrystals ( $M = \text{Al}^{3+}, \text{Ga}^{3+}, \text{In}^{3+}$ ), *The Journal of Physical Chemistry C*, 125 (2021) 7772-7779.
- [13] A. Rana, B.P. Singh, R. Sharma, Structural and chemical changes in Ga doped Ge S glassy alloy, *Journal of Non-Crystalline Solids*, 523 (2019).
- [14] A. Ahmadi, A. Nouri, N. Taghizade, M. Faghihnasiri, Thermodynamic, Mechanical, Optical and Electronic Properties of  $\text{Cu}_3\text{VS}_4$ : An Ab Initio Study, *Journal of Electronic Materials*, 50 (2020) 336-345.
- [15] H. Yan, Q. Ru, P. Gao, Z. Shi, Y. Gao, F. Chen, F. Chi-Chun Ling, L. Wei, Organic pillars pre-intercalated  $\text{V}^{4+}\text{-V}_2\text{O}_5\cdot 3\text{H}_2\text{O}$  nanocomposites with enlarged interlayer and mixed valence for aqueous Zn-ion storage, *Applied Surface Science*, 534 (2020).

- [16] Q.R. Deng, Y. Gao, X.H. Xia, R.S. Chen, L. Wan, G. Shao, V and Ga Co-doping effect on optical absorption properties of TiO<sub>2</sub> thin films, *Journal of Physics: Conference Series*, 152 (2009).
- [17] Y. Du, Q. Tian, J. Huang, Y. Zhao, X. Chang, A. Zhang, S. Wu, Heterovalent Ga<sup>3+</sup> doping in solution-processed Cu<sub>2</sub>ZnSn(S,Se)<sub>4</sub> solar cells for better optoelectronic performance, *Sustainable Energy & Fuels*, 4 (2020) 1621-1629.
- [18] C. Bhoomanee, P. Ruankham, S. Choopun, D. Wongratanaphisan, Diffusion-induced doping effects of Ga in ZnO/Ga/ZnO and AZO/Ga/AZO multilayer thin films, *Applied Surface Science*, 474 (2019) 127-134.
- [19] A. Singh, S. Kumar, Effect of Ag doping on phase-change and photocatalytic performance of rutile - anatase mixed-phase titanium dioxide (TiO<sub>2</sub>) nanoparticles, *Applied Physics A*, 127 (2021).
- [20] X. Zhang, T. Wan, A. Jia, J. Li, G. Liu, D. Sun, Y. Wang, Graphene oxide-wrapped cobalt-doped oxygen-deficient titanium dioxide hollow spheres clusters as efficient sulfur immobilizers for lithium-sulfur batteries, *Electrochimica Acta*, 397 (2021).

## Part 4

### **Conclusion and outlook**

## 1. Conclusion

Hydrogen peroxide ( $\text{H}_2\text{O}_2$ ) is highly promising as a solar fuel and an environmentally friendly oxidant. However, its conventional production method, the anthraquinone method, generates a lot of pollution and consumes a lot of energy. Therefore, a cheap and nontoxic copper-based sulfide photocathode was prepared by an efficient and economical spray pyrolysis method for solar energy conversion to produce  $\text{H}_2\text{O}_2$ .

Based on the key parameters to evaluate the photoelectrochemical properties of the electrode, photocurrent density, a series of modification on copper-based sulfide photocathode was carried out. The main findings of the study are as follows:

1.  $\text{Cu}_3\text{BiS}_3$  thin film electrodes were prepared by electrophoretic deposition and spray pyrolysis deposition, respectively. The differences in surface morphology, crystallinity and charge transfer rate between the electrodes prepared by the two methods were investigated, and the relationship between photocurrent density and these parameters was studied.

2. By modifying the  $\text{Cu}_3\text{BiS}_3$  photocathode with different n-type semiconductors, the best results were found for  $\text{In}_2\text{S}_3$ . A p-n heterojunction formed between the n-type  $\text{In}_2\text{S}_3$  and p-type  $\text{Cu}_3\text{BiS}_3$  substantially increases the photocurrent density by improving charge separation efficiency.

3. Au nanoparticles were found to be the most effective co-catalyst for generating hydrogen peroxide. The high selectivity may be due to the high activity of Au nanoparticles for oxygen reduction reaction. The critical step was the formation of O-Au bonds with a corresponding decrease in the activation energy of molecular oxygen. Therefore, the co-catalyst can significantly improve the charge injection efficiency.

4. Ag-doped  $\text{Cu}_3\text{VS}_4$  electrode effectively increased the particle size of the material, resulting in a significant increase in photocurrent density and stability. By reducing electron-hole recombination between particle interfaces, large particles provide improved charge separation efficiency, leading to high photocurrent densities.

5. Ga-doped  $\text{Cu}_3\text{VS}_4$  electrode effectively increased in photocurrent density. It can be attributed to two factors: firstly, Ga doping effectively increases the bandgap width of

the CVS electrode, which leads to an increase in light absorption efficiency; furthermore, Ga doping leads to an increase in electrical conductivity, indicating an increase in charge concentration and thus an increase in charge separation efficiency.

In summary, this study provided a universal strategy for designing a highly efficient photocathode for producing H<sub>2</sub>O<sub>2</sub> basing on improving light absorption efficiency, charge separation efficiency and charge injection efficiency.

## 2. Outlook

Although we have concluded a series of modification methods for improving photocurrent density and product selectivity, the current photocurrent density and H<sub>2</sub>O<sub>2</sub> generation rate are far from adequate for industrial applications and further optimizations are required.

1. We did not pay attention to the important parameter of sulfur pressure when preparing the Cu<sub>3</sub>BiS<sub>3</sub> electrodes, and the vacuum was only 10<sup>2</sup> Pa. When preparing the CVS electrodes, we increased the vacuum to 1.2×10<sup>-2</sup> Pa, which led to a significant increase in the crystallinity of the electrode material and thus to a significant increase in the photocurrent density.

2. Several common n-type semiconductors were used to modify the CVS electrode; unfortunately, the bandgap structure did not match and could not effectively improve the charge separation efficiency and photocurrent density. There are two ideas here, the first is to continue the search for a suitable n-type semiconductor; secondary, we found that Ga doping can effectively improve the valence band position of the CVS electrode, and if a large amount of Ga is used for doping (e.g. 10%, 20%), it may be possible to make a great change in the bandgap structure of the CVS electrode, thus matched with the n-type semiconductors.

3. It is necessary to find a photoanode that matches the copper-based sulfide photocathode for H<sub>2</sub>O<sub>2</sub> production without adding any additional bias.



## Acknowledgements

My three-year doctoral studies at the Kyushu Institute of Technology have come to an end. Three years ago, with the thoughts of "seeing a different scenery", I joined the dual-degree joint program of Yangzhou University and Kyushu Institute of Technology. Thanks to my supervisors, Prof. Lei Yu and Prof. Ming Zhang, for giving me such an opportunity.

Firstly, I want to express my gratitude to my supervisor Professor Teruhisa Ohno for the thorough guidance he provided. The patient guidance of my professor helped me open the door to photocatalysis as a layman, since my postgraduate studies were in thermal catalysis. Because of my introverted nature, I rarely asked my professor for advice. Instead, I often needed Ohno sensei to ask me about the progress of projects and the problems I encountered, which was really humbling. The professor's wealth of knowledge and high moral character was a source of respect.

I also need to thank Dr. Zhenyuan Teng, Dr. Wenan Cai, Dr. Cao Yu, Dr. Yang Hui, Dr. Xiaoyu Sun, M.S. Zhi Zheng, Dr. Katsuichiro Kobayashi, Miharu Yasugi san, Hiroataka Kawano san, and other students in the ohno lab for their help in the three years. In addition, I am very grateful to Mrs. Dongming Wang and her colleagues in the Student Section for their help in my life at KIT.

Finally, I need to thank my wife and parents for their support, understanding, companionship and tolerance, which made it possible for me to complete my studies.

Chen Chao

2022/08/01

## List of Publications

Chao Chen, Zhenyuan Teng, Miharuru Yasugi, Hui Yang, Yu Cao, Lei Yu, Teruhisa Ohno, A homogeneous copper bismuth sulfide photocathode prepared by spray pyrolysis deposition for efficient photoelectrochemical hydrogen generation, *Materials Letters*, 2022, 325, 132801.

Chao Chen, Miharuru Yasugi, Lei Yu, Zhenyuan Teng, Teruhisa Ohno, Visible light-driven H<sub>2</sub>O<sub>2</sub> synthesis by a Cu<sub>3</sub>BiS<sub>3</sub> photocathode via a photoelectrochemical indirect two-electron oxygen reduction reaction, *Applied Catalysis B: Environmental*, 2022, 307, 121152.